UNIVERSITAT ROVIRA I VIRGILI

TOWARD NANOSTRUCTURED PEROVSKITE SOLAR CELLS BASED ON NANOPOROUS ANODIC ALUMINA TECHNOLOGY

María Del Pilar Montero Rama

ADVERTIMENT. L'accés als continguts d'aquesta tesi doctoral i la seva utilització ha de respectar els drets de la persona autora. Pot ser utilitzada per a consulta o estudi personal, així com en activitats o materials d'investigació i docència en els termes establerts a l'art. 32 del Text Refós de la Llei de Propietat Intel·lectual (RDL 1/1996). Per altres utilitzacions es requereix l'autorització prèvia i expressa de la persona autora. En qualsevol cas, en la utilització dels seus continguts caldrà indicar de forma clara el nom i cognoms de la persona autora i el títol de la tesi doctoral. No s'autoritza la seva reproducció o altres formes d'explotació efectuades amb finalitats de lucre ni la seva comunicació pública des d'un lloc aliè al servei TDX. Tampoc s'autoritza la presentació del seu contingut en una finestra o marc aliè a TDX (framing). Aquesta reserva de drets afecta tant als continguts de la tesi com als seus resums i índexs.

ADVERTENCIA. El acceso a los contenidos de esta tesis doctoral y su utilización debe respetar los derechos de la persona autora. Puede ser utilizada para consulta o estudio personal, así como en actividades o materiales de investigación y docencia en los términos establecidos en el art. 32 del Texto Refundido de la Ley de Propiedad Intelectual (RDL 1/1996). Para otros usos se requiere la autorización previa y expresa de la persona autora. En cualquier caso, en la utilización de sus contenidos se deberá indicar de forma clara el nombre y apellidos de la persona autora y el título de la tesis doctoral. No se autoriza su reproducción u otras formas de explotación efectuadas con fines lucrativos ni su comunicación pública desde un sitio ajeno al servicio TDR. Tampoco se autoriza la presentación de su contenido en una ventana o marco ajeno a TDR (framing). Esta reserva de derechos afecta tanto al contenido de la tesis como a sus resúmenes e índices.

WARNING. Access to the contents of this doctoral thesis and its use must respect the rights of the author. It can be used for reference or private study, as well as research and learning activities or materials in the terms established by the 32nd article of the Spanish Consolidated Copyright Act (RDL 1/1996). Express and previous authorization of the author is required for any other uses. In any case, when using its content, full name of the author and title of the thesis must be clearly indicated. Reproduction or other forms of for profit use or public communication from outside TDX service is not allowed. Presentation of its content in a window or frame external to TDX (framing) is not authorized either. These rights affect both the content of the thesis and its abstracts and indexes.

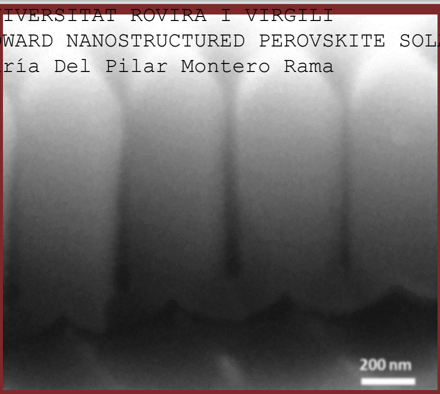

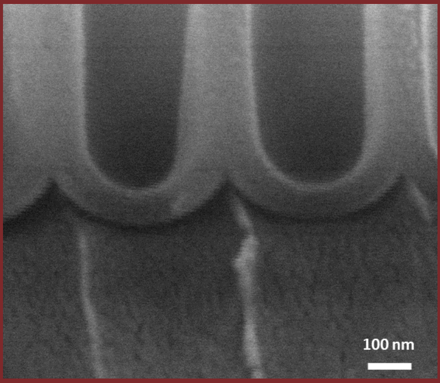

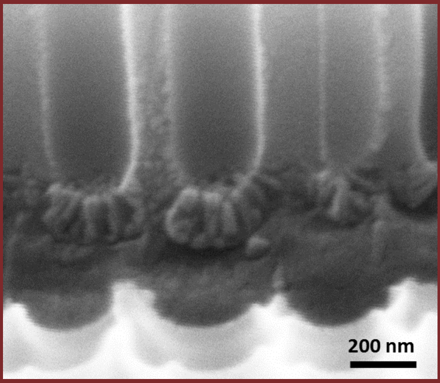

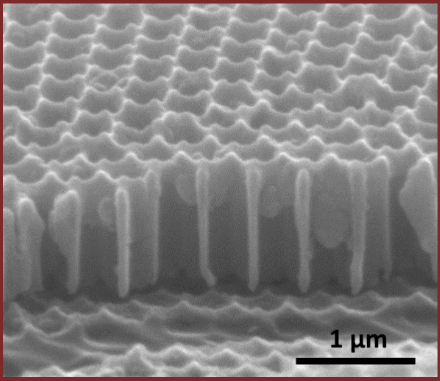

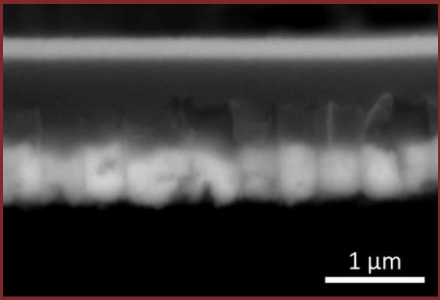

UNIVERSITAT
ROVIRA i VIRGILI

TOWARD NANOSTRUCTURED PEROVSKITE SOLAR CELLS BASED ON NANOPOROUS ANODIC ALUMINA TECHNOLOGY

María Del Pilar Montero Rama

Doctoral Thesis

2020

María Del Pilar Montero Rama

PhD. Thesis

TOWARD NANOSTRUCTURED PEROVSKITE SOLAR CELLS BASED ON NANOPOROUS ANODIC ALUMINA TECHNOLOGY

Supervised by:

Prof. Lluís Francesc Marsal Garví

Departament D'Enginyeria Electrònica Elèctrica i Automàtica

Nanoelectronic and Photonic Systems (NePhoS)

UNIVERSITAT ROVIRA i VIRGILI

Tarragona
2020

UNIVERSITAT
ROVIRA I VIRGILI

Departament d'Enginyeria Electrònica, Elèctrica i Automàtica

Escola Tècnica Superior D'Enginyeria

Campus Sescelades

Avinguda dels Països Catalans, 26

43007 Tarragona

España

Tel. 977 55 96 10

Fax 977 55 96 05

I, Lluís Francesc Marsal Garví state that the present study, entitled "TOWARD NANOSTRUCTURED PEROVSKITE SOLAR CELLS BASED ON NANOPOROUS ANODIC ALUMINA TECHNOLOGY ", presented by María Del Pilar Montero Rama for the award of the degree of Doctor, has been carried out under me supervision at the Department of Electronic, Electric and Automatic Control Engineering of this university and that it satisfies all requirements to be eligible for the International Doctorate Award.

Tarragona, 30 September 2020

Doctoral Thesis Supervisor

Lluís Francesc Marsal Garví

Acknowledgements

Esta tesis doctoral es el fruto de un largo trabajo, el cual he llevado a cabo con mucha ilusión y dedicación. Pero, afortunadamente no ha sido un trabajo en solitario, sino en EQUIPO, al que me gustaría expresar mi gratitud.

En primer lugar, quiero dar las gracias mi supervisor el profesor Lluís F. Marsal por confiar en mí y darme la oportunidad de formar parte de su grupo. Por su soporte y por compartir conmigo su experiencia y conocimientos.

Me gustaría destacar a dos personas que han sido muy importantes para mí en esta experiencia, el doctor Aurelien Viterisi y el profesor Josep Ferré (Au y Pep). Ambos me habéis ayudado mucho, no sólo en lo profesional (una miqueta de esta tesis es vuestra) sino también en lo personal, ya que cada uno a su modo me ha enseñado a mirar la vida de otra forma, de una manera mejor. Merci.

Gracias a todas las personas que forman y han formado parte del grupo NePhoS (y “allegados”) a lo largo de estos años: Laura, Karen, José, Sara, Franchu, Pilar, Carlos, Mari Carmen, Harold, Lindsay, François, Jakub, Pankaj, Amou, Anand, Alfonsina, Rebecca, Enas, Magali y Ángel; por ofrecerme vuestra ayuda cuando lo he necesitado y por los paseos, tardes de playa, comidas en el Llorito, quedadas, etc. Especialmente a Lau, K, Lupito y Sara, por compartir conmigo vuestros conocimientos sobre alúmina, celdas solares y vuestra amistad.

Gracias al profesor Franklin Jaramillo por acogerme en su grupo de celdas solares de la Universidad de Antioquia como si fuera un miembro más y gracias a su equipo: Manuuuu, Juanjo, Rafa, Felipe T., Juan M., Nicky, Natalia, Isa, Santi, Nacho, Juan Pablo, Aleja, Laura, Dayana (SEM) y especialmente al profesor Daniel Ramírez (Dani) por todo lo que me has enseñado (incluido Medellín).

También quiero dar las gracias a Emilio Palomares y a su grupo del Institut Català d'Investigació Química (ICIQ): María, Santi, Ilario, Jesús, Sofía, Cristina, Werther y Nuria por su colaboración y enseñanzas; al personal del Servei de Recursos Cientifics i Tècnics (SRCiT): Lukas, Mariana y Rita por su ayuda durante las sesiones de caracterización.

Me gustaría agradecer a los miembros del tribunal y revisores externos: Josep Pallarès, Agustin Mihi, Maria Isabel Alonso, Franklin Jaramillo y Magali Estrada sus comentarios y correcciones sobre mi trabajo.

Quiero dedicar este libro a mi profesora de química del I.E.S Alonso de Ercilla de Ocaña (Toledo) Sonsoles Mellado, tú me enseñaste a amar la química.

A mis amigos: Geles, Patri, María, Jenny, Sara, Emilio, Ángel y Javi. A pesar de la distancia he sentido vuestros ánimos muy de cerca.

A Alberto, por apoyar y respetar todas mis decisiones, aunque para la mayoría sean una locura, por acompañarme en mi camino con tanta paciencia, amabilidad y amor. Gracias por existir.

Y por supuesto a mis padres, ya que este trabajo no hubiera sido posible sin vosotros: Carlos y Pilar, habéis apoyado y confiado en mi carrera científica incondicionalmente desde siempre, muchísimas gracias por esto y por todo lo que me habéis dado y al resto de mi familia: Carlos, Jesús, Andrés, Nuria, Laura, Carlos, Miriam e incluso al “futuro” Marco por vuestro apoyo y amor.

List of Abbreviations

Ac. - Spin Acceleration

Ag - Silver

Al_2O_3 - Aluminium Oxide

Ar - Argon

Au - Gold

C. - Concentration

C_2H_5OH - Ethanol

$CH_3OCH_2CH_2OH$ - 2-Methoxyethanol

CH_3OH - Methanol

CsI - Caesium Iodide

c-TiO_2 -. Compact Titanium Dioxide

DMD - Dielectric-Metal-Dielectric

D_p - Pore Diameter

DSSC - Dye-Sensitized Solar Cell

E - Electric Field

FAI - Formamidinium Iodide

FF - Fill Factor

FoM - Figure-of-Merit

FTO - Fluorine-Doped Tin Oxide

$H_2C_2O_4$ - Oxalic Acid

H_2CrO_4 - Chromic Acid

H_2CrO_7 - Chromic Acid

H_2SO_4 - Sulphuric Acid

HA - Hard Anodization

HCl - Hydrochloric Acid

$HClO_4$ - Chloric Acid

I_{rndz} - Re-Anodization Current Density

ITO- Indium Tin Oxide

J - Current Density

J_{SC} - Short Circuit Current Density

L - Nanoporous Anodic Alumina Thickness

LiTFSI - Bis(trifluoromethylsulfonyl)amine Lithium Salt

MA - Mild Anodization

MABr - Methylammonium Bromide

$MAPbI_3$ - Methylammonium Lead Iodide Perovskite

MAX - Organic Ammonium

$MeNH_3I$, MAI - Methylammonium Iodide

m-TiO_2 - Mesoporous Titanium Dioxide

N_2 - Nitrogen

NAA - Nanoporous Anodic Alumina

nPSC - Nanostructured Perovskite Solar Cell

OIHP - Organic-Inorganic Hybrid Perovskite

OSC - Organic Solar Cell

P - Porosity

$PbBr_2$ - Lead Bromide

PbI_2 - Lead Iodide

PCE- Power Conversion Efficiency

P_{max} - Maximum Power Point

PSC - Perovskite Solar Cell

Pt - Platinum

PV - Photovoltaic

Q - Current Charge

Rs_{avg} - Average Sheet Resistance

SEM - Scanning Electron Microscopy

$SnCl_2 \cdot 2H_2O$ - Tin (II) Chloride Dehydrate

Ss - Spin Speed

t - Time

T - Temperature

T_{avg} - Average Transmittance

T_{bl} - Barrier Layer Thickness

TBP - Tert-Butylpiridine

TCO - Transparent Conductive Oxide

Ti - Titanium

$Ti(i\text{-}PrO)_2(acac)_2$ - Titanium Diisopropoxide Bis-(acetylacetonate)

$Ti[OCH(CH_3)_2]_4$ - Titanium (IV) Isopropoxide

$TiCl_4$ - Titanium Tetrachloride

TiO_2 - Titanium Dioxide

TiO_2-NPs - Titanium Dioxide Nanoparticles

T_w - Pore Wall Thickness

U - Voltage

U_b - Breakdown Potential

UVO - Ultraviolet-Ozone

V - Potential Bias

V_d - Dropped volume

V_{OC} - Open-Circuit Voltage

WAW - $WO_3/Ag/WO_3$

wBL-NAA - Barrier Layer Free Nanoporous Anodic Alumina

ʎ$_{int}$ - Proportionality Constant (D_{int})

ʎ$_p$ - Proportionality Constant (D_p)

Zn - Zinc

δ_{Ag} - Silver Thickness

ρ_p - Pore Density

List of Figures

List of Tables

List of Contributions

Journal Articles

1. Caterina Stenta; Desiré Molina; Aurelien Viterisi; María Pilar Montero-Rama; Sara Pla; Werther Cambarau; Fernando Fernandez-Lázaro; Emilio Palomares; Lluis F. Marsal; Ángela Satre-Santos. *Diphenylphenoxy-thiophene-PDI dimers as acceptors for OPV applications with open circuit voltage approaching 1 volt*. Nanomaterials (Basel). 2018 Mar 30;8(4):211. DOI: 10.3390/nano8040211.

2. Michael Bothe; María Pilar Montero-Rama; Aurelien Viterisi; Werther Cambarau; Caterina Stenta; Emilio Palomares; Lluis F. Marsal and Max von Delius. *Second-Generation Azafullerene Monoadducts as Electron Acceptors in Bulk Heterojunction Solar Cells.* Synthesis. 2018, 50 (4), 764-771, DOI: 10.1055/s-0036-1591871.

3. Caterina Stenta; María Pilar Montero-Rama; Aurelien Viterisi; Werther Cambarau; Emilio Palomares; Lluis F. Marsal. *Solution Processed Bathocuproine for Organic Solar Cells.* IEEE Transactions on Nanotechnology. Volume 17, Issue 1, January 2018, Article number 8126873, Pages 128-132. DOI: 10.1109/TNANO.2017.2779544

4. María Pilar Montero-Rama, Aurelien Viterisi, Josep Ferré-Borrull, Chris Eckstein and Lluis F. Marsal; *In-situ Removal of Thick Barrier Layer in Nanoporous Anodic Alumina by Constant Current Re-anodization.* Surface and Coatings Technology. 380, 125039. DOI: 10.1016/j.surfcoat.2019.125039

Communications to International Conferences

1. Michael Bothe, María Pilar Montero-Rama, Aurélien Viterisi, Werther Cambarau, Caterina Stenta, Emilio Palomares, Lluis F. Marsal and Max von Delius, *Organic Solar Cells Based on Azafullerene Acceptors*, Graduated Student Meeting on Electronic Engineering (GSMEE), Tarragona, Spain, 2017. **Poster**

2. María Pilar Montero-Rama, José Guadalupe Sánchez, Caterina Stenta, Aurelien Viterisi, Josep Pallarès and Lluis F. Marsal, *Thin Film Metal Oxides as Electron Transport Layer for Efficient Polymer Solar Cells,* Nanoscience and Nanotechnology International Conference (NanoPT 2018), Lisbon, Portugal, 2017. **Poster**

3. Michael Bothe; María Pilar Montero-Rama; Aurelien Viterisi; Werther Cambarau; Caterina Stenta; Emilio Palomares; Lluis F. Marsal and Max von Delius. *Polymer Solar Cells made from Azafullerene Acceptors,* Stability of Emerging Photovoltaics: from Fundamentals to Applications (SEPV18), Barcelona, Spain, 2018. **Poster**

4. Caterina Stenta; Desiré Molina; Aurélien Viterisi; María Pilar Montero-Rama; Sara Pla; Werther Cambarau; Fernando Fernández-Lázaro; Emilio Palomares; Lluis F. Marsal and Ángela Sastre-Santos. *Diphenylphenoxy-Thiophene-PDI Dimers as Acceptors for OPV Applications with Open Circuit Voltage Approaching 1 Volt*, Stability of Emerging Photovoltaics: from Fundamentals to Applications (SEPV18), Barcelona, Spain, 2018. **Poster**

5. Michael Bothe, María Pilar Montero-Rama, Aurélien Viterisi, Werther Cambarau, Caterina Stenta, Emilio Palomares, Lluis F. Marsal and Max von Delius, *Organic Solar Cells Based on Azafullerene Acceptors*, Graduated Student Meeting on Electronic Engineering (GSMEE), Tarragona, Spain, 2018. **Poster**

6. María Pilar Montero-Rama, Aurelien Viterisi, Josep Ferré-Borrull, Chris Eckstein and Lluis F. Marsal *Development of Nanostructured Perovskite Solar Cells,* 12th Spanish Conference on Electron Devices (CDE 2018), Salamanca, Spain, 2018. **Poster**

7. Aurelien. Viterisi, María Pilar Montero-Rama, Chris Eckstein, Josep Ferré-Borrull and Lluis F. Marsal, *Nanoporous Anodic alumina as Cathode for Perovskite Solar Cells,* Porous Silicon Semiconductors and Technology (PSST), Montpellier, France, 2018. **Poster.**

8. María Pilar Montero-Rama, Aurelien Viterisi, Josep Ferré-Borrull, Chris Eckstein and Lluis F. Marsal *Electrochemical Method for Removing Thick Barrier Layer in Nanoporous Anodic Alumina*, NanoSpain2019 conference, Barcelona, Spain, 2019. **Oral presentation.**

“An expert is a person who has made all the mistakes which can be made, in a narrow field.”

Niels Bohr

Contents

Chapter 1

Introduction

1.1 Motivation and Background

Nanotechnology research has achieved great attention in the last decades. Nano-sized materials present excellent and unique optical, electrical, magnetic, catalytic, biological, or mechanical properties.[1] Therefore, nanomaterials can implicate in several fields such as chemistry, sensors, biotechnology, electronics and so on.[2,3]

Currently, one of the most active nanotechnology research is based on nanoporous materials synthesized by electrochemical techniques, such as nanoporous anodic alumina (NAA). NAA prepared by aluminium substrates anodization possesses exceptional chemical, optical and mechanical properties, for example, chemical resistance, thermal stability, hardness, biocompatibility and large specific surface area.[4] NAA is an excellent platform to develop applications as cell adhesion and culture,[5–7] chemical/biological sensing,[8–10], drug delivery,[11,12] energy generation and storage and template synthesis.[13–16]

NAA offering exciting new possibilities in the field of renewable energy production/conversion and storage. Focusing on the use of NAA as energy generation devices, it is necessary that these devices also meet the same requirements of sustainability and efficiency, making the entire process of generation and consumption of energy as clean as possible.

Approximately 80% of global energy consumption, which includes supplying 65% of global electricity generation comes from fossil fuels (coal, oil and natural gas).[17] Reducing our dependence on these energy sources by moving to renewable ones such as wind and solar will enable a notable reduction in carbon emissions. If humanity does not act quickly to reduce emissions of greenhouse gases, particularly carbon dioxide (CO_2) released through the burning of fossil fuels, we face devastating consequences. Fortunately, society is increasingly aware of the usage of sustainable energy sources that protect the environment, such as solar energy.

The Sun is the main source of visible light and the most significant source of radiant energy that hits the Earth. The total solar irradiance hitting the top of the Earth's atmosphere is around 1361 W/m^2.[18] This energy can be used for heating, by plants for the process of photosynthesis and for generating electricity. Nowadays, solar energy is one of the most important renewable energy for getting a future sustainable.

Organic-inorganic hybrid perovskites (OIHPs) have drawn tremendous research attention in the past years because of their various advantages for photovoltaic (PV) applications such as large absorption coefficient,[19] suitable bandgap,[20] excellent crystallinity[21] and long carrier diffusion length. To judge the feasibility of the commercialization of photovoltaic technology, three factors are usually considered: cost, efficiency and stability. The power conversion efficiency (PCE) of a PV device is a measure of the percentage of light incident upon it that is converted into usable electricity. Perovskite solar cells (PSCs) are predicted to be low- cost because of their low material and fabrication costs. In a few years, its PCE almost reaches the value of silicon solar cells. However, stability still requires further development.

This thesis aim is focused on the use of NAA technology to develop nanostructured perovskite solar cells. Confining perovskite nanocrystals within NAA considerably increases its stability because NAA templates propitiously serve as an encapsulation.[22] Therefore, first, the familiarization process with the manufacture and characterization of NAA, as well as of high-efficiency PSCs, by known standard methods were conducted.

NAA has not electric contact between the interior of the nanopores and the aluminium substrate. It is due to the as-produced compact oxide layer (barrier layer) at the nanopore bottom. So, the first goal achieved is to remove this thick barrier layer under controlled anodization conditions. With this structural modification, electric contact between the aluminium of NAA substrate and the possible infiltrated materials within the nanopores is reached. Also, the objective of infiltrating the different materials that form the PCSs with a specific height and homogeneous among all the nanopores is studied and attained.

The starting hypothesis in this PhD. dissertation is that by confining the PSC structure within the nanopores of NAA, its performance and durability can be improved. This hypothesis requires to demonstrate the feasibility of such nanostructured PSCs. The goal of this work will be to check this hypothesis by achieving full working nanostructured PSC for the first time and measuring/studying their properties. In this PhD essay, the design and fabrication of an energy generation device founded on nanostructured perovskite solar cells based on NAA technology are presented.

1.2 Summary

The thesis is organized as follows:

In chapter 2, the fundamentals of the nanoporous anodic alumina are explicated. Going through its history, structure, electrochemistry, anodization methods, structural characteristics and anodization parameters. Also, the fundamentals of the perovskite solar cells are expounded. Giving an overview through its history, structure, materials, deposition methods and photovoltaic parameters.

In chapter 3, the experimental methods employed for preparing nanostructures based on anodic aluminium oxide are defined. Additionally, the experimental methods used for manufacturing high-efficiency perovskite solar cells, which will be the reference cells of this thesis, are described.

In chapter 4, a new method for the removal of the thick barrier layer in nanoporous anodic alumina without removing the aluminium substrate is bestowed.

In chapter 5, a novel type of perovskite solar cell device on a metallic substrate, using nanoporous anodic alumina as a enclosure, is presented. The experimental methods used for infiltrating distinct kinds of materials within the nanoporous anodic alumina membrane, which barrier layer was previously removed, are explained. A nanostructured perovskite solar cell device is manufactured, and its current density-voltage characteristics are measured.

In chapter 6, the optimization of the nanostructured perovskite solar cell device obtained in the preceding chapter is investigated. Several changes were introduced to achieve a solar cell with better current density-voltage characteristics. The experimental part of this chapter was carried out in the CIDEMAT group of the University of Antioquia from Medellin (Colombia)

In chapter 7, the general conclusions of the thesis and the overall results achieved during this research are summarized. Also, future works related to this research are added.

Following, there are two appendixes. The appendix I and II, in which the characterization and the thin-film deposition techniques used in this thesis are briefly explained, respectively. At the end of the document, there is a list of the references used to carry out this work.

Chapter 2

Fundamentals of Nanoporous Anodic Alumina and Perovskite Solar Cells

In the following chapter, the fundamentals of the nanoporous anodic alumina are explicated. Going through its history, structure, electrochemistry, anodization methods, structural characteristics and anodization parameters. Also, the fundamentals of the perovskite solar cells are expounded. Giving an overview through its history, structure, materials, deposition methods and photovoltaic parameters.

2.1 Fundamentals of Nanoporous Anodic Alumina

2.1.1 Brief History

Aluminium exposed to the atmospheric air creates a natural protective layer of aluminium oxide (Al_2O_3, alumina). At the beginning of the 20th century, the aluminium anodization process (an electrochemical process in which the chemistry surface of the aluminium is changed *via* oxidation using an electrolyte to produce an anodic oxide layer that is thick enough to avoid further oxidation) was used by industry mainly to protect metal components from corrosion[23] and with decorative proposes.[24]

However, with the discovery of the electron microscopy, Keller *et al.*[25] characterized the anodic alumina structure for the first time in 1953. They describe the nanoporous anodic alumina (NAA) structure such as a hexagonally arranged arrays of pores in the nanometre range (nanopores). In which, the diameter of the nanopores (D_p) and the interpore distance (D_{int}, the distance between the centres of adjacent pores) are proportional to the anodization voltage (U), which led to an increased interest in research on NAA.

Several theoretical models about pore nucleation and growth in NAA have been suggested,[26–31] but the actual mechanism of NAA growth has yet to be completely clarified. The first theoretical models were developed by Diggle *et.al* in 1968.[26] Subsequently, Thomson and Wood provide a better understanding of the growth mechanism of NAA.[27,28] In 1995 Masuda and Fukuda[32] developed a two-step anodization process, this fabrication process is a cheap way of fabricating nanoporous structures based on aluminium oxide, which marked an inflexion point in NAA history. In 2002, Nielsch *et al.* proposed an empirical rule that self-ordering of porous alumina requires a porosity (P) of about 10% irrespective of the anodizing potential, electrolyte composition and anodization conditions.[33] Later many different types of anodization techniques have been established.[34–36]

Depending on the electrolyte chemical nature (neutral or acid) used in the anodization process a different type of Al_2O_3 can be formed: a non-porous also called barrier type and a porous also called nanoporous anodic alumina (NAA). In the non-porous, the anodic oxide layer is compact, thin, amorphous, wear-resistant and behaves as an electrical insulator. In the porous, the anodic oxide layer is thick and porous.[37] **Figure 2.1** displays the formation diagram of both types of membranes.

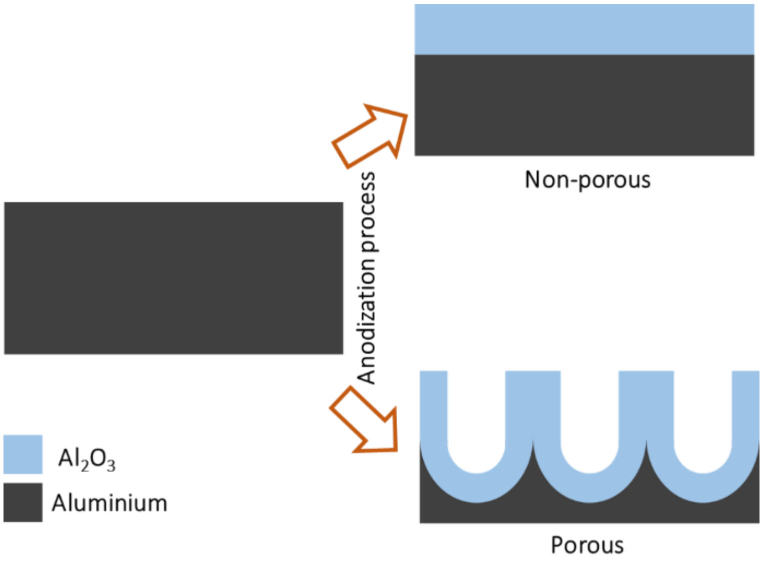

Figure 2.1. Formation diagram of non-porous and porous NAA by aluminium through the anodization process.

In the last decades, many researchers have focused on studying NAA for its use as templates in a great variety of nanotechnology applications.[38–42] Due to its stability, cost-effective scalable production and highly tuneable properties can be obtained templates for nanofabrication with desired geometrical features.[43–45]

NAA has attracted scientific attention in its use not only as a template for fabricating structurally well-defined nanostructures (nanowires,[46] nanotubes[47] and nanodots)[48] *via* electrochemical, physical and chemical deposition methods into NAA, which allows the enhancement of magnetic, electric, catalytic, optical and sensing properties of the deposited materials, due to the small size and high-aspect-ratio of the obtained nanostructures.[49] But also, NAA is a starting material for developing high-performance sensors, photonic, energy harvesting and memory devices.[50–54]

Nanostructured materials have opened a promising way to future renewable energy sources with high conversion efficiency, especially nanostructured solar cells.[55–57] This kind of solar cell uses the advantages of nanostructured gratings for the improvement of light trapping or capturing capacity into the substrate.[58,59] The nanostructured devices reduce the volume of semiconductor materials and enable beneficial optical management, novel conversion mechanisms and improvement of carrier generation and collection.[60–62] These technologies are expected to contribute significantly to a sustainable future for the next generation.[63]

2.1.2 Unit Cell Structure and Chemical Composition

NAA has a honeycomb-like structure in which the hexagon is the unit cell, NAA is formed by numerous hexagonal cells. **Figure 2.2 a)** shows schematically an idealized NAA honeycomb-like structure. In **figure 2.2 b)** the main parameters (explained in more detail in section 2.1.5) which describe NAA structure[25,37,64,65] are marked: Interpore distance (D_{int}), pore diameter (D_p), pore wall thickness (T_w) NAA thickness (L), pore density (ρ_p), porosity (P) and barrier layer thickness (T_{bl}).

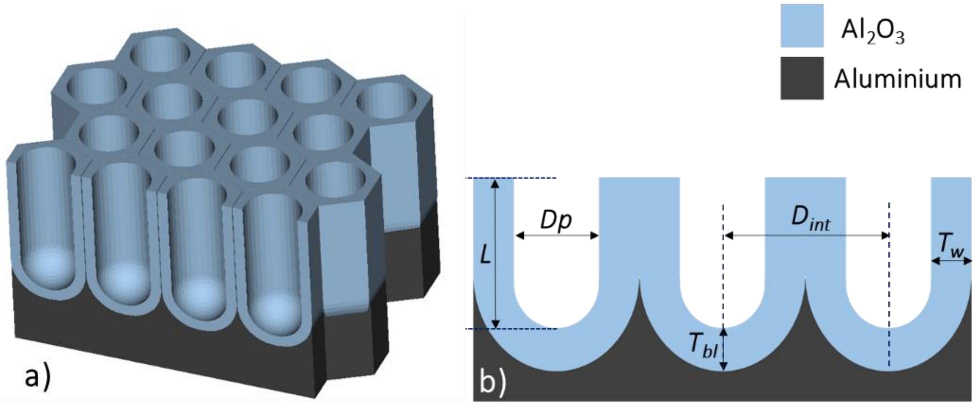

Figure 2.2. a) NAA honey-comb structure **b)** NAA structure main parameters: L: NAA thickness, D_p: pore diameter, D_{int}: interpore distance, T_{bl}: barrier layer thickness and T_w: pore wall thickness.

Every cell encloses, as can be seen in **figure 2.3** three parts: An inner layer (which can be considered the skeleton) which consists of a hexagonal layer formed by the bordering internal walls. An outer layer between the central pore and the inner layer and an interstitial rod inside the inner layer at the triple cell junction. The inner layer is composed of pure Al_2O_3 and the outer layer is composed of Al_2O_3 contaminated with impurities (anionic species i.e.

phosphate, sulphate, oxalate, etc.) from the electrolyte.[66] **Figure 2.3 b)** exhibits the scanning electron microscopy (SEM) picture of NAA top view.

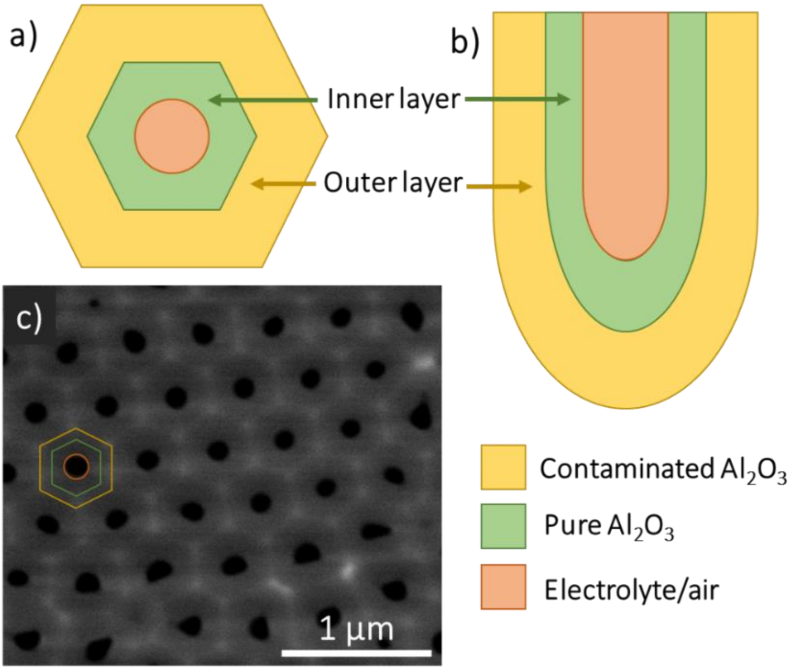

Figure 2.3. a) Top and **b)** cross-sectional views of NAA pore showing the chemical composition distribution inside the nanopore walls. **c)** Top SEM view of NAA. The scale is indicated in the picture.

The thickness ratio of inner and outer layers (ri/o) depends on the electrolyte in the order: sulphuric acid (H_2SO_4) < oxalic acid ($H_2C_2O_4$) < phosphoric acid (H_3PO_4) < chromic acid (H_2CrO_4).[67] Also, Han *et al.* demonstrated that the anionic impurities incorporated depend on the anodization time and the electrolyte concentration.[68] They reported that electrolyte concentration decrease along the pore, so the contaminated area will be thicker on the top of the pores. Besides, one important property of these layers is that the outer layer is less resistant to chemical etching than the inner layer, which prevents the structure from collapsing even at high porosity.

2.1.3 Electrochemistry of Nanoporous Anodic Alumina

Aluminium oxidation can be controlled by the electrochemical aluminium anodization process. Anodic films are formed on aluminium by passing a direct voltage (*U*) through an electrolytic solution (aqueous solution of acid, e.g., H_2SO_4, $H_2C_2O_4$ and H_3PO_4). Aluminium works as the anode and a material that will not be affected by the electrochemical process (usually a platinum wire) is used as the cathode.

The applied *U* generates a high electric field (*E*) across the pre-existing thin oxide film on the surface of aluminium (natural protective layer). Under *E*, the negatively charged anions (O^{2-} and OH^-) of the solution migrate to the anode in which aluminium will be positively charged with consequent electrons lost. If a *U*, which is different depending on the electrolyte used, is applied between the cathode and anode, pores nucleate and start to grow on the aluminium surface. NAA membranes are generally formed under constant *U* or constant current density (*J*) conditions. Under a constant *U*, a typical anodization *J* versus time (*t*) curve, as is showed in **figure 2.4** can be divided into four NAA growth stages.[30,31,69–71]

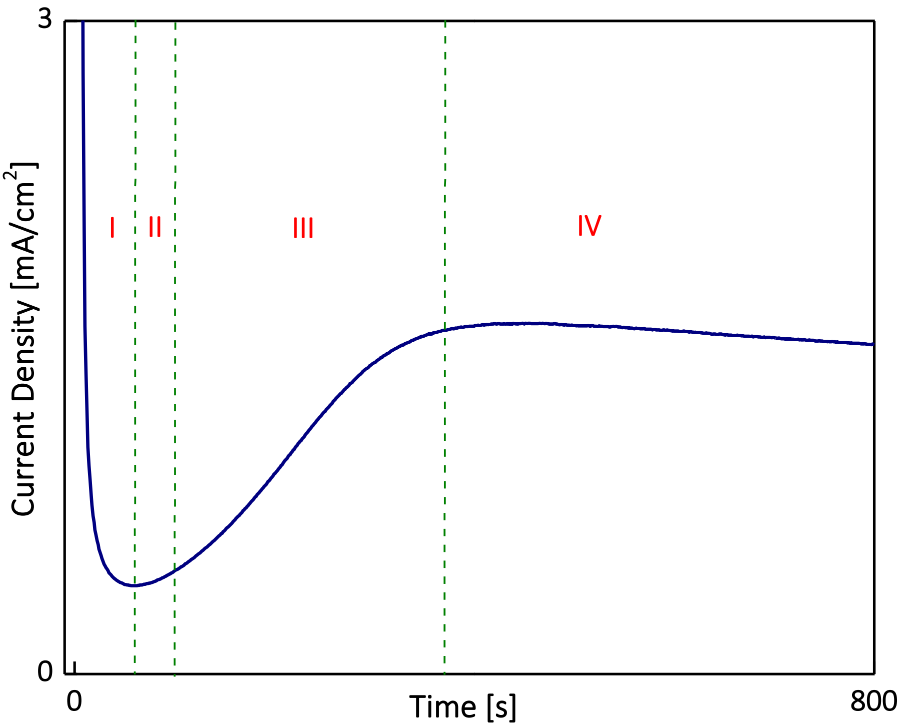

Figure 2.4. Current density *vs* time curve during nanopores formation, which is divided into four stages. **I)** A film of Al_2O_3 starts to grow and forms a compact barrier layer, **II)** pores start to grow, **III)** the anodizing process continues and **IV)** arrangement of pores occurs and continues to grow.

Stage I, the compact oxide (also known as barrier layer) grows as a result of the field-assisted migration of O^{2-} ions through the compact oxide itself. But this process reduces the growth rate gradually with increasing thickness, as for increasing thickness and fixed potential, the electric field is reduced. (I, **figure 2.4** and **figure 2.5**)

Stage II, as the compact oxide thickness reaches a relatively big value and the current is greatly reduced, the electric field becomes too weak to promote ion migration. However, the compact oxide is not completely uniform and has points where the thickness is smaller. At those points, the electric field is enhanced concerning the average value for the complete barrier layer. This enhanced electric field can permit the ion migration and at the same time to promote oxide dissolution, localized at the thickness inhomogeneities. These two processes produce the nucleation of the pores: the formation of concavities at random points on the oxide surface. (II, **figure 2.4** and **figure 2.5**)

Stage III, at the beginning of the pore growth, the rate of the local dissolution of the oxide at the nucleation sites is bigger than the rate of oxide formation. This is probably caused by a local increase of the temperature at the nucleation sites, because of the higher current at those sites. Some authors also mention that the higher local electric field improves the local dissolution of the oxide. As a consequence, the thickness of the oxide is reduced, increasing the observed current. The concavities become deeper forming a pore. (III, **figure 2.4 and figure 2.5**)

Stage IV, the increase in current causes, in turn, an increase in the rate of oxide formation at the bottom of the concavity. When the two rates become equal two dynamic processes happen at the same time: i) local dissolution of the barrier layer at the oxide/electrolyte interface at the bottom of the pore and ii) local production of barrier layer oxide at the metal/oxide interface at the bottom of the pores. These two simultaneous processes are the responsibility of the steady growth of the pores starts. (IV, **figure 2.4** and **figure 2.5**).

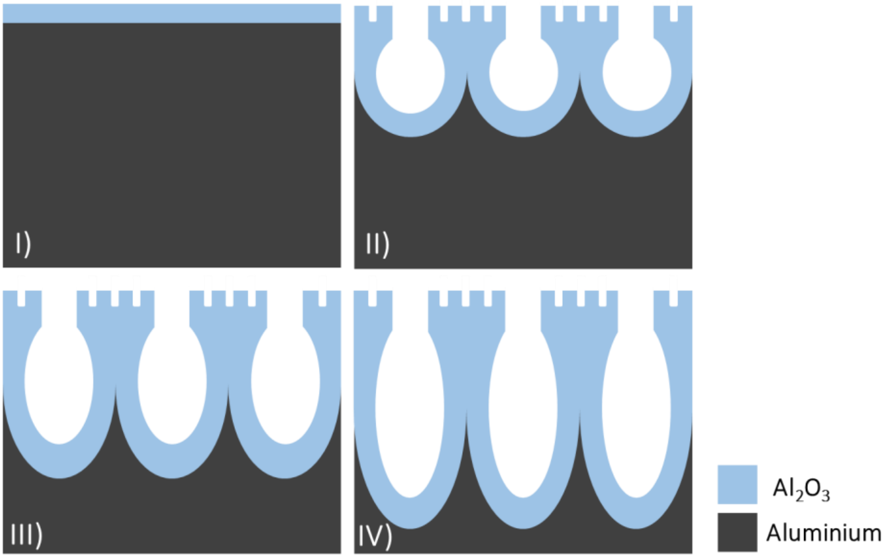

Figure 2.5. Schematic of NAA growth process under constant voltage condition. **I** to **IV** Morphology development with anodization time increasing.

The growth mechanism in steady-state (IV) is the result of competing oxidation (Al_2O_3 formation at the aluminium-oxide interface) and dissolution (Al_2O_3 dissolution at the oxide-electrolyte interface) through the anodization process. Although it is not clarified, some possible reactions that are probably taking place have been reported.[72–76]

Equation 2.1 shows the overall oxidation-reduction (redox) reaction that takes place during anodizing, it is the sum of the separate reactions at each electrode.

$$2Al_{(s)} + 3H_2O_{(l)} \rightarrow Al_2O_{3(s)} + 3H_{2\,(g)} \qquad (2.1)$$

The process starts with the heterolysis dissociation of water, **equation 2.2**).

$$2H_2O_{(l)} \rightarrow O^{2-}_{(ox)} + OH^{-}_{(ox)} + 3H^{+}{}_{(aq)} \qquad (2.2)$$

The O^{2-} and OH^{-} anions, under the influence of the electric field (*E*), leave the oxide-electrolyte interface and migrate through the barrier layer until the aluminium-oxide interface. When O^{2-} arrives at the aluminium-oxide interface, the metallic aluminium is oxidized (**equation 2.2**) and forms Al_2O_3 (**equation 2.3**). The Al^{3+} and O^{2-} ionic transport at the anode is illustrated in a schematic diagram in **figure 2.6**.

$$Al^{0}_{(s)} \rightarrow Al^{3+}_{(ox)} + 3e^{-} \qquad (2.3)$$

$$2Al^{3+}_{(ox)} + 3O^{2-}_{(ox)} \rightarrow Al_2O_{3\,(s)} \qquad (2.4)$$

H^{+} in contact with e^{-} released from the dissociation of water forms H_2 (**equation 2.4**).

$$6H^{+}_{(aq)} + 6e^{-} \rightarrow 3H_{2(g)} \qquad (2.5)$$

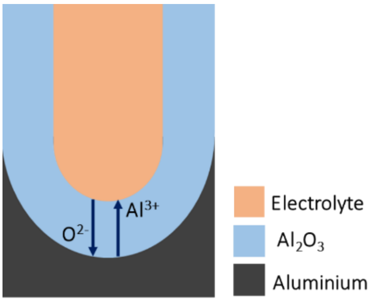

Figure 2.6. Schematic diagram illustrating the ionic transport in porous anodic films on aluminium.

2.1.4 Anodization Methods

Porous NAA membranes can be manufactured using different anodization methods to obtain membranes with specific characteristics. In this section, the most used methods are described: hard anodization (HA) and mild anodization (MA).

2.1.4.1 Hard Anodization

For a given anodizing electrolyte, there is a breakdown potential (U_b) value (27 V, 50 V and 197 V for H_2SO_4, $H_2C_2O_4$ and H_3PO_4, respectively)[77–79] above which anodization is difficult to maintain due to the local current flow and consequent Joule heating which produces local burning. HA uses voltages above U_b[70]. This anodization produces NAA films faster and with a higher porous anodic layer growth rate than using MA.[80] However, the substrate can be damaged because of the high voltage employed. For this reason, HA is not used for nanotechnology research.

2.1.4.2 Mild Anodization (Two-Step Anodization)

Masuda and Fukuda developed in 1995 the so-called “two-step anodization” process[32] for fabricating NAA membranes with a highly ordered arrangement of uniform nanopores. They found that a long anodization process produces an almost ideally arranged honeycomb structure since the pores at the bottom start to be ordered in hexagonal arrays. In the first anodization step, NAA membrane with disordered pores at the top but with ordered pores at the bottom is obtained [**figure 2.7 b)**]. After, NAA membrane (disordered pores) is removed resulting in a pre-patterned aluminium surface with a self-arranged array of concavities (which will act as the nucleation points in the second step) [**figure 2.7 c)**]. In the second anodization, carried out at the same conditions as the first one, the pores start to nucleate at these concavities and form a self-arranged array [**figure 2.7 d)**]. With this method is possible to obtain uniform pore diameter (D_p) and interpore distance (D_{int}) that can be easily tuned by the selection of appropriate anodization conditions.[70,80]

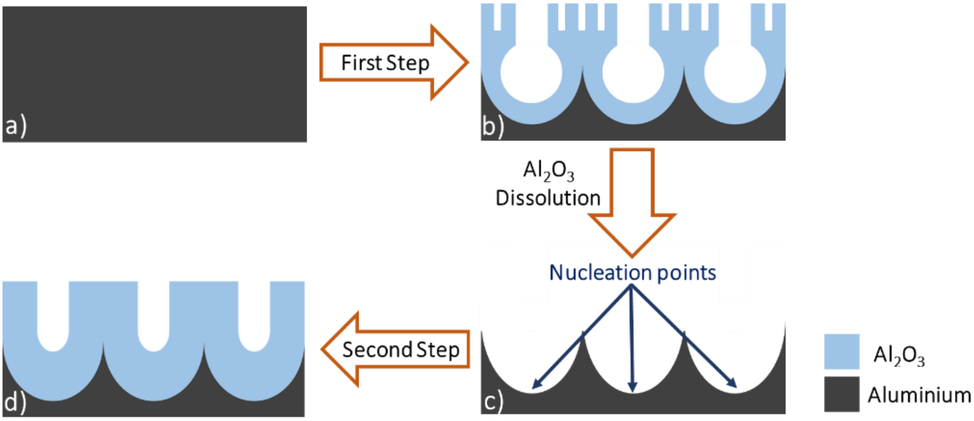

Figure 2.7. Conventional two-step MA process for self-ordered porous NAA **a)** Aluminium substrate, **b)** disordered nanopores, **c)** patterned aluminium surface and d) ordered nanopores.

2.1.5 Structural Characteristics and Anodization Parameters

The structural characteristics of NAA template: interpore distance (D_{int}), pore diameter (D_p), pore wall thickness (T_w), NAA thickness (L), porosity (P), pore density (ρ_p) and barrier layer thickness (T_{bl}), can be controlled by the following anodization parameters: electrolyte type, total current charge (Q) and anodization voltage (U).[25,37,64,65] For ideally ordered NAA, the following relationships can be drawn by simple geometric consideration:

$$D_{int} = D_p + 2T_w \ [nm] \tag{2.6}$$

$$D_p = \Lambda_p U \ [nm] \tag{2.7}$$

$$D_{int} = \Lambda_{int} U \ [nm] \tag{2.8}$$

$$P = \left(\frac{\pi}{2\sqrt{3}}\right)\left(\frac{D_p}{D_{int}}\right) 100 \ [\%] \tag{2.9}$$

$$\rho_p = \left(\frac{2}{\sqrt{3}D_{int}^2}\right) 10^{14} \ [nm^{-2}] \tag{2.10}$$

$$T_{bl} = \Lambda_{bl} U \ [nm] \tag{2.11}$$

The **Interpore distance** (*D_{int}*) is the distance between the centres of adjacent pores. It is directly correlated with the **pore diameter** (*D_p*) and the **pore wall thickness** (*T_w*) by **equation 2.6**. *D_p* is the diameter of the pores. *D_p and D_{int}* are linearly proportional to the anodizing voltage (*U*) by **equations 2.7** and **2.8**, respectively, with proportionality constants (Λ) of approximately Λ_p = 1.29 nm/V and Λ_{int} = 2.5 nm/V.[30,70] *D_p and D_{int}* values depend on the anodization conditions. *D_p* can range from 20 to 200 nm and *D_{int}* from 50 to 500 nm under MA conditions, depending on the applied voltage as **figure 2.8** shows.

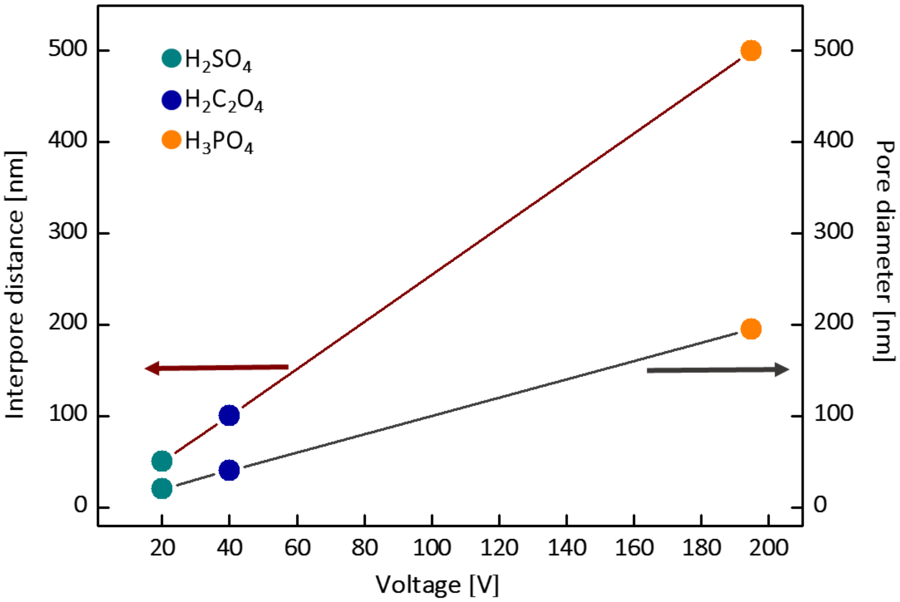

Figure 2.8. Relationship between D_{int} and U (deep-red line) and between D_p and U (grey line) under MA. In sulphuric (green circles), oxalic (blue circles) and phosphoric (orange circles).

NAA thickness (*L*) is proportional to the total current charge (*Q*) involved in the electrochemical oxidation.[81,82] Therefore, the depth of oxide nanopores is easily tuneable from a few tens of nanometres up to hundreds of micrometres by controlling *Q*.[30,83]

The **Porosity** (*P*) can be defined as the ratio of the surface occupied by the pores of the total substrate surface. Under MA conditions, porosity follows rule and is always about 10%.[66] *P* can be correlated with D_p and D_{int} by **equation 2.9**. The **pore density** (ρ_p), is the number of pores that can be found in a specific area. The relationship between ρ_p and D_{int} can be expressed by the **equation 2.10**.

During the aluminium anodization, a very thin, dense and compact dielectric layer is formed at the pore bottoms. This layer called **barrier layer** (T_{bl}) is one of the most important structural parameters of NAA for understanding the kinetics of the electrochemical oxidation of aluminium. Like other structural parameter is directly proportional to U by **equation 2.11** with a proportionality constant (λ_{bl}) of approximately 1.3 nm/V for MA.[30,70].

The pore diameter, wall thickness, as well as the barrier layer thickness of the as-produced NAA can be easily altered by post-treatment procedures involving chemical etching, it is known as pore widening. It consists of immersing the anodized substrates into a phosphoric acid solution (5% wt. concentration) at 35°C for a controlled period. This acid will dissolve the pore oxide walls. [84,85]

2.1.5.1 Electrolyte Type

NAA can be easily fabricated by anodization of aluminium in different kinds of electrolytes, such as sulphuric acid (H_2SO_4)[86], oxalic acid ($H_2C_2O_4$)[87], phosphoric acid (H_3PO_4).[88], and chromic acid (H_2CrO_4).[27] However, for neutral electrolytes with pH in the range of 5–7, only barrier-type alumina thin film can be formed. This work is only focused on the former porous-type. The temperature, concentration and pH of the electrolyte affect strongly to NAA structural characteristics.

The electrolyte **temperature** (T) is a crucial parameter take into account since during the anodizing process an increase in temperature is probable to occur because of local heating.[89,90] This temperature increase can result in the rapid dissolution of the pore walls due to the burning phenomenon.

Besides, the pore growth rate and pore diameter are affected by this parameter, decreasing as *T* is reduced. High temperatures lead not only to faster growth rates but also to a high dissolution rate of formed Al_2O_3 which promotes larger pores.[91,92] For high anodization voltages, the electrolyte temperature can be kept below 0 °C by adding a certain quantity of ethanol (C_2H_5OH) to the acid aqueous solution. Another parameter that affects the pore growth rate is the stirring rate of the acid electrolyte since this ensures that the diffusion of the ionic species and the temperature inside the pores are homogeneous during the anodization process.

The pore diameter (D_p) is mainly affected by the electrolyte **pH** in which value is given by the acid type and its concentration. Low pH values need low anodization voltages, which implies a reduced dissolution of Al_2O_3 which induce smaller pores. For this reason, pores are wider using H_3PO_4 and thinner using H_2SO_4.[93]

2.1.5.2 Anodization Voltage

The pore diameter (D_p) and interpore distance (D_{int}) can be varied from several to hundreds of nanometres mainly by changing the anodization voltage (U).[32,37,65,94,95] It is restricted for a given electrolyte and its concentration since if U is excessively high, the oxide barrier layer usually burns and the pore growth is not homogeneous. This phenomenon occurs due to the conductivity increase in the oxide barrier layer at the pore bottom tips produced by local heating, ionization of atoms that generate more electrons due to energy from the electric field and breakdown of the oxide barrier layer from pre-existing cracks.

To summarize, in **table 2.1** the most usual anodization parameters for the three kinds of acid electrolytes most applied for MA are reported. Besides, the average values of the resulting geometric characteristic are included. In **table 2.2** the relation between the anodization parameters and NAA structural characteristics are indicated.

	H_2SO_4	$H_2C_2O_4$	H_3PO_4
Voltage [*V*]	20	40	195
Temperature [°C]	5	5	-5
Concentration	0.3 M	0.3 M	1% wt.
Pore diameter [nm]	20	40	195
Interpore distance [nm]	50	100	500

Table 2.1. MA parameters for the mostly used anodizing electrolytes.

	D_{int}	D_p	P	ρ_p	T_{bl}
pH	α	α	α	1/α	α
T	-	α	1/α	α	1/α
U	α	α	1/α	α	α

Table 2.2. Qualitative relationship indicating the direct (α) or inverse (1/α) dependence between anodization parameters and structural characteristics of the resulting NAA. D_{int}: interpore distance, D_p: pore diameter, P: porosity, ρ_p: pore density, T_{bl}: barrier layer thickness, T: temperature and U: anodization voltage.

2.2 Fundamentals of Perovskite Solar Cells

2.2.1 Solar Cell Overview

A solar cell, also called photovoltaic (PV, photo means *"light"* and voltaic mean *"electric potential"*) cell is any device that generates electricity directly from the visible light through the photovoltaic effect.[96] Since the PV effect was discovered by A. E. Becquerel in 1839[97] a process where a photon of energy is directly converted into electricity, scientists have developed different technologies and have used different materials to leverage this sustainable energy. The first operational solar cell, based on selenium or copper-gold junction, was reported by C. Fritts in 1885.[98] They obtained a device with less than 1 % efficiency. However, the PV mechanism was not understood since the sunlight was not perceived as a fuel. It came out in the following years that the photovoltaic effect had the same origin as the photoelectric effect: the quantum nature of light, chiefly introduced by A. Einstein in 1905.[99] In 1941[100], Bell telephone's laboratories patented the first silicon solar cell. In the following years, Bell's laboratories developed an intense research activity to increase the efficiency of the solar cells. The first silicon solar cell which converted solar radiation into electrical energy was reported with an efficiency of 6% by D.M. Chapin *et.al.* in 1954.[101]

The development of solar cell technology has gone through three stages, which are known as three generations:

1. First-generation, based on silicon wafers (mono and polycrystalline). Most solar cells and modules sold today are made of crystalline silicon, single-crystalline and polycrystalline silicon wafers with high purity. Nowadays, technologies based on silicon has reached 27.6% of efficiency with silicon single crystals.[102]

2. Second-generation, based on thin-film technology. In this approach, a thin layer of active material, for example, amorphous silicon (a-Si), cadmium telluride (CdTe) or copper indium gallium selenide (CIGS) is deposited onto a substrate, which not only reduces the usage of the active material and consequently the cost, but also makes the cells more flexible and lower in weight. Currently, technologies based on thin-film technology has reached 23.4% of efficiency.[103]

3. Third-generation refers to different emerging technologies which aim is to produce solar cells with lower cost and higher efficiency. The third-generation technologies normally include organic solar cells (OSCs), quantum dots solar cells, dye-sensitized solar cells (DSSCs), perovskite solar cells (PSCs) as well as multi-junction solar cells such as tandem solar cells, with a record efficiency of 17.4%[104], 16.6%[105], 12.3%[106], 25.2%[107] and 47.1%[108], respectively.

In recent years, PSCs have become a promising PV technology, most notable for their high-power conversion efficiencies and potential for cheap, solution-processable, roll-to-roll compatible module production.[109–112] The increase in world-record performance of all solar cell technologies is given in **figure 2.9**, as tracked by the National Renewable Energy Laboratory. PSCs are the fastest-developing solar technology to date with an efficiency that surpassed 25% the last year, which is already really close to the values obtained for silicon.

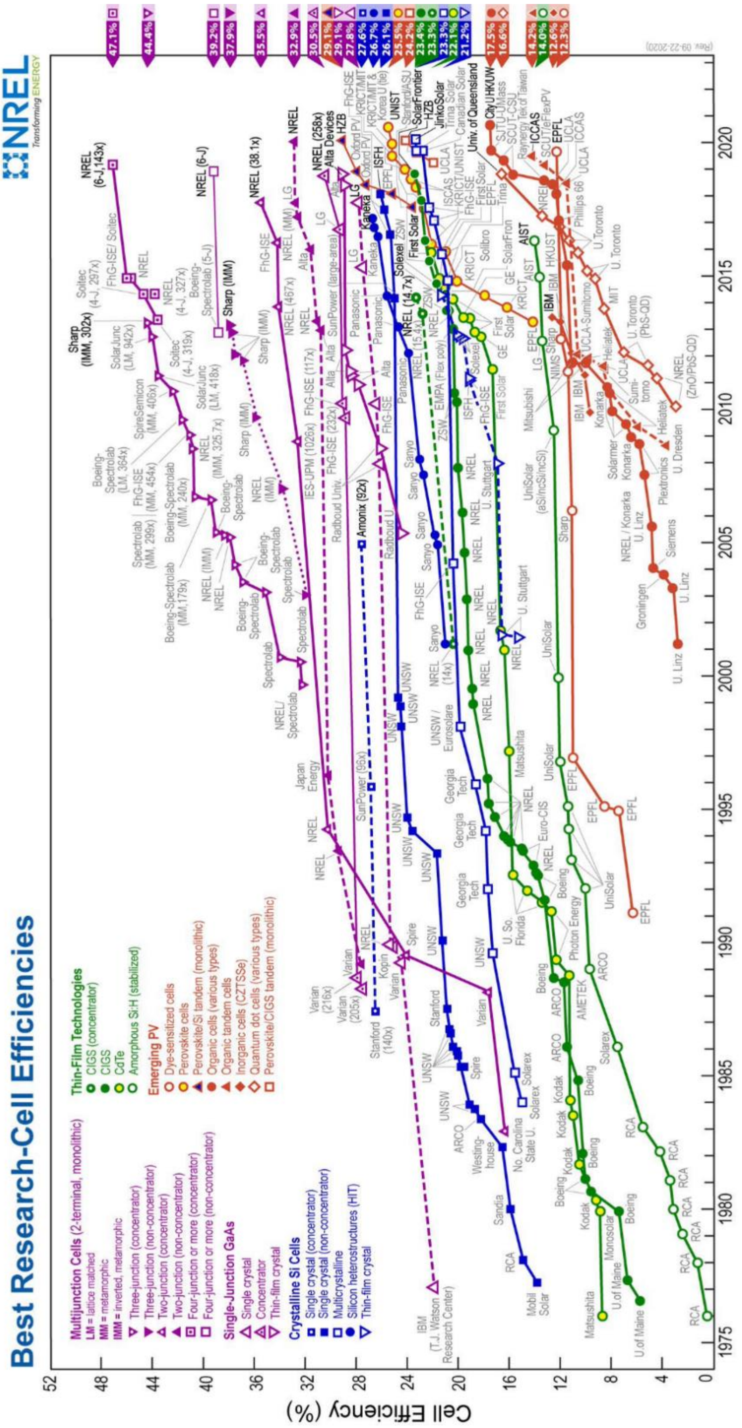

Figure 2.9. Record efficiencies reached by different solar cell technologies during the last decades.[107]

2.2.2 Perovskite Solar Cells

2.2.2.1 Perovskite Materials

In recent years, a crystalline material called perovskite has attracted a lot of attention for use in solar cells. The term 'perovskite' refers to a crystal structure originally found for $CaTiO_3$.[113] The same crystal structure is present in materials with the generic chemical formula ABX_3, in which an *A* cation is located at the eight corners of the cubic cell and a *B* cation, which is smaller than *A*, resides at the body centre, surrounded by six *X* anions (located at the face centres), forming a BC_6 octahedron, as illustrated in **figure 2.10**[114] Such materials are also called perovskites.

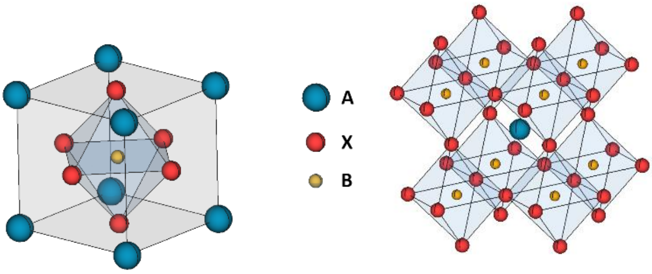

Figure 2.10. Perovskite crystal structure with the generic chemical formula ABX_3.

Perovskite has been investigated in the past few decades for their interesting and unique properties. Perovskite solar cells (PSCs) have become the most promising alternative to replace silicon-based solar cells by more cost-effective PV technologies with attractive properties such as transparency, colour control, flexibility, low weight and so on.[115,116] Hybrid inorganic-organic metal halide perovskites, in particular, have been intensively studied as promising materials for next-generation efficient, lightweight and low-cost thin-film solar cells.[117] In these hybrid perovskites *A* = organic or inorganic cation (i.e., MA^+: $CH_3NH_3^+$, FA^+: $CH_3(NH_2)_2^+$, Rb^+ and

Cs^+), *B* = metal cation (i.e., lead: Pb^{2+}, tin: Sn^{2+}) and *X* =halogen anion (i.e., Cl^-, Br^- or I^-). The main advantage of this materials is their direct bandgap, low exciton binding energy (~2 meV), large absorption coefficient ($5.7x10^4 cm^{-1}$) (enabling efficient light absorption in thin films, long diffusion length (~1 µm in thin films), high electron and hole mobility (10-2320 cm^2/Vs), simple and easy fabrication techniques.[118,119] Also, the replacement of A and X positions by different species allows tuning the optical and electronic properties of perovskite films make them suitable for a variety of applications and device structures[120]. Thus, organic-metallic mixed halide perovskites represent an ideal material for photovoltaics.

2.2.2.2 Perovskite Solar Cells Evolution

PSCs efficiencies have increased from 2.2%[121] in 2006 to above to 24.8%[122] in 2020 in single-junction architectures. Therefore, PSCs are currently fastest-advancing solar technology. With the potential of achieving even higher efficiencies and very low production costs. The hybrid perovskite made its debut in PVs in 2006 when Kojima *et.al* employed $CH_3NH_3PbBr_3$ as a sensitizer on nanoporous TiO_2 in a liquid electrolyte based on DSSC[123], realizing efficiency of 2.2%.[121] In 2009, a power conversion efficiency (PCE) of 3.8% was achieved by replacing Br with I[124], the methylammonium lead iodide perovskite with the chemical structure of $CH_3NH_3PbI_3$ ($MAPbI_3$) was incorporated into to act as the light absorber. In 2011, Im *et al.* achieved an efficiency of 6.5% by employing perovskite nanoparticles on titanium dioxide (TiO_2) for improved absorption over conventional dyes.[125] In 2012, a breakthrough came when two different papers were published almost at the same time. The first one, by Kim *et al.* used spiro-OMeTAD as hole transport layer (HTL), which increased the PCE up to 9.7%.[126] The second one, by Lee *et al.,* replaced the mesoporous TiO_2 with aluminium dioxide (Al_2O_3) as a scaffold, leading to a PCE of 10.9%.[127] These reports revealed the ambipolar nature of perovskites, the perovskite layer can not only absorb light but also transport electrons out of the device.[128,129] In 2014, Grätzel's group reported a mixed-cation perovskite (double cation composition) based on mixed organic cations of MA^+ and FA^+. It was found that the band-gap of perovskite $(MA)_x(FA)_{1-x}PbI_3$ can be tuned by changing the FA^+ content in the composition. The optimal absorption was obtained from $MA_{0.6}FA_{0.4}PbI_3$, with the best efficiency of 14.9%.[130] The report by Correa-Baena *et al.* demonstrated in 2015, that a PCE of 18% could be achieved for planar architectures with SnO_2 as the ETL using a double cation composition.[131] Saliba and co-workers further added a small amount of Cs^+ (*A* position) into the binary mixed cations in 2016, forming a triple cation configuration $Cs_x(MA_{0.17}FA_{0.83})_{(100-x)}Pb(I_{0.83}Br_{0.17})_3$. The triple cation cells provided PCEs up to 21.1%.[132] In 2019, PCE was raised to 23.7%[133] by improving the open-circuit voltage (V_{OC}) and photocurrent. Currently, the highest efficiency of single-junction PSC has exceeding 24.8%.[122]

In the last decade, several investigations have explored the effect of solution concentration[134,135], precursor composition[136], solvent composition[137], post-deposition annealing temperature[138], the presence of additives[139] and deposition method[134,140] on the morphology of perovskite thin films. So, the crystal size, morphology, and orientation of perovskites in the active layers of PSCs have all been found to affect overall PSC efficiency.[141–143] For example, nanoconfinement of perovskite crystallization in mesoporous enclosures likely plays a role in guiding the crystallization process during PSC fabrication. Nanoconfined crystals exhibit, for example, depressed melting points[144–146] and preferential orientations compared to bulk crystals.[147–149] By controlling the size and shape of semiconducting nanocrystals, have been achieved advances nanoelectronics and photonics. Alumina thin-films can be used as templates for the growth of perovskite nanocrystallites directly within device relevant architectures.[150,151]

2.2.2.3 Photovoltaic Parameters

The primary performance parameters of solar cells are the open-circuit voltage (V_{OC}), the short circuit current density (J_{SC}), the fill factor (*FF*) and the power conversion efficiency (*PCE*), which can be obtained from the typical *JV* curve (**figure 2.11**) in the dark and under standard illumination (1SUN intensity, 1000 W/m^2 illumination with AM1.5G spectrum) conditions.

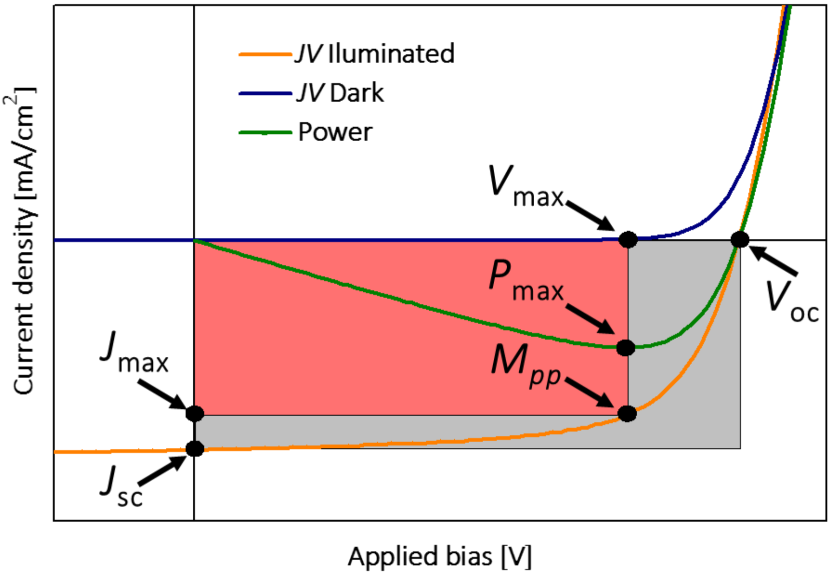

Figure 2.11. Typical *JV* curve with the solar cell photovoltaic parameters in the dark and under standard illumination at 1 SUN. The ratio between the areas of the small and large rectangle is the fill factor.

An external potential bias (*V*) is applied to the cell while measuring the current (*J*) response. $\boldsymbol{V_{oc}}$ is the maximum voltage of a solar cell. It is defined as the *V* at which the measured current is 0 mA/cm^2. $\boldsymbol{J_{sc}}$ is the maximum current density of a solar cell. It is the *J* at which the applied potential is 0 V.

FF measures the amount of power available to be extracted from the device. It is defined by **equation 2.12** in which the maximum power point (P_{max}) is the point at which voltage (V_{max}) and current density (J_{max}) product result in maximum power output from the device[112,115].

$$FF = \frac{P_{max}}{J_{sc}V_{oc}} = \frac{J_{max}V_{max}}{J_{SC}V_{OC}} \qquad (2.12)$$

The ***PCE*** is the most important parameter since it describes the fraction of maximum electric power output generated to the incident power. *PCE* evaluates the device capacity to convert the incident photons in electrons and can be defined by **equation 2.13**, in which P_{in} is the incident light power density (100 mW/cm^2, 1 SUN AM1.5G.)

$$PCE = \frac{P_{max}}{P_{in}} = \frac{FF\ V_{OC}\ J_{SC}}{P_{in}} \qquad (2.13)$$

The measurement of the *JV* curve can be done with two different scan sweeps, forward, which means from J_{SC} to V_{OC} conditions, and reverse, from V_{OC} to J_{SC}. Due to PCSs present the so-called *JV* **hysteresis**, is important to perform the *JV* measurement in both ways, forward and reverse. The *JV* curve taken with decreasing voltage (reverse scan) tends to exhibit higher currents at each voltage than the curve taken with increasing voltage (forward scan).

Several ideas have been proposed as the cause of this phenomenon.[152–154] The idea that it is caused by ion migration is being accepted by more and more researchers, but more work is still needed for better understanding and the avoidance of hysteresis.[155–158]

2.2.2.4 Device Structure and Working Principle of Perovskite Solar Cells

The PSCs devices fabrication is very similar to organic solar cells, with the main difference being that the organic electron accepting material is replaced by an inorganic material. Typically, PSCs present a structure in which the perovskite layer (light-absorbing photoactive layer containing the donor and acceptor material) is sandwiched between two electrodes with different work functions, an anode and a cathode. One of which is transparent (glass or PET) to allow the incoming light to reach the photoactive/absorber layer and the other one of which is a metal electrode to collect the free charge carriers.[159,160] Commonly, materials used for transparent electrodes are based on transparent conductive oxides (TCOs), such as fluorine-doped tin oxide (FTO) or indium tin oxide (ITO). The metal electrode usually consists of a thin metallic film like gold (Au) or silver (Ag).[161] Besides, the perovskite surface is covered with selective charge transport layers. An n-type electron transport layer (ETL), e.g. titanium dioxide (TiO_2) and tin dioxide (SnO_2) and a p-type hole transport layer (HTL), normally 2,2',7,7'-Tetrakis[N,N-di(4-methoxyphenyl)amino] - 9,9' spirobifluorene, spiro-OMeTAD). To transport only one type of carrier (and block the other) to the respective electrode for extraction. Depending on whether the perovskite is deposited on an n-type (ETL) or p-type (HTL) semiconductor, the structure receives the name of n-i-p (normal) or p-i-n (inverted) PSC, respectively.[162,163] Both structures are represented in **figure 2.12**.

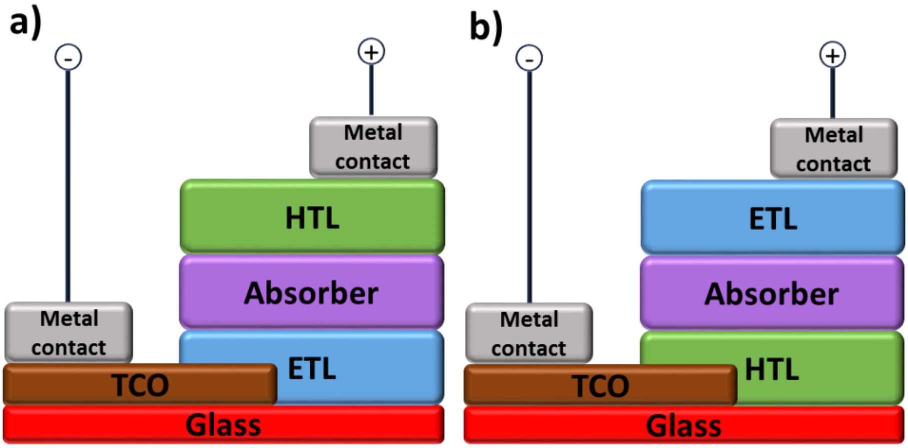

Figure 2.12. PSCs structure types **a)** n-i-p and **b)** p-i-n PSCs architectures. TCO: transparent conductive oxide, ETL: electron transport layer and HTL: hole transport layer. The dimensions of the layers do not correspond to their actual thicknesses.

The n-i-p typed PSC can be further categorized into mesoporous or planar configurations based on the structure of ETL.[164] Both device configurations in general consists of five different layers which are: (1) TCO, (2) planar or mesoporous ETL, (3) light-absorbing layer based on perovskite materials (400-600 nm), (4) HTL (100-300 nm) and (5) a metal electrode (50-150 nm).[117,165]

The mesoporous n-i-p configuration presents spaces within the ETL which allow the infiltration of perovskite materials. The oxide compact layer (20-80 nm) works as the hole blocking layer and the mesoporous layer (100-300 nm) forms the so-called meso-superstructure PSC, which is filled with the perovskite material The oxide compact layer is essential in both planar and mesoporous PSCs to ensure highly efficient electron extraction and transporting from perovskite absorber to TCO.[164] The advantage of employing this configuration is that it can provide a larger contact between ETL and the perovskite absorber layer which latter enables faster charge transfer kinetics.[166] The mesoporous ETL provides spaces for the penetration of perovskite precursors and confines the perovskite crystallites in the small volume of nanopores. This will enhance the absorption of the incident photon and subsequently, boosts the photocurrent generation and increase device efficiency.[167]

In the planar n-i-p configuration, the mesoporous scaffold layer is removed and typically uses a compact ETL (20-80 nm). In this configuration, the perovskite layer is sandwiched between the compact ETL and HTL.[127]. As already mentioned, PSCs are manufactured between two electrodes (a transparent and a back-metal electrode). Most of them are prepared on a glass/plastic substrate covered with a TCO and the metal electrode is deposited on top of the structure. Alternatively, metal substrates can be a viable alternative to TCO substrates, offering advantages such as high-temperature control without the use of expensive ITO.[168] When opaque metal electrodes (metal foils) are used as substrates, a semi-transparent electrode is deposited as the last layer of the solar cell.[169,170] This semi-transparent electrode should have high transmission to let light to be absorbed by the solar cells, especially they should be transparent in a broad wavelength range of 380-700 nm, high electrical conductivity to efficiently collect carriers and soft preparation method in to not damage the below perovskite and charge transport layers.[171] The most common semi-transparent electrodes are transparent conductive oxides prepared by sputtering. However, in the case of PSCs, the sputtering process affects the properties of the underneath layers.[172,173] A dielectric-metal-dielectric (DMD) multilayer has been developed as the top electrode for PSCs. The DMD consist of a combination of transition metal oxides (WO_3, MoO_3, V_2O_5, etc) and a metal (Au, Ag). Metal oxides and metals are thermally evaporated on the top of the substrate.[174–178] Currently, PCSs on opaque metal substrates have reached a PCE of 15%, by Heo *et al.*, who used an anodized Ti foil as the bottom electrode and laminated graphene–polydimethylsiloxane transparent top electrode.[179]

As **figure 2.13** shows, light (photon) is absorbed by perovskite and it promotes the generation of an electron-hole pair, then carriers are separated by the internal electric field and diffuse to proper direction due to charge selective materials: ETL or HTL. Finally, the extraction of those carriers to an external circuit is obtained by the metal contact electrodes.

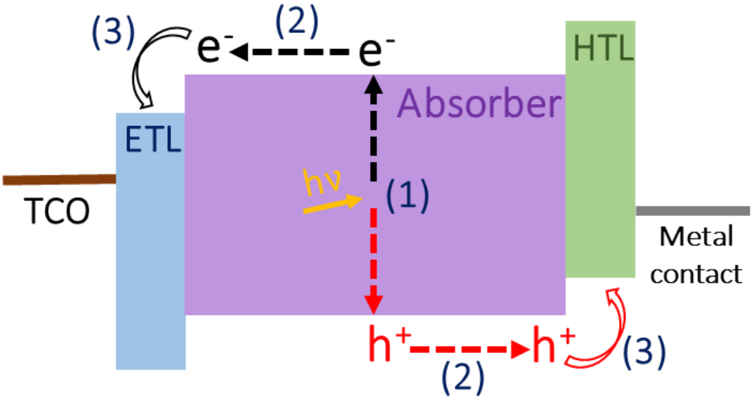

Figure 2.13. Band diagram and main processes and PSC: (1) Absorption of photon and free charges generation, (2) Charge transport and (3) Charge extraction.[180]

2.2.2.5 Perovskite Films Deposition Techniques

The deposition of the perovskite films is mainly based on the reaction of their precursors: organic ammonium (MAX) and inorganic lead halide (PbX_2) where X= I, Cl, Br. The most common deposition technique is the spin-coating *via* one or two-step method or anti-solvent method.[120]

$$PbX_2 + MAX \rightarrow MAPbX_3 \qquad (2.12)$$

The one-step method is based on the co-deposition of both, organic and inorganic, precursors through a solution. The perovskite films are deposited by spin-coating a mixed solution of PbX_2 and MAX in anhydrous organic solvents, e.g. N,N- dimethylformamide (DMF) and dimethyl sulfoxide (DMSO), followed by thermal annealing.[181]

The two-step method is based on the formation of PbX_2 films, normally by spin-coating and their subsequent transformation into perovskite films. The transformation process can be done in different ways: dipping the PbX_2 films into MAX solution[182,183] and spin-coating MAX solution on top of the PbX_2 films.[184,185]

The anti-solvent method is based on dripping a solvent (in which the perovskite is poorly soluble) while the substrate is still spinning. A poor solvent is poured onto the precursor perovskite film during spin coating, causing the salts to precipitate out of solution into a smooth and compact film. The use of anti-solvents enhances crystallinity and allows us to have better control of the perovskite morphology.[137,186]

It is crucial to take into account the fact that perovskites films are very sensitive to degradation in the presence of water and oxygen. Therefore, the absorber and the posterior layers' depositions and annealing steps should be carried out under specific conditions in a glove-box or a dry-box.

The glove-box consists of a large box in which the air was removed and replaced with an inert gas as pure nitrogen (N_2) or argon (Ar).[187]

The dry-box is a large box in which the humidity is kept less than 20 % under a constant dry-airflow.

2.2.2.6 Pre- and Post-Deposition Treatments

The wettability of solutions and adhesion of evaporation can be improved by the cleaning of surfaces and surface energy modification caused by an Ultraviolet-ozone (UVO) treatment. Here, a substrate is illuminated with UV in air, leading to the formation of individual oxygen radicals that go on to form O_3 when combined with other O_2 molecules. Contaminants on the irradiated substrates can undergo photoexcitation followed by a reaction with ozone, liberating any organic material from the surface of the substrate.[188]

At the most basic level, most PSCs are based upon a commercial thin-film transparent conductive oxide (TCO) coated glass substrates, like fluorine-doped tin oxide (FTO) and indium tin oxide (ITO). ITO thin-film of the commercial ITO glass substrates is covering the full glass surface. These thin films can be selectively patterned with a fibre laser.[189] The laser technology is a process that uses a high-intensity laser beam to vaporize the thin layer of a film directly from the surface substrate. Removing a thin film from a substrate creates a circuit that can be used in solar cells, liquid crystal displays, plasma displays, and touch-sensitive panels.

Most solvents will not be completely liberated from a thin-film until the thin-film has been heated (annealing treatment), placed under a vacuum, or a combination of both. This heating is typically done in an oven or on a hotplate. In the context of perovskite solar cells, the same processes are used to extract solvent from the film and to grow perovskite crystal grains. Upon drying, stoichiometric perovskite solutions will often immediately convert to black film.[190]

Chapter 3

Manufacture of Nanoporous Anodic Alumina and High-Efficiency Perovskite Solar Cells

In the following chapter, the experimental methods employed for preparing nanostructures based on anodic aluminium oxide are defined. Additionally, the experimental methods used for manufacturing high-efficiency perovskite solar cells, which will be the reference cells of this thesis, are described. Furthermore, a special focus on critical experimental details is devoted.

3.1 Nanoporous Anodic Alumina Manufacture

In this section, the experimental methods employed for preparing nanostructures based on anodic aluminium oxide are described. The experimental methods are based on a two-step anodization process to obtain alumina layers of self-organized nanopores with specific structural features.[32] The nanoporous anodic alumina (NAA) substrates were manufactured with a nanoporous layer thickness of 1 μm and 650 nm.

3.1.1 Experimental Anodization Set-Up

3.1.1.1 Electrochemical Cell

NAA structures were prepared by the electrochemical aluminium anodization process described in section 2.1.3 of the previous chapter. This process is based on electrochemical cell working. As **figure 3.1** shows a basic electrochemical cell can be divided into the following parts: two electrodes, an anode (aluminium (Al)) and a cathode (platinum (Pt) wire), an electrolyte (acid aqueous solution) and a power supply, which provides the driving force.

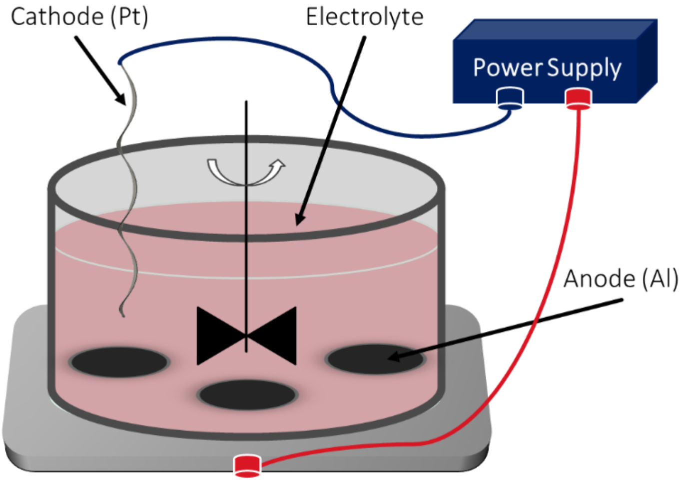

Figure 3.1. Basic schematic diagram of the electrochemical cell for anodizing aluminium substrates. Al: aluminium. Pt: platinum.

The anode (Al) and the cathode (Pt) are immersed in the acid aqueous solution (oxalic, sulphuric, phosphoric acid) which is the transport medium of the ionic species between both electrodes: H^+, Al^{3+} and O^{2-}. The power supply provides the electrical potential (*U*) to ionize aluminium at the aluminium-oxide interface (anode) and generates electrons (e^-). Once the anodization potential is reached the pores nucleate and grow on the aluminium surface.[71,191]

3.1.1.2 Custom-Made Electrochemical Cell

To fabricate NAA structures and for their posterior structural modification (expounded in chapter 4), different voltages (U) and currents (i) profiles needed to be applied. To do so, several custom-made LabVIEW programs were developed. These programs control and monitor the anodization process, using several parameters such as anodization time (t) and total current charge (Q). The communication between the software, the computer and the anodizing hardware (i.e., power supplies and mustimeters) was established employing a high-speed GPIB-USB interface.

Figure 3.2 displays the custom-made electrochemical cell. Given the deadly nature of the voltages used in the process (up to 200 V), PVC was used as the material for the body of the cell. Indeed, PVC possesses very good electrical insulation properties as well as good chemical resistance to weak acids. To avoid energizing the chassis of the cooling apparatus **(1)**, the temperature and cooling control of the electrolyte was carried out through a glass serpentine **(2)**, in this way maximum cooling efficiency and complete isolation between the deadly potentials of the electrochemical cell and the cooling apparatus chassis are achieved. The anode was made from a stainless-steel plate electrically insulated by the bottom part of the cell´s body **(3).** The aluminium substrates **(4)** were simultaneously placed in contact with the anode and the electrolyte *via* the container **(5)**. A platinum wire **(6)** immersed in the electrolyte **(5)** works as the cathode. As the temperature and stirring in the anodization steps are very important,[192,193] a custom-made stirrer controller **(7)** and a thermometer sensor **(8)** were assembled with the help of a programmable microcontroller board (Arduino Uno) **(9)** and a computer **(10)**. A high voltage capability (up to 200V) power supply **(11)** was used for the anodization, keithley2400 (k2400).

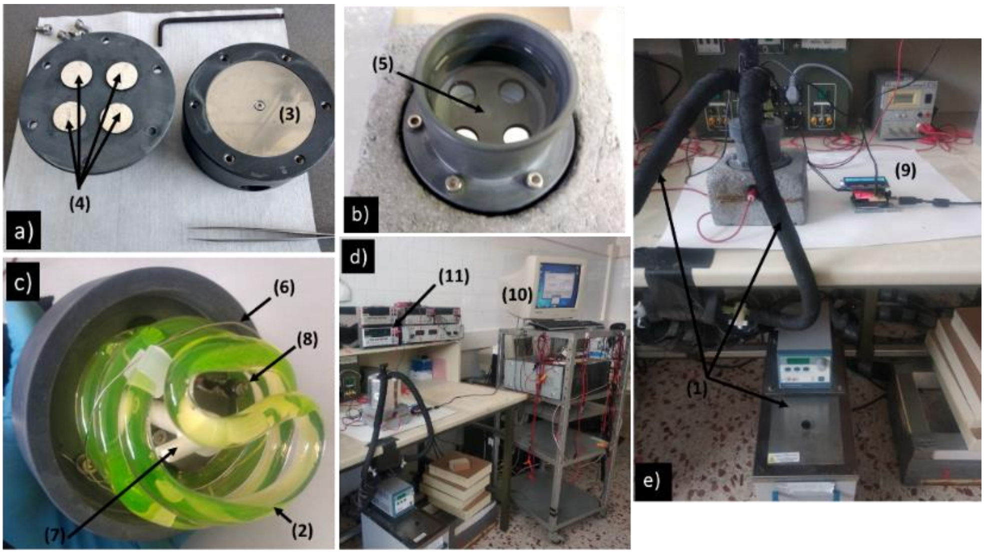

Figure 3.2. Experimental equipment used to fabricate NAA templates. **a) (3)** Stainless steel plate cover by Teflon and **(4)** aluminium substrates placed in a Teflon container. **b) (5)** Teflon container with the electrolyte. **c) (2)** cooling glass serpentine, **(6)** platinum wire, **(7)** home-made stirrer controller and **(8)** home-made thermometer sensor. **d) (10)** Computer and **(11)** k2400. **e) (1)** Cooling apparatus.

3.1.2 Fabrication Process

To obtain hexagonally ordered nanoporous alumina membranes, NAA substrates were prepared following the well-established two-step anodization process described by Masuda *et al.*[32] After each step, a SEM study of NAA substrates was carried out.

3.1.2.1 Electrochemical Polishing

To achieve a homogenous NAA layer the commercial aluminium substrates underwent a pre-treatment before anodization. Several processes of aluminium pre-treatment exist, however, one the most known is the electrochemical polishing (electropolishing).[194,195] Pure aluminium discs, which were used as substrates, were cleaned with acetone, deionised water and ethanol (C_2H_5OH) to remove all the impurities and traces of residual grease. In the electropolishing process, the aluminium substrate (anode) and platinum wire (cathode) are submerged in an electrolyte solution, a voltage is applied between them and the aluminium is oxidized. The electric field generated on the aluminium surface is higher at the surface protuberances than at the basins between adjacent protuberances, so the former dissolves faster than the latter. The electrolyte solution used to electropolish the aluminium substrates was an acid solution 4:1 v/v of C_2H_5OH and per-chloric acid ($HClO_4$) at 20 V. The aluminium substrates and a platinum wire were submerged in the electrolyte for 6 min under a constant stirring rate of 450 rpm and at a temperature between 5 and 10 °C.[196] It is very important to note that temperature control is crucial in this process since the oxidation reaction is extremely exothermic and can be explosive. Besides, if the temperature reaches 20 °C can appearance defects on the aluminium surface [**figure 3.3 d)**]. Finally, the electropolished aluminium substrates were rinsed with deionised water and C_2H_5OH to remove the acid solution. The result is a mirror-like aluminium surface as can be seen in **figure 3.3**. **Figure 3.3 a)** and **b)** show a commercial aluminium substrate photo before and after the electropolishing process, respectively.

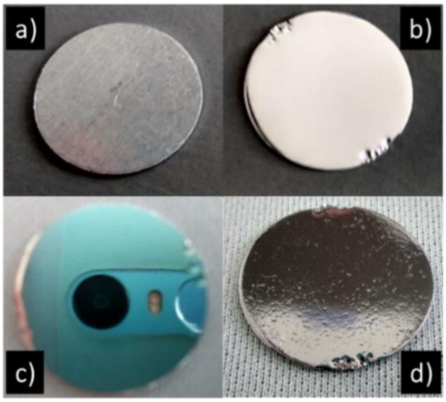

Figure 3.3. Commercial aluminium substrate photos **a)** before and **b)** after the electro-polishing step. **c)** Electro-polished aluminium photo in which can see the reflex of the mobile phone with which the photo was taken. (mirror-like surface) **d)** Aluminium substrate photo after the electropolishing at a temperature around 20°C.

3.1.2.2 First Anodization Step

NAA can be prepared using several different electrolytes. As is explained in section 2.1.5.1 NAA morphology and optical characteristics depend on the choice of this electrolyte.[66,197]

The first anodization step was carried out using a phosphoric acid (H_3PO_4) (1% wt.) solution as the electrolyte. The first step was started at an anodization potential of 175 V and an electrolyte temperature of -5 °C. After 3 h, the anodization voltage was ramped up to 195 V (0.01 V/s). The anodization was continued for 12 h at 195 V at the same temperature.

In this step, the anodization conditions are very important since is a long process in which the substrate is subjecting a high potential. If the anodization potential is 195 V from the very start of the process, current builds up too fast and electric breakdown (U_b) occurs, burning the substrates. For this reason, anodization was started at 175 V, since first induce the formation of a protective oxide layer that prevents the burning substrates at the beginning of the anodization. Also, it is observed that if the anodization started at a temperature of less than -5 °C the substrates will be burned by heat generated at the pore bottom tips.[192,193] In **figures 3.4 a)** and **b)** measured applied voltage *vs* time and measured current *vs* time are plotted.

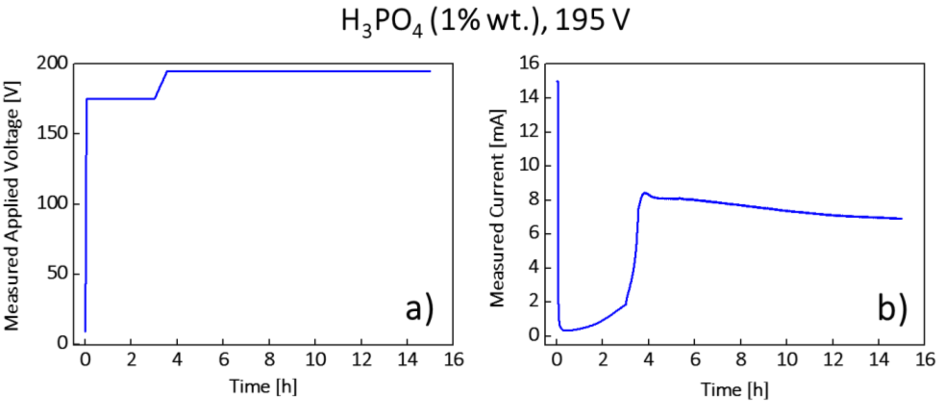

Figure 3.4. a) Measured applied voltage *vs* time and **b)** Measured current vs time corresponding to the first anodization step.

In the initial step, as can be seen in **figure 3.5**, the nanopores grow in an unordered way. **Figures 3.5 a)** and **b)** exhibit the top and cross-section SEM views of the formation of unordered nanopores, respectively. **Figure 3.6 a)** displays the electropolished aluminium surface and **b)** the anodized alumina surface after the first step.

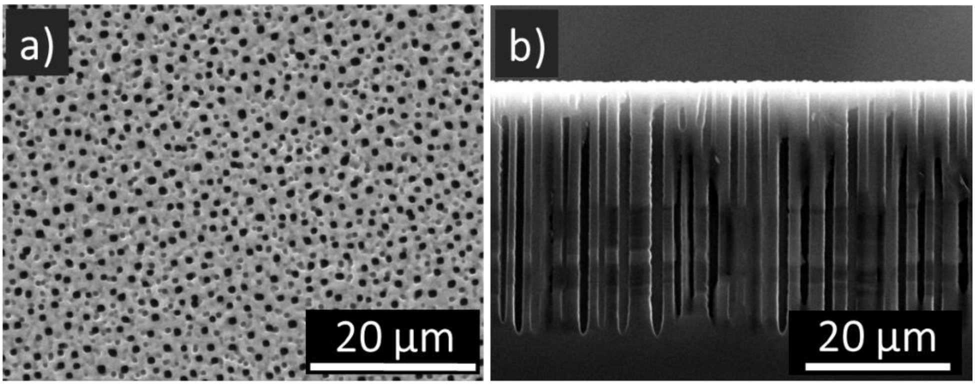

Figure 3.5. a) Top and **b)** cross-section SEM pictures of NAA after the first step. The scale bars are indicated in each picture.

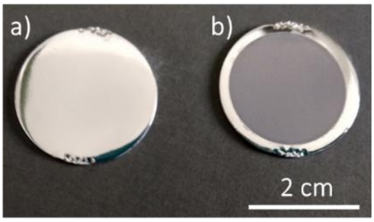

Figure 3.6. a) Substrate photos before and **b)** after the first anodization step. The scale bar is indicated in the picture.

3.1.2.3 Removal of Unordered Nanopores

To achieve an ordered pattern of the nanopores, when the first anodization step finished, the aluminium oxide (Al_2O_3) film with unordered pores on the top and ordered pores on the bottom was selectively dissolved. NAA layer was completely removed by chemical etching in a solution consisting of an acid mixture of chromic acid (H_2CrO_7, 1.8% wt.) and H_3PO_4 for 1 h at 70 °C. **Figure 3.7** shows NAA substrate **a)** before and **b)** after the removal of the unordered nanopores.

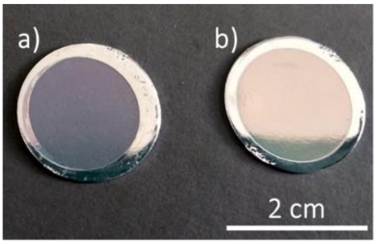

Figure 3.7. Substrate photos **a)** before and **b)** after the chemical etching. The scale bar is indicated in the picture.

3.1.2.4 Second Anodization Step

NAA can be prepared with different thicknesses, diameters and interpore distances. In this thesis, substrates with two different nanoporous film thicknesses were fabricated, 1 µm and 650 nm. The final nanoporous film thickness depends on the total amount of charge that has circulated through the electrochemical cell in this step. The total charged needed was determined via the linear relationship of total anodization charge and NAA thickness.[81]

The second anodization step was conducted in a solution of H_3PO_4 (1% wt.) at an anodization potential of 195 V and -6.5 °C. In contrast to the first anodization step, in the second anodization step, the pores grow in an organised way guided by the concavities on the patterned aluminium surface. The area of a substrate exposed to the electrolyte was 1.76 cm^2. To obtain nanopores with a thickness of 1 µm and 650 nm, the total charge employed in this second anodization step was of 2.63 C and 1.71 C per substrate, respectively. In **figure 3.8 a)** measured applied voltage *vs* time and **b)** measured current *vs* time are plotted. **Figures 3.9 a)** and **b)** exhibit the top SEM views of NAA after the second step.

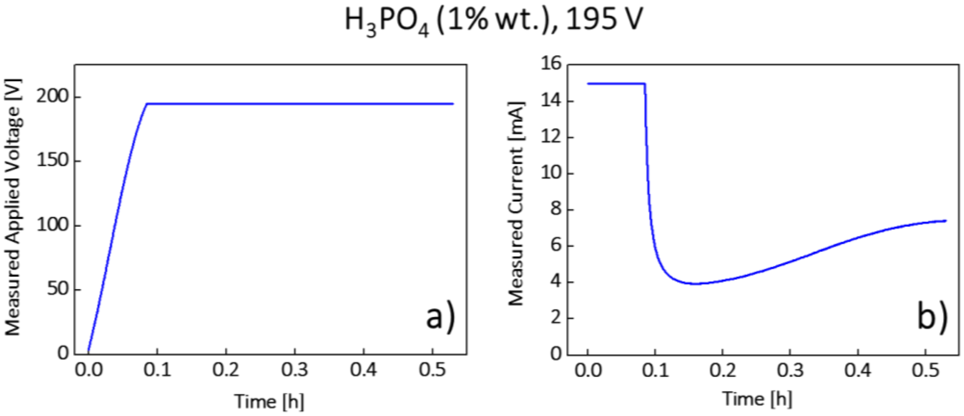

Figure 3.8. a) Measured applied voltage *vs* time and **b)** measured current vs time corresponding to the second anodization step.

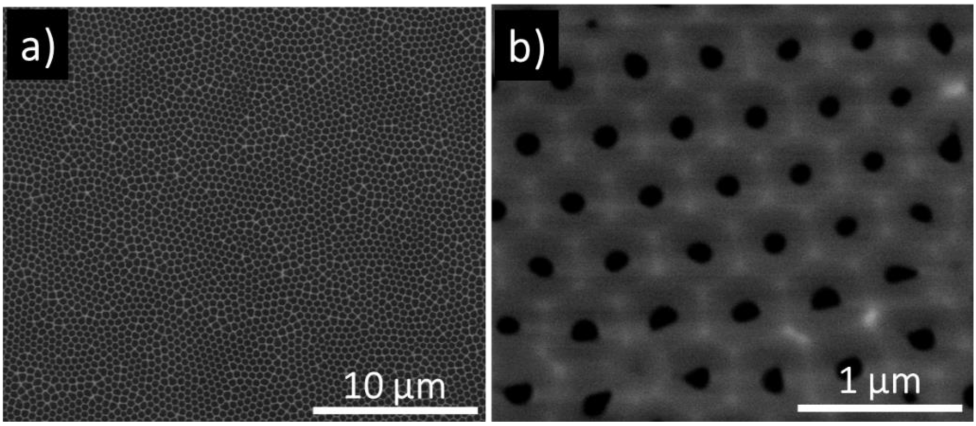

Figure 3.9. a) and **b)** top SEM pictures of NAA after the second step. The scale bars are indicated in each picture.

Figure 3.10 displays the cross-section SEM views of NAA after the second step using a total charge of **a)** 2.63 C and **b)** 1.70 C. From them, a nanopores thicknesses of 1 µm and 650 nm, respectively, can be estimated.

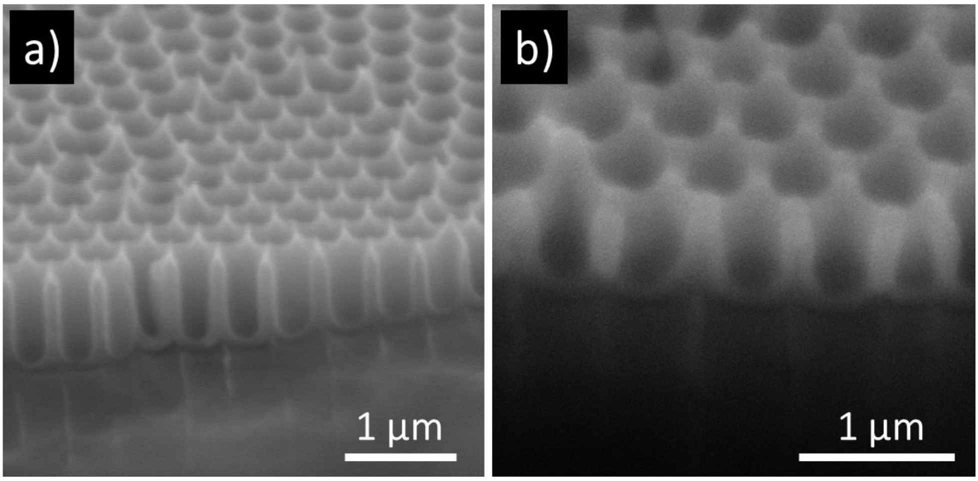

Figure 3.10. Cross-section SEM pictures of NAA after the second step using a total charge of **a)** 2.63 C and **b)** 1.70 C. The scale bars are indicated in each picture.

3.2 Perovskite Solar Cell Manufacture

In this section, the materials used for fabricating high-efficiency perovskite solar cells (PSCs) and NAA-based perovskite solar cell devices (nanostructured perovskite solar cells, nPSCs) are described. Also, the device fabrication process of two different PSCs and their basic electrical characterization is reported. These PSCs will be the reference devices of this thesis. The most common n-i-p architecture for fabricating PSCs is related.[198] The different layers that form the n-i-p PSCs are a transparent conductive oxide (TCO), an electron transport layer (ETL), an absorber layer (AL), a hole transport layer (HTL) and a metal contact.[199] **Figure 3.11** displays a schematic diagram of the previously listed layers for manufacturing the n-i-p PSCs.

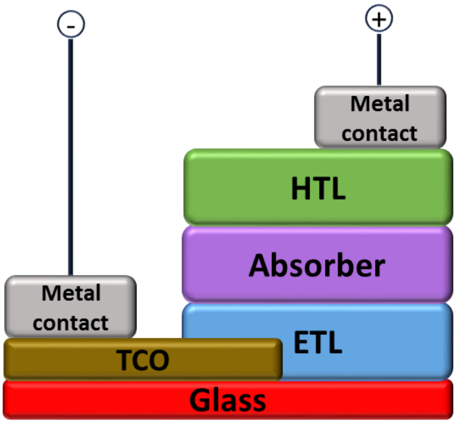

Figure 3.11. N-i-p perovskite solar cell basic architecture scheme. TCO: transparent conductive oxide, ETL: electron transport layer and HTL: hole transport layer. The dimensions of the layers do not correspond to their actual thicknesses.

3.2.1 Materials

3.2.1.1 Electron Transport Layer Materials

PSCs fabricated in this thesis were based on two different electron transport layer (ETL) materials, titanium dioxide (TiO_2) and tin dioxide (SnO_2). For the conventional flat PSCs devices (reference devices) fabrication, TiO_2 was employed for mesoporous devices structure while SnO_2 was chosen for planar devices structure. For nPSCs devices manufacture, only TiO_2 was used.

TiO_2 is the most frequently ETL material used in the most common reported PSCs, due to its suitable energy level, good optical transparency, relatively high electron mobility and environmental stability.[164,200,201] It is also a very good hole blocking layer due to its low lying valence band edge.[202] TiO_2 has several phases where the anatase phase has more research significance for PSCs fabrication.[203]

Recently, SnO_2 has been evaluated as another promising ETL due to its wide bandgap, high transparency and high electron mobility [204–206] Also, SnO_2 nanoparticles have the advantages of possessing good anti-reflective properties and thermal stability.[207] The phase of SnO_2 currently applied in PSCs is the tetragonal rutile structure, which is the most important form of naturally occurring SnO_2.[204]

3.2.1.2 Absorber Materials

PSCs devices prepared in this thesis were based on two different absorber materials, methylammonium lead iodide perovskite ($CH_3NH_3PbI_3$, $MAPbI_3$) and caesium formamidinium methylammonium lead iodide bromide perovskite (triple cation perovskite, CsFAMAPbIBr).

$MAPbI_3$ is the simplest and most widely used perovskite absorber.[208] It has a high optical absorption coefficient, good electrical transport properties, favourable bandgap which is close to the optimum value for a single-junction solar cell.[201] It has become one of the leading compounds for the preparation of organic-inorganic hybrid perovskite solar cells.

Triple cation perovskite films are thermally more stable and less affected by fluctuating surrounding variables such as temperature, solvent vapours or heating protocol[209,210] In this thesis, the triple cation perovskite stoichiometry used is $(FAPbI_3)_{0.78}(MAPbBr_3)_{0.14}(CsPbI_3)_{0.08}$.

In this thesis, for the conventional flat PSCs devices manufacture, $MAPbI_3$ perovskite was employed for mesoporous devices structure while CsFAMAPbIBr perovskite was chosen for planar devices structure. For nPSCs devices fabrication, both perovskites were used.

3.2.1.3 Hole Transport Layer Material

Normally, most highly efficient PSCs employ the small organic molecule 2,2',7,7'-Tetrakis[N,N-di(4-methoxyphenyl)amino]- 9,9'spirobifluorene (spiro-OMeTAD) as hole transport layer (HTL) material, which has a high hole conductivity, mobility and a suitable HOMO energy level.[211] In this thesis, the PSCs and nPSCs devices were prepared using spiro-OMeTAD as HTL.

The spiro-OMeTAD has been optimized by incorporating some additives, such as bis(trifluoromethylsulfonyl)amine lithium salt solution (LiTFSI) and tert-butylpiridine (TBP).[212–214] In addition to completing the function of HTL, the spiro-OMETAD serves the purpose (in the case of nPSCs devices) of covering and levelling the rough NAA surface.

Figure 3.12 displays an energy-level diagram of the distinct materials mentioned previously.

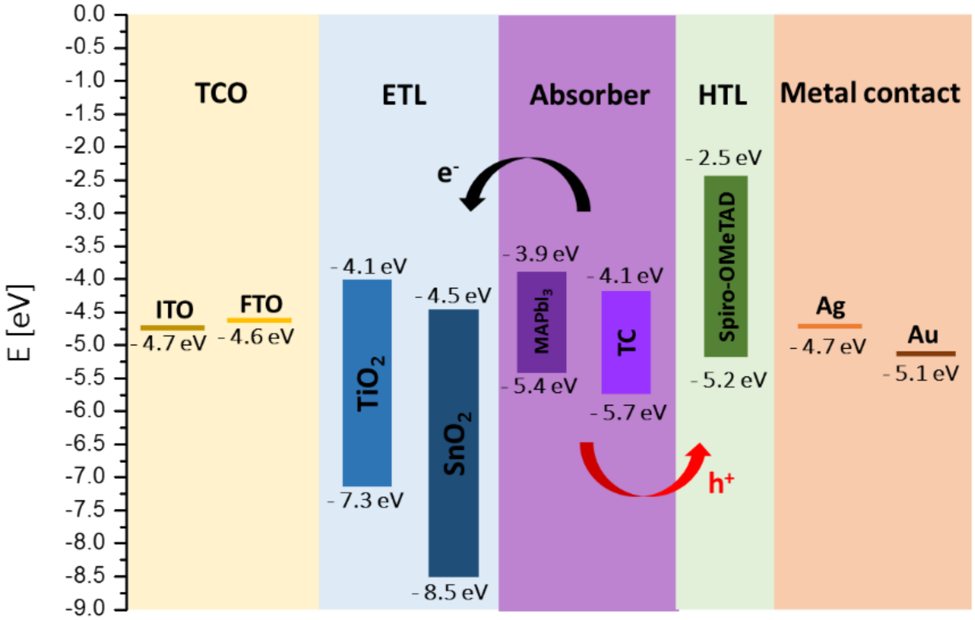

Figure 3.12. Energy-level diagram showing the valence band (VB) and conduction band (CB) levels of the different materials employed in this thesis for fabricating PSC and nPSC. TC: triple cation perovskite, $(FAPbI_3)_{0.78}(MAPbBr_3)_{0.14}(CsPbI_3)_{0.08}$. [175,201,204,215–220]

3.2.2 Fabrication Process Using $MAPbI_3$ as Absorber Layer

$MAPbI_3$ perovskite solar cells were fabricated using modifications of standard recipes.[127,221] Several mesoporous PSCs devices were prepared using fluorine-doped tin oxide (FTO) as the TCO, TiO_2 as ETL, $MAPbI_3$ perovskite as absorber layer, spiro-OMeTAD as HTL and Ag as back electrode contact.[222] **Figure 3.13** displays a schematic diagram of the mesoporous device structure.

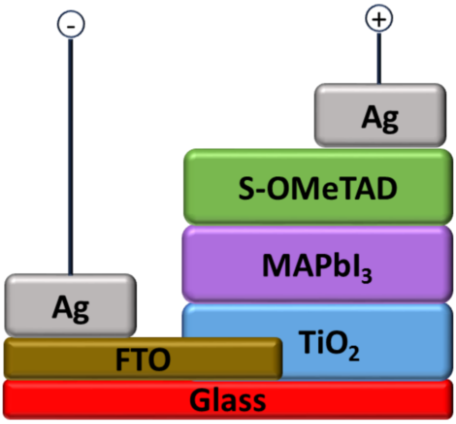

Figure 3.13. Schematic diagram of the mesoporous device using $MAPbI_3$. The dimensions of the layers do not correspond to their actual thicknesses.

3.2.2.1 Bottom Contact Cleaning

In a cleanroom, pre-patterned 1.5 × 1.5 cm FTOs were employed as substrates. All the substrates were carefully cleaned. First, they were brushed with a solution of Hellmanex soap in deionized water, and following they were cleaned with ultrasonication in three different solutions for 15 min each. The solutions were Hellmanex soap in deionized water, isopropanol and acetone. Then, the substrates were treated with a UVO cleaning system for 15 min. The substrates cleaning is a critical step as it could lead to unfavourable consequences in the final operation of the device and should be done carefully.

3.2.2.2 Titanium Dioxide as Electron Transport Layer

Over the previously cleaned FTOs substrates, three different TiO_2 layers were deposited.[223]

Compact Titanium Dioxide

First, a compact TiO_2 (c-TiO_2) layer was formed. A titanium diisopropoxide bis-(acetylacetonate) (0.3 M, $Ti(i\text{-}PrO)_2(acac)_2$) solution was prepared diluting 0.3 mL of $Ti(i\text{-}PrO)_2(acac)_2$ in 1.7 mL of anhydrous isopropanol and filtered (PTFE, 0.2 µm) just before its use. 40 µL of the filtered $Ti(iPrO)_2(acac)_2$ solution were deposited by spin-coating on the top of the previously cleaned FTO substrates at 4000 rpm (1000 rpm/s) for 25 s to obtain a c-TiO_2 film thickness between 20 nm and 30 nm. Then, the substrates were dried at 125 °C for 5 min and subsequently calcined at 450 °C for 30 min in a titanium hotplate.

Titanium Tetrachloride Solution

When the substrates had cooled down, after the previous calcination, they were immersed in the filtered (0.22 µm, PES) 40 mM titanium tetrachloride ($TiCl_4$) solution in 9% hydrochloric acid (HCl) at 70 °C for 30 min into a muffle oven. Then, the substrates were rinsed with water and C_2H_5OH and dried with a strong airflow.

Mesoporous Titanium Dioxide

Finally, to deposit the mesoporous TiO_2 (m-TiO_2) layer, a solution was prepared by diluting a commercial paste (30 nm particle size) in C_2H_5OH, with 1:7 weight ratio. It was left under stirred overnight to obtain a good solution. 40 µL of the m-TiO_2 solution were spin-coated at 6000 rpm (1000 rpm/s) for 30 s to obtain a m-TiO_2 film thickness between 100 nm and 150 nm. Then, the substrates were dried at 125 °C for 5 min and subsequently were calcined at 450 °C for 30 min in a titanium hotplate.

3.2.2.3 $MAPbI_3$ Perovskite as Absorber Layer

A 1.25 M $MAPbI_3$ precursor solution was prepared, in a N_2-filled glovebox, from its two precursors: lead iodide (PbI_2) and methylammonium iodide ($MeNH_3I$, MAI) using anhydrous dimethyl sulfoxide (DMSO) as the solvent.[224] To help the lead salt dissolution, 288.1 mg of PbI_2 were dissolved in 500 µl of DMSO heating it at 150 °C for 10 min in a hotplate, when the solution was a room temperature 99.35 mg of MAI were added.

$MAPbI_3$ precursor solution was filtered (0.2 µm, PTFE) just before its use. It was deposited, in a N_2-filled glovebox, by the anti-solvent method.[137] 40 µl of the $MAPbI_3$ precursor solution were dropped on the top of the previously deposited layer and the substrates were spin-coated with a two-step program. First, at 1000 rpm (500 rpm/s) for 10 s and then at 4000 (500 rpm/s) rpm for 30 s. 10 s before the spinning process ends 100 µl of anhydrous chlorobenzene were spin-coated right on the centre of the substrate. The substrates were moved directly from the spin coater to a hotplate at 100 °C and they were annealed for 45 min. The substrates turned dark brown during the first minute of the annealing process as can be seen in **figure 3.14**. The $MAPbI_3$ film thickness obtained was between 400 nm and 450 nm. The perovskite layer formation is the most critical step in PSCs fabrication. The deposition method requires practice since the anti-solvent step is crucial. The solvent deposition should be not done too fast or too slow since it could lead that some rings appear in the substrate.

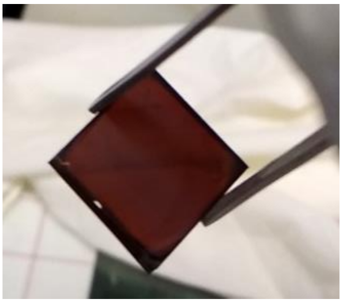

Figure 3.14. $MAPbI_3$ perovskite film photo.

3.2.2.4 Hole Transport Layer and Top Electrode

First, an additive solution was prepared. The additives used were the tert-butylpiridine and a bis(trifluoromethylsulfonyl)amine lithium salt (LiTFSI) solution, which was prepared by mixing 520 mg of LiTFSI in 1 mL of anhydrous acetonitrile. The additive solution was made by adding 38.7 µL of tert-butylpiridine to 1 mL of anhydrous chlorobenzene, then 23.7 µL LiTFSI solution were added. Secondly, a 60 mM spiro-OMeTAD solution was prepared by dissolving 73 mg of spiro-OMeTAD in 1 mL of the additive solution.[225] Subsequently, the solution was vigorously stirred and filtered (0.2 µm PTFE filter) before its deposition. Finally, the solution was deposited dynamically by spin-coating.[226] 30 µL of 60 mM spiro-OMeTAD solution were dropped, in a N_2-filled glovebox, on the top of the previous layer deposited and the substrates were spin-coated at 4000 rpm for 30 s, to obtain a thickness between 150 nm and 200 nm.[225] Subsequently, FTO contact was cleaned on two edges scratching away spiro-OMeTAD and $MAPbI_3$, then the edges were further cleaned with swabs lightly wet with anhydrous DMSO and immediately with anhydrous acetonitrile to remove DMSO vapours since they can damage the perovskite layer. To increase the oxidative doping of the HTL, substrates were kept in dark in a dry air chamber overnight before the thermal evaporation of the top electrode.[227]The next day the substrates were placed into the thermal evaporation chamber (vacuum pressure < $5x10^{-6}$ torr, in an N_2-filled glovebox) and 120 nm of silver (Ag) were thermally evaporated using a shadow mask leading to 4 diodes for substrate each with an active area of 9 mm^2.

3.2.3 Fabrication Process Using CsFAMAPbIBr as Absorber Layer

CsFAMAPbIBr perovskite solar cells were manufactured employed variations of standard recipes.[228,229] Several mesoporous PSCs devices were produced using ITO as TCO, SnO_2 as ETL, CsFAMAPbIBr perovskite as absorber layer, spiro-OMeTAD as HTL and Au as back contact. **Figure 3.15** displays a schematic diagram of the planar device.

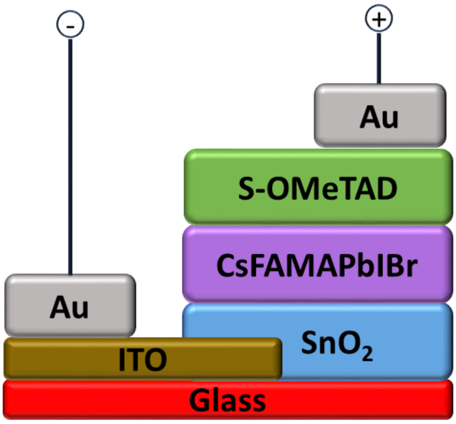

Figure 3.15. Schematic diagram of the planar device. The dimensions of the layers do not correspond to their actual thicknesses.

3.2.3.1 Bottom contact Cleaning

In a cleanroom 2.54 x 2.54 cm ITO (indium tin oxide) coated glasses were uses as substrates. The commercial ITO substrates were undergone pre-treatment before the cleaning. The ITO thin film was patterned by laser scribing lines. The pattern was performed with these conditions: 50 % power, 1000 mm/s, 55 kHz, to remove an ITO portion of each cell. Afterwards, the substrates should be blown with airflow to remove the generated dust in this process. **Figures 3.16 a)** and **b)** exhibit a commercial ITO coated glass pictures before and after the annealing pattern, respectively. The ITO film is represented by green and the removed ITO portion by white. Subsequently, all the substrates were carefully cleaned as is explained in section **3.2.2.1**.

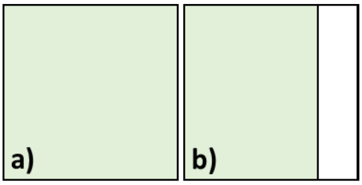

Figure 3.16. Commercial ITO coated glass **a)** before and **b)** after annealing pattern. The ITO film is represented by green.

3.2.3.2 Tin dioxide as Electron Transport Layer

Over the previously cleaned ITOs substrates, a tin dioxide (SnO_2) thin layer was deposited by a two-step method described by Anaraki *et al.*[230]

Tin Dioxide Chemical Bath Deposition

First, Tin (II) chloride dehydrate (0.048 M, $SnCl_2{\cdot}2H_2O$) solution was prepared by diluting 28 mg of $SnCl_2{\cdot}2H_2O$ in 2.54 mL of isopropanol previously filtered. 80 µl of the filtered $SnCl_2{\cdot}2H_2O$ solution were spin-coated on the top of previously cleaned ITO substrates at 3000 rpm (1000 rpm/s) for 30 s to obtain a SnO_2 film thickness about 30 nm. Afterwards, they were annealed at 180 °C for 1 h in a hotplate. Subsequently, the substrates were submerged for 3 h in a chemical bath at 70 °C (muffle oven) composed of 2.5 g of urea, 50 µL of 3-mercaptopropionic acid, 2.5 mL of HCl and 540 mg of $SnCl_2{\cdot}2H_2O$

in 200 mL of deionized water. Then, substrates were washed with deionized water and dried with an airflow. It is crucial to wash the substrates with a lot of water and dry it well to avoid the appearance of white spots on the substrate surfaces. Finally, the substrates were annealed at 180 °C for 1 h in a hotplate.

3.2.3.3 CsFAMAPbIBr Perovskite as Absorber Layer

The triple-cation caesium formamidinium methylammonium lead iodide bromide (CsFAMAPbIBr) perovskite was prepared in a N_2-filled glovebox, following the method described J.Tirado *et al*.[229], from its precursors: lead iodide (PbI_2), lead bromide ($PbBr_2$), formamidinium iodide (FAI), methylammonium bromide (MABr) and caesium iodide (CsI). The solvents used were anhydrous DMF and anhydrous DMSO.

A 1.3 M CsFAMAPbIBr perovskite precursor solution was prepared as it is summarized in **figure 3.17**. In a vial (V_1) 636 mg of PbI_2 and 85 mg of $PbBr_2$ were mixed in 1 mL of a mixture of DMF and DMSO with a volume ratio of 4:1. In a vial (V_2) 226 mg of FAI and 26 mg of MABr were added. Then, V_1 was dropped in V_2 (solution *a,* S_a). In a vial (V_3) 265 mg of PbI_2 were stirred in 500 µL of DMSO and in a vial (V_4) 149 mg of CsI were weighed. After, V_3 was dropped in V_4 (solution *b,* S_b). Finally, in a vial (V_5) 1.2 mL of S_a and 0.12 mL of S_b were mixed to have the triple-cation perovskite precursor solution. The resulting stoichiometry is $(FAPbI_3)_{0.78}(MAPbBr_3)_{0.14}(CsPbI_3)_{0.08}$.

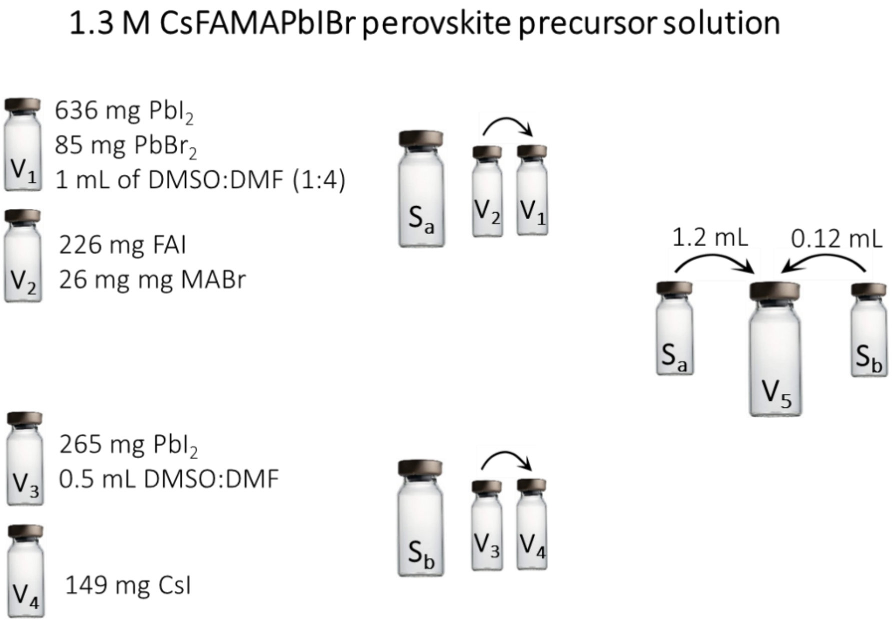

Figure 3.17. Steps diagram to prepare a 1.3 M CsFAMAPbIBr perovskite precursor solution.

Before the CsFAMAPbIBr perovskite precursor deposition, the substrates were treated with a UVO system at 50 °C for 15 min. The CsFAMAPbIBr perovskite precursor solution was deposited, in a dry-box, by the anti-solvent method[137] and it was filtered (PTFE, 0.2 µm) just before its use. 45 µL of the solution were dropped on the top of the previously deposited layer and the substrates were spin-coated with a two-step program, first at 2000 rpm (200 rpm/s) for 12 s and then 5000 rpm (2000 rpm/s) for 25 s. In this step, 120 µL of anhydrous chlorobenzene were dropped 9 s before the end of the process. Then, the substrates were moved directly from the spin coater to a hotplate and they were annealed at 100 °C for 1 h. The substrates turned dark brown during the first minute of the annealing process as can be observed in **figure 3.18**. The CsFAMAPbIBr film thickness obtained was about 500 nm. The perovskite layer formation is the most critical step in PSCs fabrication. The deposition method requires practice since the anti-solvent step is crucial. The solvent deposition should be not done too fast or too slow since it could lead that some rings appear in the substrate.

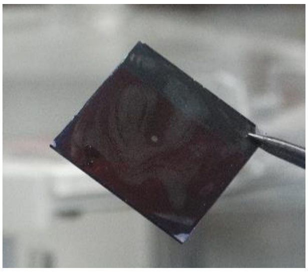

Figure 3.18. CsFAMAPbIBr perovskite film photo.

3.2.3.4 Hole Transport Layer and Top Electrode

First, an additive solution was prepared by adding 28 µL of tert-butylpiridine to 1 mL of anhydrous chlorobenzene, then 16 µL LiTFSI solution were added. Secondly, a 70 mM spiro-OMeTAD solution was prepared by dissolving 70 mg of spiro-OMeTAD in 1 mL of the additive solution.[229] Subsequently, the solution was vigorously stirred and filtered (0.2 µm PTFE filter) before its deposition. Finally, the solution was deposited dynamically by spin-coating. 50 µL of 70 mM spiro-OMeTAD solution were deposited, in a N_2-filled glovebox, on the top of the previous layer deposited and the substrates were spin-coated at 4000 rpm for 20 s to obtain thickness between 100 nm and 300 nm.[229] Subsequently, the substrates were patterned by laser scribing to remove all the layers of the device except the ITO in a specific area of the substrate, to facilitate the contact with the metal electrode. The conditions of the laser scribing were 5% power, 3000 mm/s, 55 kHz. To increase the oxidative doping of the HTL, substrates were kept in dark in a dry air chamber overnight before the thermal evaporation of the top electrode.[227] The next day the substrates were placed into an ultra-high vacuum chamber and 70 nm of gold were deposited by thermal evaporation using a shadow mask leading to 5 diodes for substrate each with an active area of 0.19 cm^2.

3.2.4 Basic Electrical Characterization

The current density-voltage (*JV*) characteristics of PSCs were measured in dark and under simulated AM1.5G illumination (100 mW/cm^2). The $MAPbI_3$ and CsFAMAPbIBr best-performing devices *J-V* characteristics are shown in the **figures 3.19** and **3.20**, respectively. All the *J-V* measurements were carried out under light and nitrogen conditions ($O_2 < 0.1$ ppm and $H_20 < 0.1$ ppm).

As expected, some hysteresis (difference between forward and reverse scan) is observed for all evaluated systems. This phenomenon has been reported elsewhere for n-i-p PSC and is attributed to ion migration inside perovskite material and especially to the formation and the release of interfacial charges in both electron and hole transporting layer contacts.[231,232] Also, as expected the performance values measured with devices prepared under identical conditions present a small difference. This phenomenon has been informed elsewhere for n-i-p PSC and is attributed to the sensibility of the drying and crystallization steps of the perovskite absorber synthesis.[233–235] The performance parameters values of the $MAPbI_3$ and CsFAMAPbIBr devices are summarized in **tables 3.1** and **3.2**, respectively.

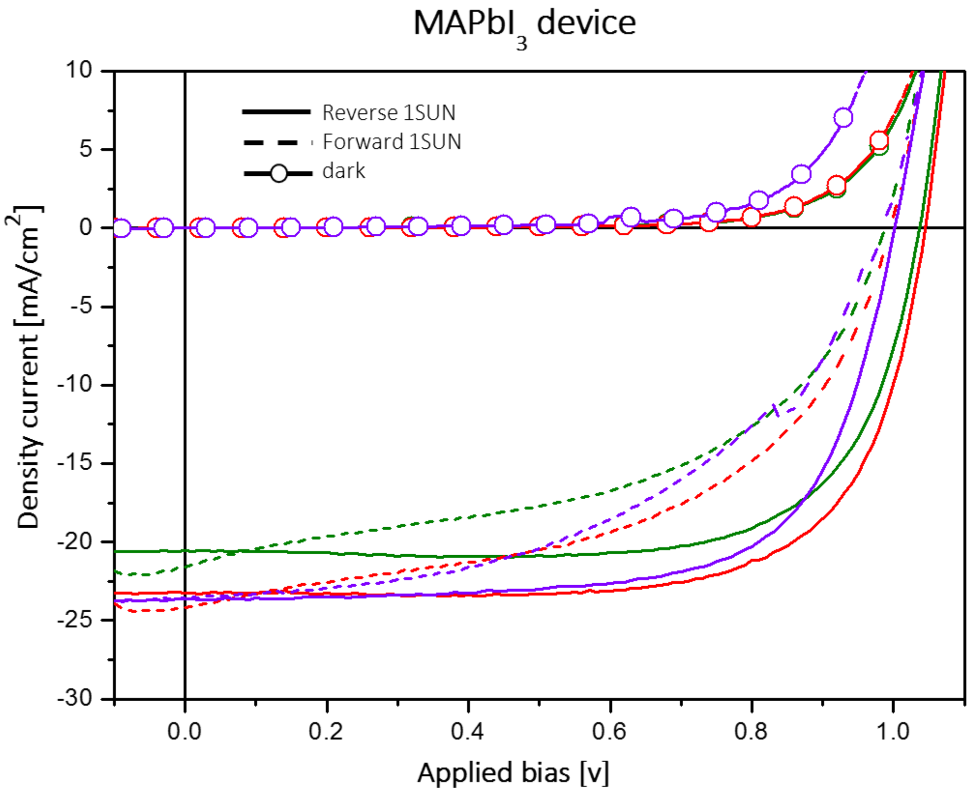

Figure 3.19. Current density *vs* voltage (*JV*) characteristics of the best performing MAPbI$_3$ devices in dark (hollow markers) and under simulated A.M. 1.5G illumination (100 mW/cm^2). The solid and dashed lines correspond to the reverse and forward scans, respectively.

Device	Sweep	V_{oc} [V]	J_{sc} [mA/cm]	FF [%]	PCE [%]
Green	Reverse	1.04	20.5	72	15.3
	Forward	0.99	21.6	50	10.6
Red	Reverse	1.04	23.2	71	17.2
	Forward	0.99	24.2	71	12.3
Purple	Reverse	0.99	23.6	69	16.2
	Forward	0.99	23.5	48	11.2

Table 3.1. Primary performance parameters values of the best-performing $MAPbI_3$ devices measured at 1 SUN A.M. 1.5 illumination (100 $mWcm^{-2}$). V_{oc}: open-circuit voltage, J_{sc}: short circuit current density, FF: fill factor and PCE: power conversion efficiency.

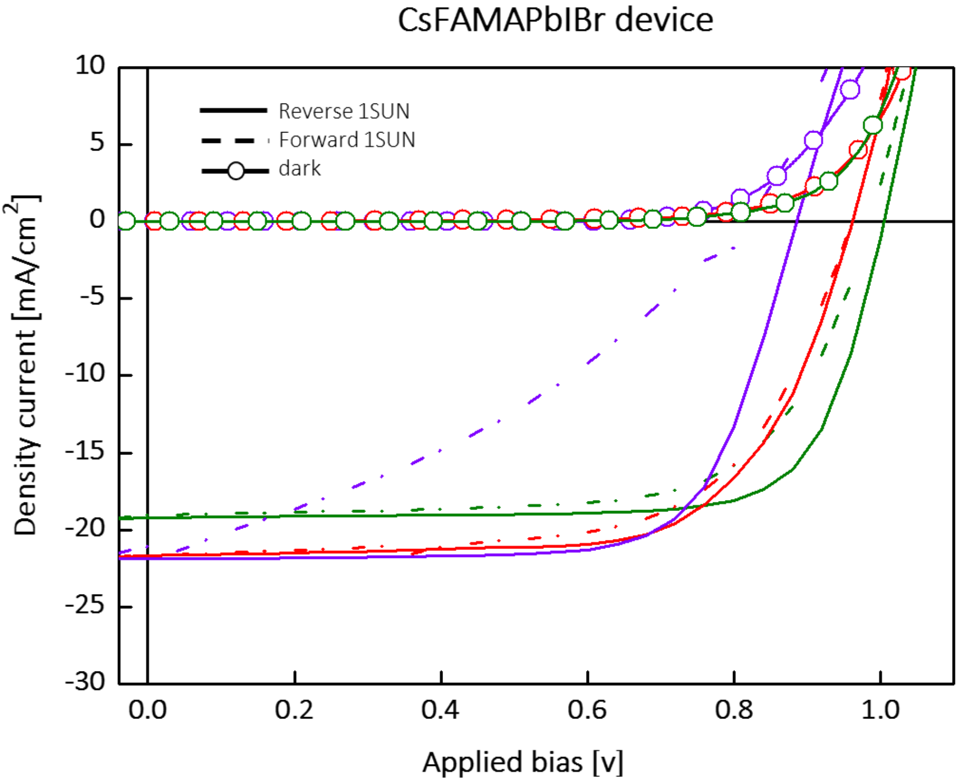

Figure 3.20. Current density *vs* voltage *(JV)* characteristics of the best performing CsFAMAPbIBr devices in dark (hollow markers) and under simulated A.M. 1.5G illumination (100 mW/cm^2). The solid and dashed lines correspond to the reverse and forward scans, respectively.

Device	Sweep	V_{oc} [V]	J_{sc} [mA/cm]	FF [%]	PCE [%]
Green	Reverse	1.01	19.22	66	12.73
	Forward	0.98	19.07	77	14.61
Red	Reverse	0.96	21.68	64	13.31
	Forward	0.96	21.36	66	14.01
Purple	Reverse	0.88	21.07	33	6.19
	Forward	0.96	21.36	69	13.89

Table 3.2. Primary performance parameters values of the best-performing CsFAMAPbIBr devices measured at 1 SUN A.M. 1.5 illumination (100 mW/cm^2). V_{oc}: open-circuit voltage, J_{sc}: short circuit current density, FF: fill factor and PCE: power conversion efficiency.

Chapter 4

Thick Barrier Layer Removal in Nanoporous Anodic Alumina

In the following chapter, a new method for the removal of the thick barrier layer in nanoporous anodic alumina without removing the aluminium substrate is bestowed. It is based on a re-anodization step at a constant current density combined with chemical etchings. This chapter is based on published work: M.P. Montero-Rama, *et al.* 2019, In-situ removal of thick barrier layer in nanoporous anodic alumina by constant current Re-anodization. Surface and Coatings Technology, 380, 125039. DOI: 10.1016/j.surfcoat.2019.125039.

4.1 Introduction

Nanoporous anodic alumina (NAA) has attracted a great deal of interest in the last decades, due to its stability, cost-effective scalable production and the ability to fabricate nanopores with a wide range of thicknesses, diameters and interpore distances, allows to easily adapt them to new applications.[236,237] One remarkable NAA application is its use as a template for nanostructuring materials by infiltration of a specific material[238–240] (organic, inorganic, metallic, etc.) into NAA and following of removing NAA, can be obtained an inverse replica of NAA.[241,242] For example, NAA templates have been successfully used for nanostructuring polymer solar cells resulting in improved conductivity as compared with thin films of the same polymer.[243,244]

Since NAA is obtained by anodizing aluminium, the aluminium substrate can be used as an electrode. However, the presence of a continuous insulation barrier layer between the material infiltrated in the nanopores and the aluminium substrate, limits its applications for energy storage devices (batteries, supercapacitors), energy generation devices (photovoltaic solar cells), optoelectronic devices (LEDs, photodetectors), electrodeposition of metals where the materials infiltrated in NAA layer need to be electrically connected to the electrode.

In previous works, researchers have described procedures based on successive re-anodization (constant current density or stepwise voltage decrease) and chemical etching steps, that partially address this problem.[245,246] However, only procedures for the selective barrier layer removal in NAA with nanopores diameters up to 100 nm (NAA obtained with oxalic and sulphuric acid electrolytes) have been published to date. These methods fail for NAA obtained with phosphoric acid electrolytes. This is because phosphoric acid electrolytes (as well as other electrolytes that require higher anodization voltages) lead to barrier layer thicknesses of more than 200 nm.

Therefore, our attention was turned to a constant current re-anodization process originally described by Gösele and co-workers.[247] In their work, they achieved thinning the barrier layer of oxalic acid-made NAA by applying a chemical etching procedure after the second anodization step to decrease the thickness of the barrier layer and subsequently, applying two consecutive constant current anodization steps. Fixing the anodization current induces pore growth under out-of-equilibrium conditions, resulting in branchings at the bottom of the pores without reaching steady pore growth. This produced a sufficiently branched barrier layer allowing for the AC electrodeposition of metals. However, although the current is assumed to cross the porous layer no attempt was made to fully remove it.

In this work, a complete procedure to obtain mechanically stable NAA on aluminium substrates without a barrier layer and electrical contact between aluminium and the interior of the nanopores is presented. The procedure is based on a constant current re-anodization that results in the formation of branchings into the barrier layer that permits its selective removal in a final etching step.

4.2 Experimental

4.2.1 Partial Barrier Layer Etching

NAA samples, prepared in the previous chapter (section 3.1.2), were used as substrates to remove its barrier layer. NAA substrates were immersed in an etching solution (H_3PO_4, 4% wt.) for 1 h and at a temperature of 35 °C. With this chemical etching, the thickness of the barrier layer was reduced from 200 nm in the as-produced samples to a final thickness of approximately 80 nm. This step is crucial for the subsequent re-anodization step to ensure the establishment of the current through the barrier layer at an anodization potential smaller than the first and second step. Notice that this process also results in a reduction of the pore wall thickness, but only partially to maintain the structural stability of the porous structure.

4.2.2 Re-Anodization Step

The re-anodization step consists in a third anodization step in the same electrolyte as the first and second anodization steps (H_3PO_4, 1% wt.) at -3,5 °C, but at a constant anodization current density (re-anodization current density, I_{rndz}) instead of a constant anodization voltage.

The area of a sample exposed to the electrolyte was 1.76 cm^2. The effect of this re-anodization step on the morphology of the barrier layer is analysed and the optimal conditions that allow the removal of the barrier layer while maintaining the porous structure in contact with the aluminium substrate are determinate. For this reason, five different re-anodization current densities were tested: I_{rndz} = 568.2 $\mu A/cm^2$, I_{rndz} = 170.5 $\mu A/cm^2$, I_{rndz} = 113.6 $\mu A/cm^2$, I_{rndz} = 56.8 $\mu A/cm^2$, I_{rndz} = 5.7 $\mu A/cm^2$. After these tests, the procedure was further optimized by testing two more re-anodization current densities values: $I_{rndz} = 28.4\ \mu A/cm^2$ and $I_{rndz} = 17.0\ \mu A/cm^2$.

4.2.3 Final Barrier Layer etching

As it will be demonstrated in the results and discussion section, at certain re-anodization current densities branchings were created through the barrier layer. Such branchings permit a fast dissolution of the remaining barrier layer after a final etching step, consisting in immersing the sample in H_3PO_4 (4% wt.) solution at 35 °C for a controlled time of 38 min to remove completely the barrier layer. The time length of this step is important to keep the porous structure and its contact with the aluminium substrate. For etching times bigger than this value, pore walls are dissolved by the etching procedure.

To demonstrate that the barrier layer was removed and there is an electric contact between the aluminium and the pore bottom the current-voltage characteristics of two distinct substrates (with and without barrier layer) were measured in an electrochemical cell with a conductive electrolyte.

4.3 Results and Discussions

4.3.1 Partial Barrier Layer Etching

The barrier layer thickness of the nanopores obtained with the H_3PO_4 electrolyte after the second anodization step was found to be too thick to be removed directly after pore growth using any reported procedure. To reduce the barrier layer, the samples were etched in a solution of H_3PO_4 at 4% wt. at a temperature of 35 °C and for 1 h. The etching conditions were established after several tests and found to give optimum results when the barrier layer was reduced to 80 nm.

Figure 4.1 a) and **b)** show the cross-section SEM views of NAA obtained after the second anodization step. From **figure 4.1 b)** the thickness of the barrier layer was estimated to be about 200 nm while the pore diameter was estimated to be about 150 nm. **Figure 4.1 c)** and **d)** show the cross-section SEM views of NAA after the chemical etching step, where the thickness of the barrier layer and the pore diameter were now about 80 nm and 350 nm respectively.

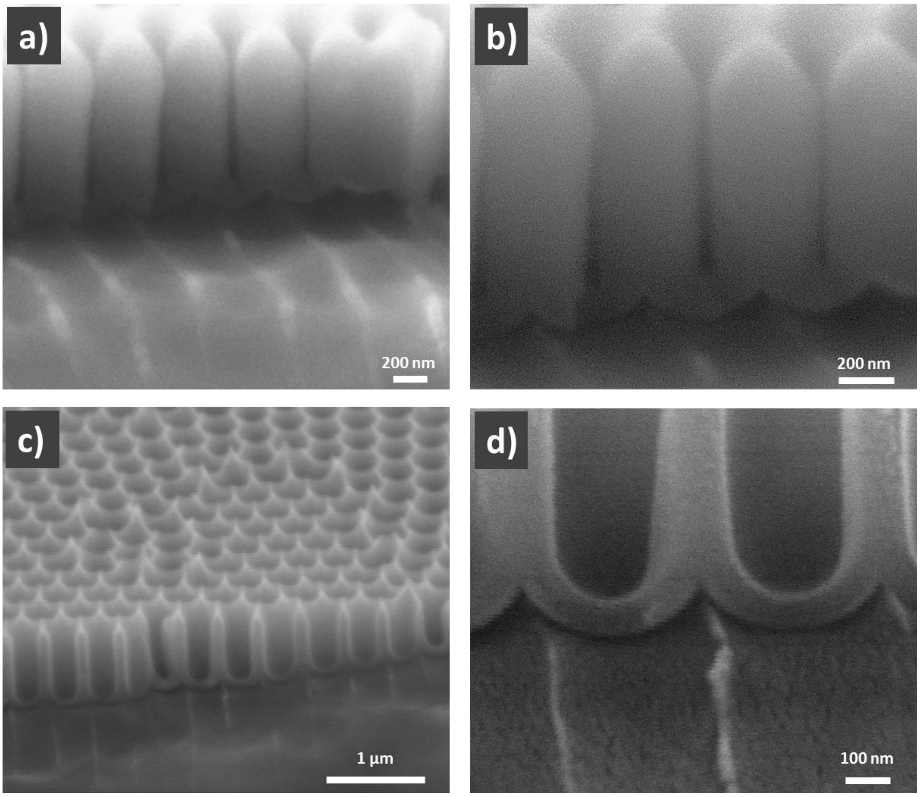

Figure 4.1. a) Cross-section SEM view of a phosphoric NAA after the second anodization step. **c)** Cross-section SEM view of a phosphoric NAA after the partial chemical etching. **b)** and **d)** are the magnification views of **a)** and **b)** respectively. The scale bars are indicated in each picture.

For etching times bigger than 38 min, nanopore walls are dissolved by the etching procedure as **figure 4.2** exhibits.

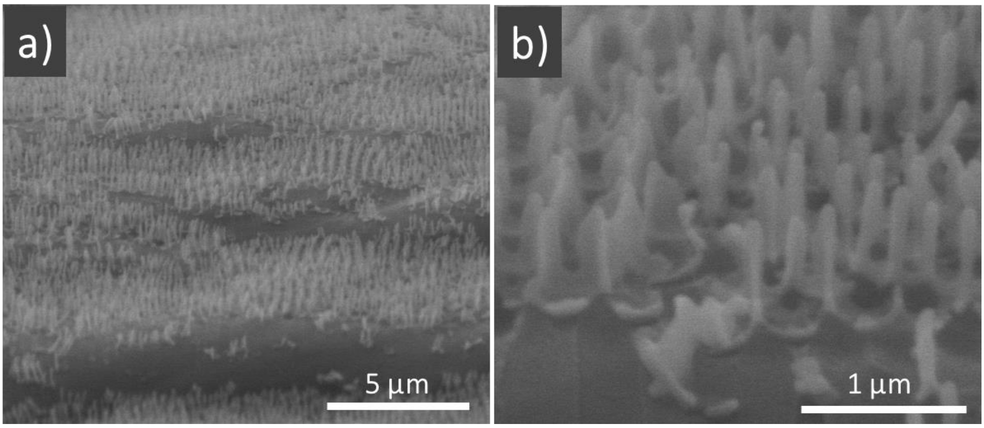

Figure 4.2. a) Cross-section SEM view of the nanopores dissolves after the final barrier layer etching with a time over than 38 min. **b)** Magnification view of **a)** The scale bars are indicated in each picture.

4.3.2 Re-Anodization Step

To determine the optimal conditions for the re-anodization step, several experiments were conducted for different values of current density. The first experiment was conducted at a constant current density about one order of magnitude lower than the current density reached at the end of the second anodization step (constant anodization voltage of 195 V). Thus, since the current density at the end of the second anodization step is 5682.1 μA/cm^2 the first re-anodization experiment was conducted at I_{rndz} = 568.2 μA/cm^2.

Figure 4.3 shows the measured voltage for I_{rndz} = 568.2 μA/cm^2. The voltage undergoes a small transient decrease for 1 s, followed by an increase with an almost constant rate of 162 mV/s. Since the objective of this re-anodization is the reduction of the measured voltage, this experiment was stopped after 46 s.

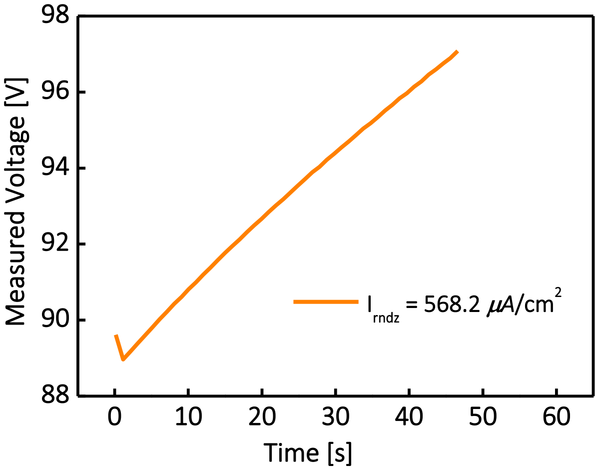

Figure 4.3. Measured voltage *vs* time for I_{rndz} = 568.2 µA/cm^2.

The behaviour of the measured voltage for I_{rndz} = 170.5 μA/cm^2 (**figure 4.4**) and 113.6 μA/cm^2 (**figure 4.5**) is similar to the previous result with the only difference that the rates of voltage increase are 47 mV/s and 9 mV/s, respectively.

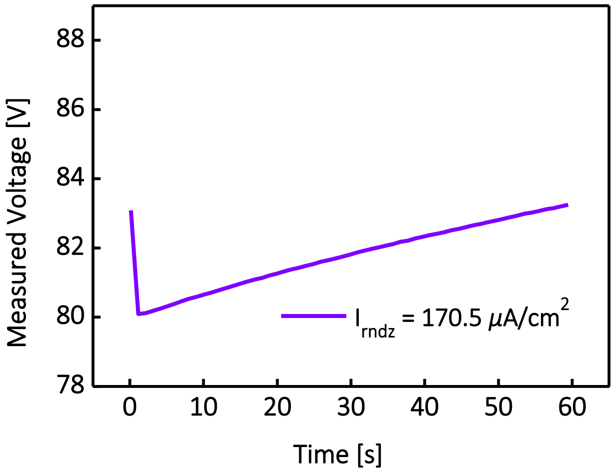

Figure 4.4. Measured voltage *vs* time for I_{rndz} = 170.5 µA/cm^2

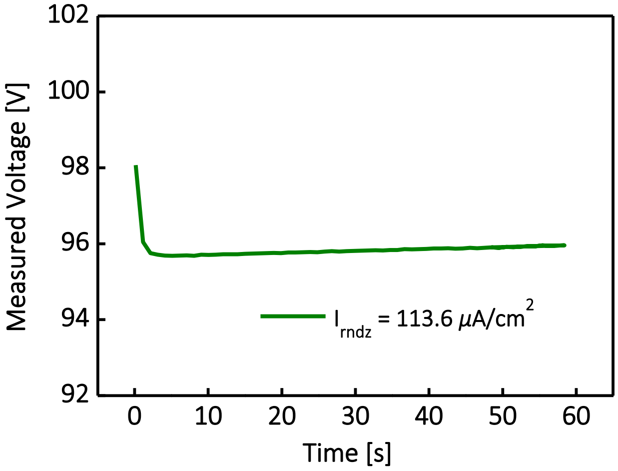

Figure 4.5. Measured voltage *vs* time for I_{rndz} = 113.6 µA/cm^2.

When the re-anodization current density was further reduced, however, i.e., I_{rndz} = 56.8 μA/cm^2 (**figure 4.6**), the measured voltage shows a completely different trend: first, the potential shows a fast increase from 78 V to 96 V in 1.2 s, then drops to 95 V in 0.9 s and finally starts to decrease slowly, with a rate almost constant of 14 mV/s.

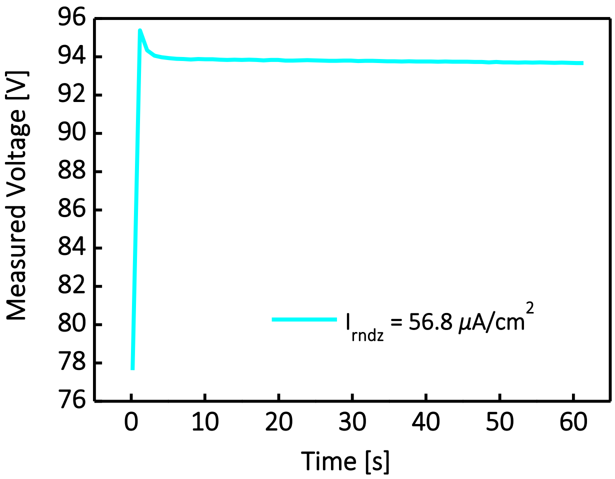

Figure 4.6. Measured voltage *vs* time for I_{rndz} = 56.8 μA/cm^2

If the constant re-anodization current density is further reduced, for I_{rndz} = 5.7 μA/cm^2 [**figure 4.7 a)**] the measured voltage experiences a sharper increase at the beginning in a brief period (from 10 V up to 65 V in 7.1 s) and then it decreases with a constant rate of 29 mV/s until stabilizes reaching values close to zero in 7 h. **Figure 4.7 b)** shows the cross-section SEM view of a sample after re-anodization performed with I_{rndz} = 5.7 μA/cm^2. The picture shows that small branchings have grown through the barrier layer. The branchings appear distributed non-homogeneously at the bottom of the pores.

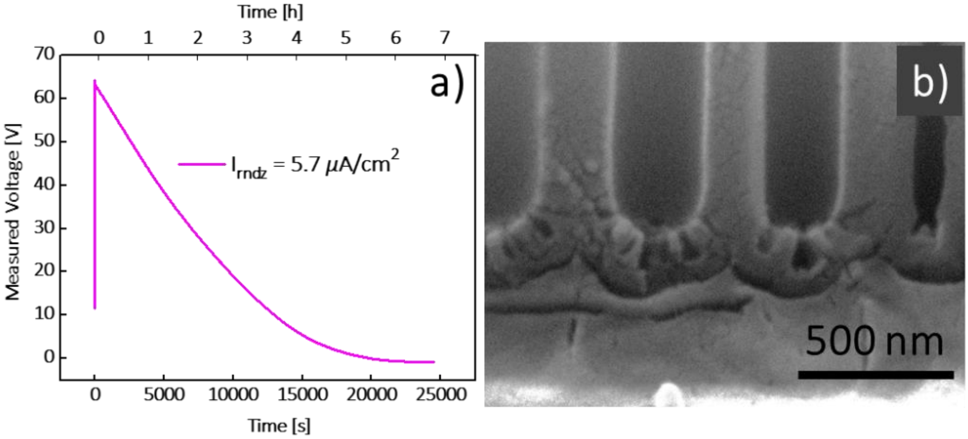

Figure 4.7. a) Measured voltage *vs* time and **b)** cross-section SEM view of NAA for I_{rndz} = 5.7 µA/cm^2. The scale bar is indicated in the picture.

The previous tests can be classified into two main groups: for re-anodization current densities above 56.8 μA/cm^2 the measured voltage increases with the application of a constant re-anodization current density, while for current densities below 56.8 μA/cm^2 the trend is opposite i.e. the measured voltage decreases.

Taking into account that the barrier layer thickness is proportional to the anodization voltage,[94,237] the increase in measured voltage for the current densities higher than 56.8 μA/cm^2 (**figures 4.3**, **4.4** and **4.5**) is indicating that the barrier layer thickness is increased. This can be explained by the fact that the current density applied is high enough to produce the generation of oxide at the oxide-metal interface at a higher rate than the dissolution at the electrolyte-oxide interface. On the other hand, when the current density is small enough [**figures 4.6** and **4.7 a)**] the rate of oxide generation is limited by the current density applied and the dissolution is promoted. The SEM view in **figure 4.7 b)** indicates that the dissolution of the alumina takes place locally at points distributed on the surface of the pores' bottom, resulting in the formation of small branchings that penetrate through the barrier layer.

The procedure was further optimized by testing two more re-anodization current densities values: I_{rndz} = 28.4 μA/cm^2 and I_{rndz} = 17.0 μA/cm^2.

Figure 4.8 a) corresponding to I_{rndz} = 28.4 μA/cm^2 shows a measured voltage increases over a short period, and then it decreases to values close to 0 V. The behaviour of the measured voltage is similar to that recorded for I_{rndz} = 5.7 μA/cm^2, with the difference that the measured voltage reaches a constant threshold after 9 h instead of 7 h. The voltage decrease has an average rate of 12 mV/s. The process was carried out over 12 h. Interestingly, SEM views [**figure 4.8 b) and c)**] of the corresponding re-anodization process show similar branchings as those formed for I_{rndz} = 5.7 μA/cm^2 with the difference that in this case, the branchings go through the barrier layer and continue growing into the aluminium substrate [Shown by the red arrows in **figure 4.8 c)**].

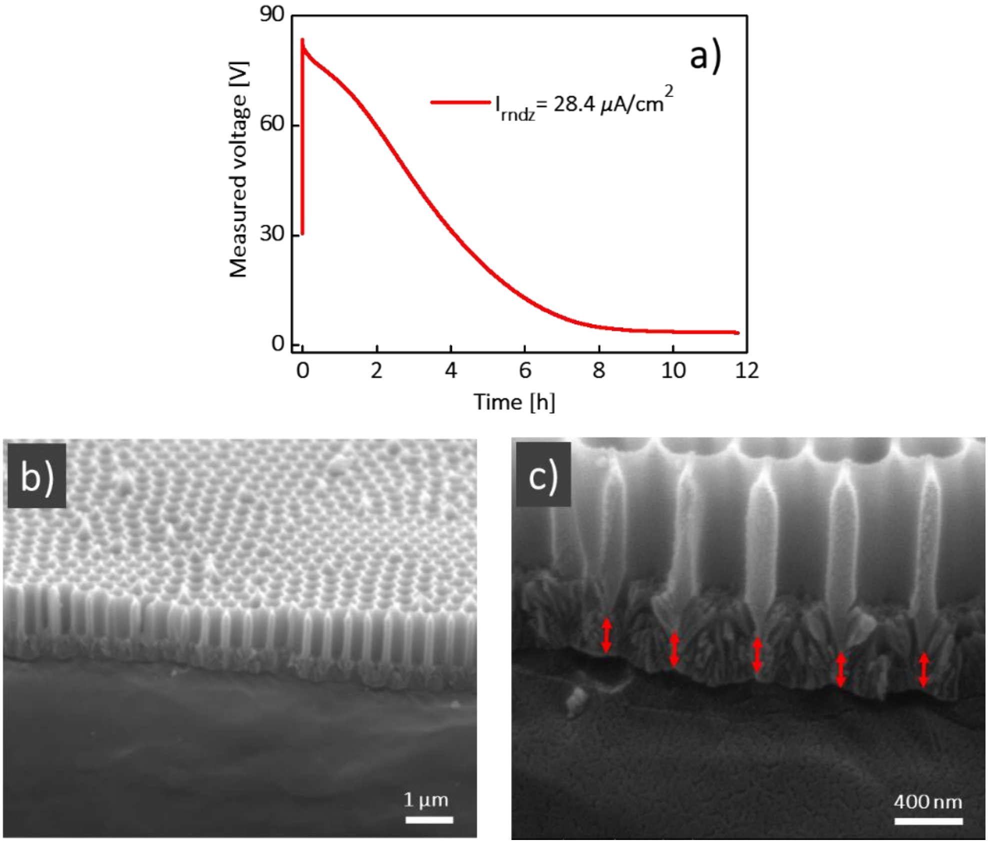

Figure 4.8. a) Measured voltage *vs* time corresponding to I_{rndz} = 28.4 μA/cm^2. **b)** Cross-section SEM view for this value of current density. **c)** Magnification view of **b)** with the growth of the branchings into the aluminium, which is mark by red arrows. The scale bars are indicated in each picture.

In **figure 4.9 a)**, the measured voltage for I_{rndz} = 17.0 µA/cm^2 shows a similar behaviour as in the previous I_{rndz} = 5.7 μA/cm^2 and I_{rndz} = 28.4 μA/cm^2. It increases up to about 80 V and then decreases with a constant rate of 0.96 mV/s. The process was stopped after 5.5 h to avoid the growth of additional oxide, as observed in **figure 4.8 c)**. SEM views [**figure 4.7 b)** and **4.8 c)**] for I_{rndz} = 5.7 μA/cm^2 and I_{rndz} = 28.4 μA/cm^2 respectively, show branchings in the alumina barrier layer. The main difference with the I_{rndz} = 5.7 μA/cm^2 current density is that in this case branchings are uniformly distributed on the pores' bottom. On the other hand, if compared with I_{rndz} = 28.4 μA/cm^2, branchings grow only through the barrier layer and do not penetrate on the aluminium substrate. It is also important to point out that the re-anodization at this current density, for such time, leaves points of contact between the oxide and the metallic aluminium substrate. (indicated by blue arrows in **figure 4.9 c)**. Such points are crucial to avoid the detachment of the porous oxide from the aluminium substrate when the subsequent etching step is applied.

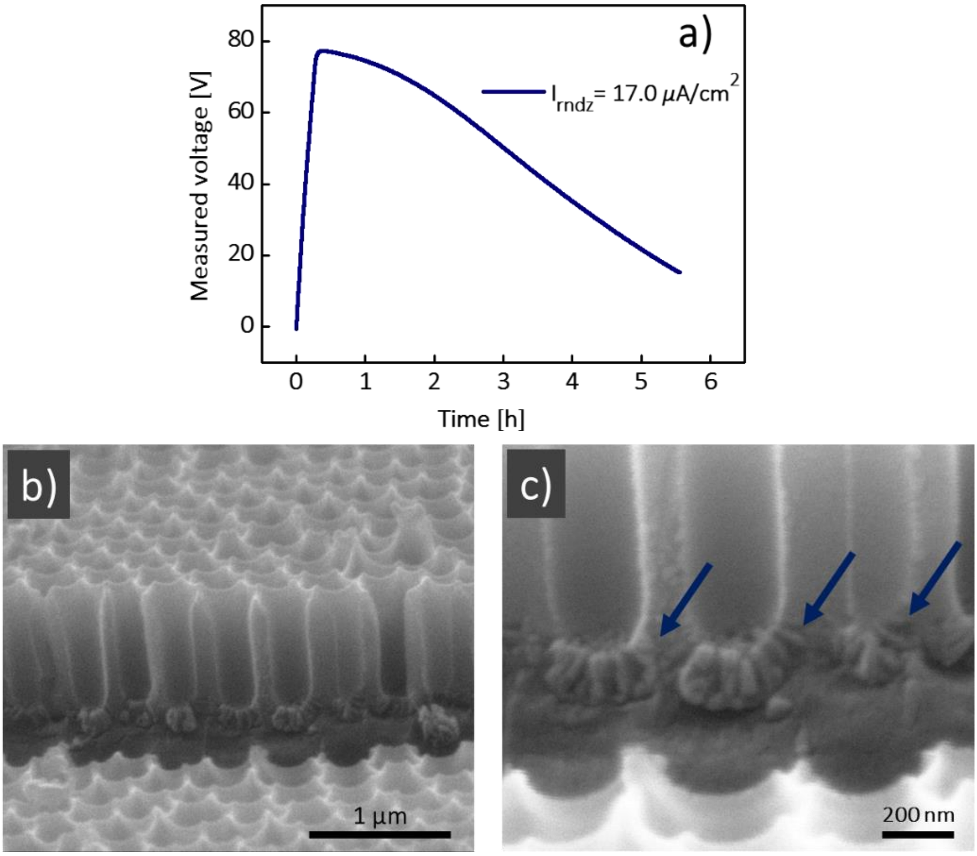

Figure 4.9. **a)** Measured voltage *vs* time for I_{rndz} = 17.0 μA/cm^2. **b)** Cross-section SEM view of NAA for this value of current density. **c)** Magnification view of **b)** with the point of contact between the oxide and the aluminium marked by the blue arrows. The scale bars are indicated in each picture.

4.3.3 Final Barrier Layer Etching

Figure 4.10 shows SEM views of the resulting NAA after applying a chemical etching step as described in the experimental section to a sample produced by a re-anodization current density of $I_{rndz} = 17.0\ \mu A/cm^2$. For this sample, the re-anodization process was stopped after 5.5 h and the chemical etching was applied for 38 min. **Figure 4.10 a)** and **b)** correspond to a cross-section from different view angles, while the **figure 4.10 c)** corresponds to a top-view. Finally, **figure 4.10 d)** and **e)** show the cross-section SEM view of NAA together with the aluminium substrate. In **figure 4.10 a)** the green arrows point to the pore's bottom showing that the barrier layer has been removed. **Figure 4.10 b)** corresponds to a flake detached from the aluminium surface, allowing for a high-contrast picture of the lower part of the pores clearly showing the absence of the barrier layer at the pores' bottom. The top-view SEM view in **figure 4.10 c)** shows that the pore wall thickness has been also reduced by the final chemical etching step, but it is thick enough to ensure structural stability. Finally, the cross-section views in **figures 4.10 d)** and **e)** show that the nanopores are completely open at their bottoms permitting the electric contact of any substance in the pore interior with the aluminium substrate while maintaining adhesion with the substrate.

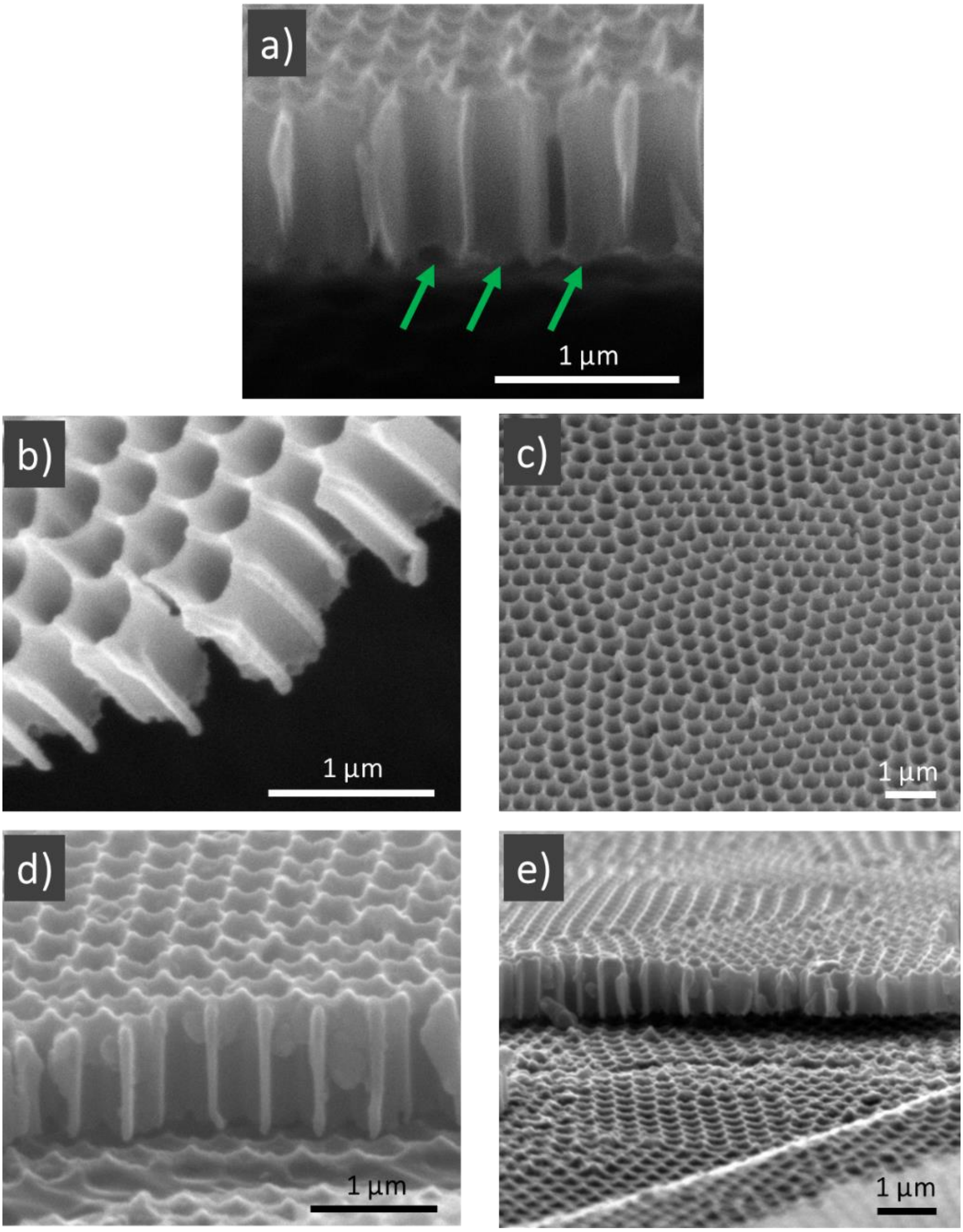

Figure 4.10. **a)** and **b)** cross-section and **c)** top SEM view of NAA after a chemical etching of NAA samples obtained with a I_{rndz} = 17.0 µA/cm^2. **d)** and **e)** Cross-section SEM view of the porous anodic alumina together with the aluminium substrate. The scale bars are indicated in each picture.

Figure 4.11 exhibits the measured current *vs* applied voltage of several NAA substrates with and without barrier layer. Measured current values of NAA are almost 0 mA while measured current values of wBL-NAA vary between -5 and 8 mA. Thus, demonstrating that there is an electric contact between aluminium and the pore bottom and therefore will be an electric contact between a conductor material infiltrated within wBL-NAA and the aluminium.

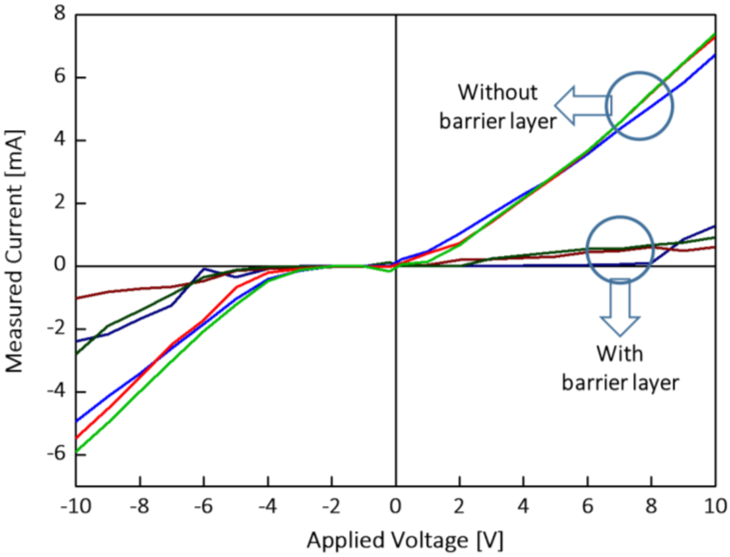

Figure 4.11. Measured current *vs* applied voltage of NAA substrates with and without barrier layer.

4.4 Conclusions

It is presented a new method for the removal of the thick barrier layer in NAA without removing the aluminium substrate based on a re-anodized step at a constant current density and chemical etchings. The best condition for removing the barrier layer is to fix a constant density current of 17.0 μA/cm^2 in the constant current re-anodization step, using as electrolyte a solution of H_3PO_4 (1% wt.) Previous methods for removing the barrier layer from NAA are designed for thin barrier layers and cannot apply in samples obtained in H_3PO_4 (1% wt.) electrolytes with barrier layers of more 200 nm. Our method was tested for NAA samples obtained by two-step anodization process and using an H_3PO_4 electrolyte and keeping a constant voltage of anodization of 195 V. In this kind of NAA, the thickness of the barrier layer is about 200 nm. Before dissolved the barrier layer, it is necessary to reduce the thickness of the barrier layer with H_3PO_4 (4% wt.). Now, under specific anodization at constant current density, the barrier layer can be dissolved. Several values of re-anodization current densities were tested to optimize the process of dissolution of the barrier layer. A re-anodization at a low current density such as 17.0 μA/cm^2 leads completely barrier layer-free NAA without detachment of the aluminium substrate. For higher re-anodization current densities, the measured anodization voltage shows an initial decrease followed by a steady increase. This indicates that the pore growth process continues by adjusting the barrier layer thickness to a new equilibrium state. In contrast, for re-anodization current densities below 17.0 μA/cm^2, measured anodization voltage shows a steady decrease and stabilization at a value close to 0 V. This behaviour is related to the creation of non-homogenous branchings within the barrier layer. This barrier layer with the branchings can be removed with a final chemical etching step of H_3PO_4 (4% wt.) at 35 °C. If the re-anodization step is carried out for a long time, the branchings continue to grow into the aluminium substrate creating a highly nanoporous layer between the original NAA and the aluminium substrate. If the final chemical etching step is applied to such a layer, NAA separates from the aluminium substrate. To avoid such detachment, it is crucial to stop the re-anodization before such highly nanoporous layer is formed. However, this process can be useful in the fabrication of nanoporous membranes.

Finally, the formation of barrier layer-free NAA allows for the infiltration of the nanopores and the establishment of electric contact between the resulting material the nanopores are filled in with and the aluminium substrate. Although this method has been developed for NAA obtained with H_3PO_4 electrolytes, it could be extended to NAA fabricated with different electrolytes at high voltage anodization. Further research to study the infiltration of different materials into the barrier-free NAA and the study their electrical characteristics is underway.

Chapter 5

Strategies for Infiltrating Solutions in Barrier Layer Free Nanoporous Anodic Alumina

In the following chapter, a novel type of perovskite solar cell device on a metallic substrate, using nanoporous anodic alumina as enclosure, is presented. The experimental methods used for infiltrating distinct kinds of materials within the nanoporous anodic alumina membrane, which barrier layer was previously removed, are explained. A nanostructured perovskite solar cell device is manufactured, and its current density-voltage characteristics are measured.

5.1 Introduction

Perovskite solar cells (PSCs), as is explained in chapter 2 section 2.2.2.2, have received a great deal of attention owing to their photovoltaic (PV) properties and because in a few years, its power conversion efficiencies (PCE) have experimented a high improvement. However, one of the disadvantages of the PSCs is the very poor stability of the perovskite layer in the presence of humidity, radiation and temperature.[217,248] Due to that, in this chapter, the fabrication of a nanostructured PSC based on nanoporous anodic alumina (NAA) technology is investigated. NAA provides the advantage of enhancing perovskite stability since the perovskite layer will be surrounded by the other layers and the nanopore walls.

To reach this aim, several challenges should be overcome: 1) Obtain an electrical contact between the aluminium and the first infiltrated material. 2) Achieve that the first infiltrated material diffuses until the nanopores bottom. 3) The different layers which compound the PSCs should have a specific thickness to work correctly, so each layer infiltrated must have the right height. 4) The infiltrated materials should fill the nanopores up to a certain height. It is also very important that the height of each material should be homogeneous among all the nanopores. 5) Finally, it is also crucial to find a semi-transparent electrode which does not damage the perovskite layer and deposited it on top of the solar cell structure.

In this chapter, a novel type of PSC device on a metallic substrate is presented. In our design, barrier layer-free NAA (wBL-NAA) is used as an enclosure and the aluminium of the wBL-NAA substrate will work as the opaque metal electrode. We expected that NAA to have the role of enclosure, in which monocrystals will grow, as a result of confinement. First, typical aluminium anodization using phosphoric acid was carried out to obtain the pattern for an ordered nanoporous substrate.[246] (chapter 3, section 3.1.2) Secondly, a procedure in which a partially widened nanoporous layer is subjected fixed-current anodization to remove the barrier layer was conducted.[249] (chapter 4) Finally, different layers corresponding to the structure of the PSC devices testes in chapter 3 section 3.2, for preparing the most used PSC device were infiltrated into the nanopores of NAA to obtain a nanostructured perovskite solar cell (nPSC) device.

5.2 Experimental

5.2.1 Titanium Dioxide Infiltration

To achieve the aim of having a nanostructured titanium dioxide (TiO_2) layer thickness below 100 nm and with a homogeneous height among all the nanopores, different tests were carried out.

First, a titanium dioxide (TiO_x) solution was prepared, in a N_2-filled glovebox, *via* the sol-gel method described by Kim *et al*.[215,250] mixing 0.2 mL of titanium (IV) isopropoxide ($Ti[OCH(CH_3)_2]_4$) with 0.1 mL of 2-methoxyethanol ($CH_3OCH_2CH_2OH$) and 1 mL of ethanolamine ($H_2NCH_2CH_2OH$). The TiO_x-solution was heated to 120 °C for 90 min under magnetic stirring to obtain a clear solution. Subsequently, the TiO_x-solution was filtered (0.2 µm PTFE filter) and diluted in anhydrous methanol (CH_3OH) with a volume ratio of 1:3 (TiO_x-solution:CH_3OH). The diluted TiO_x-solution was stirred for 1 h and filtered (0.2 µm PTFE filter) before its deposition.

Secondly, the diluted-TiOx solution was deposited on the top of different wBL-NAA substrates, prepared in the same conditions, *via* drop-casting and spin-coating.

Finally, after each deposition, to convert the precursors in TiO_2 by hydrolysis, the substrates were left in ambient conditions for 1 hour, heated at 150 °C for 10 min and heated at 500 °C for 30 min. The final temperature was reached by increasing the temperature with 20 °C/min heating rate. Since aluminium is the base of the wBL-NAA substrates, is very important to note that the aluminium melting point is 660 °C. The temperature at which the substrates must be heated for the TiO_2 anatase crystalline formation (500 °C) is very close to the aluminium melting point. This can cause the metallic aluminium substrate softening and can cause stress due to the difference in coefficients of thermal expansion between metallic aluminium and the porous aluminium oxide layer. Such stress can cause bending of the substrate. Therefore, once the TiO_2 formation temperature is reached, the substrates are quickly cooled by placing them on a base of material that is a good conductor of heat.

5.2.1.1 Titanium Dioxide Infiltration *via* Drop-Casting Deposition

Several diluted TiO_x-solution volumes (V_d) V_{d1} = 100 µL, V_{d2} = 50 µL, V_{d3} = 30 µL and V_{d4} = 20 µL were drop-casted on the top of four wBL-NAA substrates. The wBL-NAA substrate area exposed to V_d was 1.76 cm^2.

Substrate	1	2	3	4
Vd [µL]	100	50	30	20

Table 5.1. TiOx-solution volumes deposited on the top of wBL-NAA substrates via drop-casting.

5.2.1.2 Titanium Dioxide Infiltration *via* Spin-Coating Deposition

Various wBL-NAA substrates were placed in a spin-coating device. 100 µL of the diluted TiO_x-solution were deposited on the top of the wBL-NAA substrates. After waiting for 30 s to let the diluted TiO_x-solution infiltrates nanopores, the wBL-NAA substrates were spin-coated at 4000 rpm (2160 rpm/s) for 90 s, to obtain the desired nanostructured TiO_2 layer thickness below 100 nm.

5.2.2 $MAPbI_3$ perovskite Infiltration

To reach the goal of having a nanostructured methylammonium lead iodide ($MAPbI_3$) perovskite layer thickness between 400 nm and 600 nm and with a homogeneous height among all the nanopores, diverse experiments were conducted.

First, several $MAPbI_3$ perovskite precursor solutions were prepared, in an N_2-filled glovebox, from the two precursors as is explained in chapter 3 section 3.2.2.3. Subsequently, the solutions were filtered (0.2 µm PTFE filter) before its deposition.

Secondly, a wBL-NAA substrate was placed in a spin-coating device which was positioned in a N_2-filled glovebox. 100 µL of each $MAPbI_3$ perovskite precursor solution were dropped on the top of different wBL-NAA substrates prepared in identical conditions. After waiting for 60 s to let the solutions infiltrates nanopores, the substrates were spin-coated at 4000 rpm (3996 rpm/s) for 45 s, to obtain the desired nanostructured $MAPbI_3$ perovskite layer thickness between 400 nm and 600 nm.

Finally, the substrates were placed in a hotplate and they were annealed at 100 °C for 1 h to obtain crystalline perovskite ($MAPbI_3$) films. The conditions of the $MAPbI_3$ perovskite precursor solutions depositions are summarized in **table 5.2**.

Sub	$MAPbI_3$ [M]	Solvent	Ss [rpm]	Ac [rpm/s]	Time [s]
5	1.5	DMF	4000	3996	45
6	2	DMF	4000	3996	45
7	2.5	DMF	4000	3996	45

Table 5.2. Conditions of the $MAPbI_3$ perovskite precursor solutions depositions. Sub: substrate, Ss: spin speed, Ac: spin acceleration.

5.2.3 Spiro-OMeTAD Infiltration

To realise the target of having a 2,2',7,7'-Tetrakis[N,N-di(4-methoxyphenyl)amino]-9,9'-spirobifluorene (spiro-OMeTAD) layer with a homogeneous height among all the nanopores and to provide additional properties to its hole conduction, such as a complete levelling of NAA pores openings, distinct tests were performed.

Diverse solutions were prepared, in an N_2-filled glovebox, by dissolving different amounts of spiro-OMeTAD in 1 mL of anhydrous chlorobenzene. Subsequently, the solutions were vigorously stirred and filtered (0.2 µm PTFE filter) before its deposition. 100 µL of each solution were deposited on the top of several wBL-NAA-TiO_2-$MAPbI_3$ substrates prepared in identical conditions *via* spin-coating. The spiro-OMeTAD layer thickness was adjusted *via* concentration solution and spin-coating speed.

First, a 72 mg/mL spiro-OMeTAD solution was spin-coated at two different spin speeds (Ss): Ss_1 = 1000 rpm and Ss_2 = 1500 rpm. After these tests, the spiro-OMeTAD layer infiltration was optimized by testing two more spiro-OMeTAD solution concentrations (C): C_1 = 105 mg/mL and C_2 = 140 mg/mL, using the same spinning conditions in its deposition. The conditions of the spiro-OMeTAD solutions depositions are summarized in **table 5.3**.

Sub	Spiro-OMeTAD [mg/mL]	Ss [rpm]	Ac [rpm/s]	Time [s]
8	72	1000	1080	90
9	72	1500	1080	90
10	105	1000	1080	90
11	140	1000	1080	90

Table 5.3. Conditions of the spiro-OMeTAD solutions deposition. Sub: substrate, Ss: spin speed, Ac: spin acceleration.

To perform the first test, a 72 mg/mL spiro-OMeTAD solution was made by dissolving 72 mg of spiro-OMeTAD in 1 mL of anhydrous chlorobenzene. 100 µL of the 72 mg/mL spiro-OMeTAD solution were dropped on the top of two wBL-NAA-TiO_2-$MAPbI_3$ substrates and they were spin-coated at two different spin-coating speeds: Ss_1 = 1500 rpm (1080 rpm/s) and Ss_2 = 1000 rpm (1080 rpm/s) for 90 s. Afterwards, both substrates were placed into a thermal evaporation chamber (vacuum pressure < $5x5^{-6}$ torr, in an N_2-filled glovebox) and the semi-transparent electrode described by Jun Hee Han *et al.*[175] was deposited over the spiro-OMeTAD layer using a thin-film mask to pattern the electrode. It was composed by tungsten trioxide (WO_3) and silver (Ag). The structure consists of two thin Ag films surrounded by WO_3 layers. The semi-transparent electrode was deposited sequentially: WO_3 (50 nm)/Ag (12 nm)/WO_3 (105 nm)/Ag (12 nm)/WO_3 (50 nm).

Secondly, two more spiro-OMeTAD solutions were prepared with concentrations (C) greater than 72 mg/mL, C_3 = 105 mg/mL and C_4 = 140 mg/mL, by dissolving 105 mg and 140 mg of spiro-OMeTAD in 1 mL of anhydrous chlorobenzene. 100 µL of each spiro-OMeTAD solution were dropped on the top of two wBL-NAA-TiO_2-$MAPbI_3$ substrates and they were spin-coated at 1000 rpm (1080 rpm/s) for 90 s.

5.2.4 Nanostructured Perovskite Solar Cell Device Fabrication

To fabricate a nanostructured perovskite solar cell (nPSC) device several wBL-NAA substrates, prepared under identical conditions, with a nanoporous film thickness of about 1 µm, were placed in a spin-coating device which is positioned in an N_2-filled glovebox. Some of the previously prepared solutions were filtered (0.2 µm PTFE filter) before its deposition and they were deposited under nitrogen conditions (O_2 < 0.1 ppm and H_20 < 0.1 ppm). The conditions of each solution deposition are summarized in **table 5.3**.

Material	C [M]	Vd [µL]	Ss [rpm]	Ac [rpm/s]	T [s]
TiOx		100	4000	2160	90
$MAPbI_3$	2	100	4000	3996	45
s-OMeTAD	0.114	100	1000	1080	90

Table 5.4. Conditions of the solutions depositions. C: concentration, Vd: deposited volume, Ss: spin speed, Ac: spin acceleration, T: spin time.

First, 100 µL of the diluted TiO_x-solution were dropped on the top of the wBL-NAA substrates. After waiting for 30 s to let the diluted TiO_x-solution infiltrates nanopores, the wBL-NAA substrates were spin-coated at 4000 rpm (2160 rpm/s) for 90 s. Then, to convert the precursors in TiO_2 by hydrolysis, the substrates were left in ambient conditions for 1 hour, heated at 150 °C for 10 min and heated at 500 °C for 30 min.

Secondly, 100 µL of the 2 M $MAPbI_3$ perovskite precursor solution were dropped on the top the previously deposited layer. Following, after waiting for 60 s to let the solution infiltration, the substrates were spin-coated at 4000 rpm (3996 rpm/s) for 45 s. Subsequently, the substrates were placed in a hotplate and they were annealed at 100 °C for 1 h. The surface of the substrates turned black during the first minute of the annealing process.

Thirdly, 100 µL of the 140 mg/mL spiro-OMeTAD solution were dropped on the top of the previously deposited layer and the substrates were spin-coated at 1000 rpm (1080 rpm/s) for 90 s.

Finally, the substrates were loaded into the thermal evaporation chamber (vacuum pressure < $5x10^{-6}$ torr, in an N_2-filled glovebox) and using a thin-film mask the semi-transparent electrode was thermally deposited sequentially: WO_3 (50 nm)/Ag (12 nm)/WO_3 (105 nm)/Ag (12 nm)/WO_3 (50 nm). Afterwards, the thin-film mask was changed and 150 nm of Ag were thermally deposited. In all cases, the effective device area of the nPSC was 0.28 cm^2.

Figure 5.1 a) shows a schematic diagram and **b)** displays a photo of the prepared nPSC device.

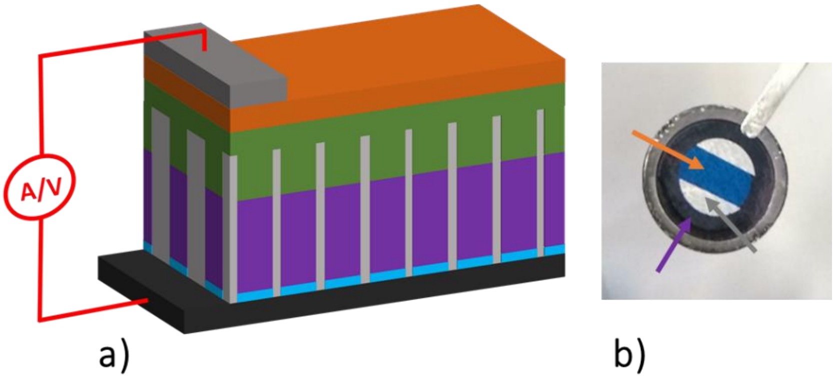

Figure 5.1. a) nPSC basic architecture scheme. **b)** nPCS device photo. Layers are not to scale in the basic architecture scheme.

5.2.5 Semi-Transparent Electrode Characterization

To measure the transmittance and sheet resistance of the proposed semi-transparent electrode composed of WO_3 (50 nm)/Ag (12 nm)/WO_3 (105 nm)/Ag (12 nm)/WO_3, several glasses were placed in the thermal evaporation chamber (vacuum pressure < $5x10^{-6}$ torr, in an N_2-filled glovebox and the alternative layers of WO_3 and Ag were evaporated under the same conditions.

5.3 Results and Discussion

5.3.1 Titanium Dioxide Infiltration

5.3.1.1 Titanium Dioxide Infiltration *via* Drop-Casting Deposition

To measure the nanostructured TiO_2 layer thickness within the nanopores an SEM study of the wBL-NAA-TiO_2 substrate was carried out. **Figures 5.2 a)**, **b)**, **c)** and **d)** show the top SEM pictures of the wBL-NAA substrates after the TiO_x diluted-solution deposition *via* drop-casting. The volumes deposited were 100 µL, 50 µL, 30 µL and 20 µL, respectively. For V_{d1} = 100 µL [**figure 5.2 a)**] the nanopore structure of the wBL-NAA surface can be observed without any traces of deposited TiO_2 on top of them. For V_{d2} = 50 µL, V_{d3} = 30 µL and V_{d4} = 20 µL [**figures 5.2 b)**, **c)** and **d)**, respectively] big TiO_2 islands with characteristic sizes between 5 and 10 µm can be observed on top of the wBL-NAA nanopore structure, marked by the blue arrows. Among the TiO_2 islands, nanopores pathways can be seen. These pathways become more narrows as the amount of deposited TiO_2 decreases.

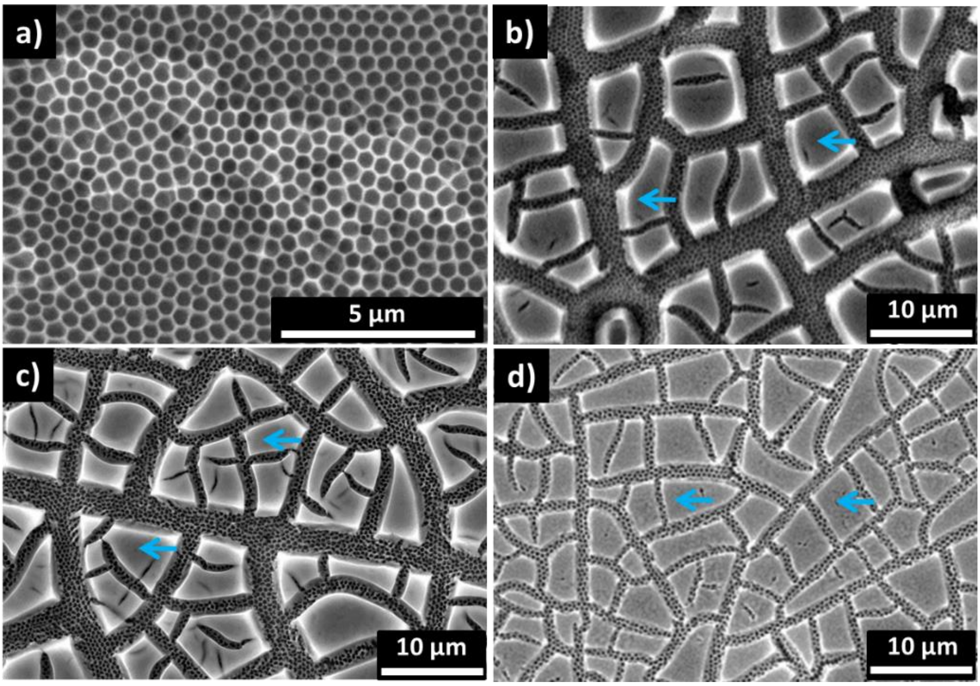

Figure 5.2. a), **b)**, **c)** and **d)** top SEM views of the wBL-NAA substrates after the TiO_x diluted-solution deposition *via* drop-casting. The volumes deposited were 100 µL, 50 µL, 30 µL and 20 µL, respectively. The scale bars are indicated in each picture and the TiO_2 is marked by blue arrows.

Figure 5.2 demonstrates a clear tendency of the TiO_2 precursor solution to infiltrate better into the nanopores for bigger deposited volumes. This is probably due to the speed at which the solvent used in the dilution it evaporates since methanol anhydrous is very volatile. When the solution is dropped, it starts to fill the nanopores, but at the same time, it evaporates very fast. If the volume of deposited TiO_2 precursor solution is not big enough, it will not have time to infiltrate the nanopores, therefore, TiO_2 instead of infiltrating the nanopores is covering them. If the droplet volume is smaller, evaporation will take a smaller time, and consequently, the solution has not enough time to infiltrate the nanopores. For V_{d1} = 100 µL [**figure 5.2 a)**] TiO_2

has infiltrated the nanopores without filling them. For V_{d4} = 20 µL [**figure 5.2 d)**] there are more TiO_2 covering the nanopores than for V_{d3} = 30 µL and V_{d2} = 50 µL [**figure 5.2 c)** and **b)**, respectively] and in turn in for V_{d3} = 30 µL [**figure 5.2 c)**] there are more TiO_2 covering the nanopores than V_{d2} = 50 µL [**figure 5.2 b)**]. There is a great amount of TiO_2 covering the nanopores, therefore, the TiO_2 is not within the nanopores.

5.3.1.2 Titanium Dioxide Infiltration *via* Spin-Coating Deposition

To estimate the nanostructured TiO_2 layer thickness within the nanopores a cross-sectional SEM study of the wBL-NAA-TiO_2 substrate was conducted. **Figure 5.3** exhibits the cross-section SEM picture of the wBL-NAA substrate after the diluted TiOx-solution infiltration *via* spin-coating deposition. The double blue arrow is pointing the TiO_2 amount on the nanopores bottom. The simple blue arrows are marking the actual TiO_2 thickness. The double purple arrow denotes the $MAPbI_3$ perovskite layer, which was deposited after the diluted TiO_x-solution, now we focus on the TiO_2 layer. **Figure 5.3** shows as the TiO_2 layer is homogeneously distributed on the nanopores bottom covering the aluminium surface. The nanostructured TiO_2 layer thickness was estimated at 40 nm.

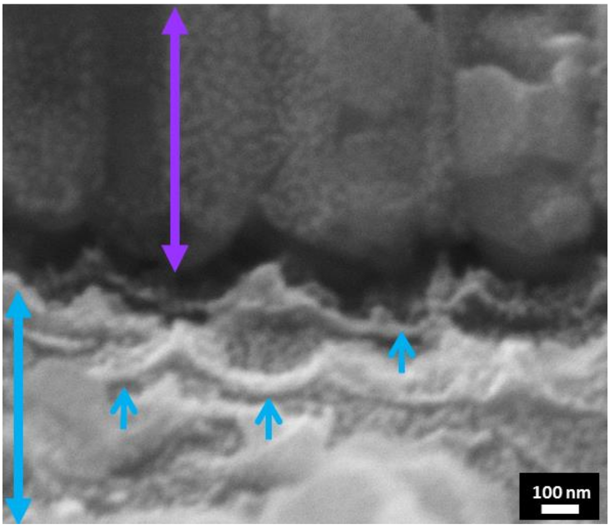

Figure 5.3. Cross-section SEM view of the wBL-NAA substrate after the diluted TiOx-solution infiltration via spin-coating deposition. The scale is indicated in the picture and the TiO_2 is marked by the blue arrows.

5.3.2 $MAPbI_3$ perovskite infiltration

To estimate the nanostructured $MAPbI_3$ layer thickness within the nanopores a cross-sectional SEM study of the wBL-NAA-$MAPbI_3$ substrates was performed. **Figures 5.4**, **5.5** and **5.5 a)** and **b)** display the top and **c)** and **d)** exhibit the cross-section SEM pictures of the wBL-NAA substrates after the $MAPbI_3$ perovskite precursor solutions infiltrations with a concentration of 1.5 M, 2 M and 2.5 M, respectively.

From **figure 5.4 a)** nanopores with different colours can be distinguished, some are black and others are white. The nanoporous layer thickness is about 1 µm. The differences in the colour observed in the SEM pictures is given by the different filling degree of the nanopores. If the nanopores are partially filled (it is means less than 500 nm) they will be black. If the nanopores are almost filled (it means more than 500 nm and less than 1 µm) they will be white. In **figure 5.4 b)** a grey layer of about 7 µm over the nanopores can be observed (marked by the purple arrow). It is a $MAPbI_3$ layer. In **figure 5.4 c)** and **d)** the double purple arrows are marking the $MAPbI_3$ thickness and the yellow one denotes the nanopores thickness. From these pictures, the nanostructured $MAPbI_3$ layer thickness was estimated at 700 nm.

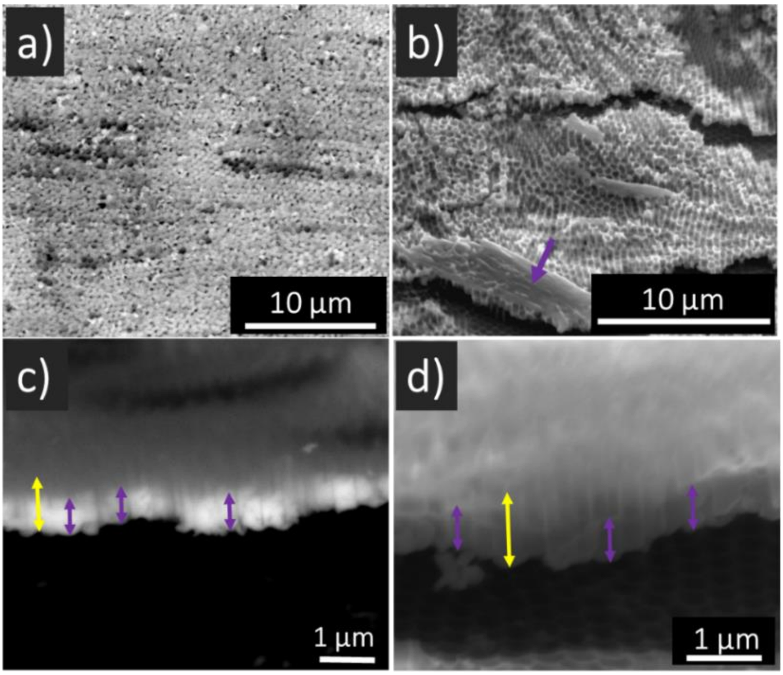

Figure 5.4. **a)** and **b)** top; **c)** and **d)** cross-section SEM views of the wBL-NAA substrate after the $MAPbI_3$ (1.5 M) infiltration via spin-coating deposition. The $MAPbI_3$ layer is marked by purple. The yellow double arrow denotes the nanopores thickness. Pictures **a)** and **c)** were taken in backscattering mode. The scale bars are indicated in each picture.

In **figures 5.5 a)** and **b)** nanopores with a uniform grey tone across the surface can be observed. It is because the filling degree is homogeneous through the nanoporous layer. Following the same reasoning from **figure 5.4 a)** the nanopores are partially filled. In **figure 5.5 d)** the double purple arrows are marking the $MAPbI_3$ thickness and the yellow one denotes the nanopores thickness. From these pictures, the nanostructured $MAPbI_3$ layer thickness was estimated at 500 nm.

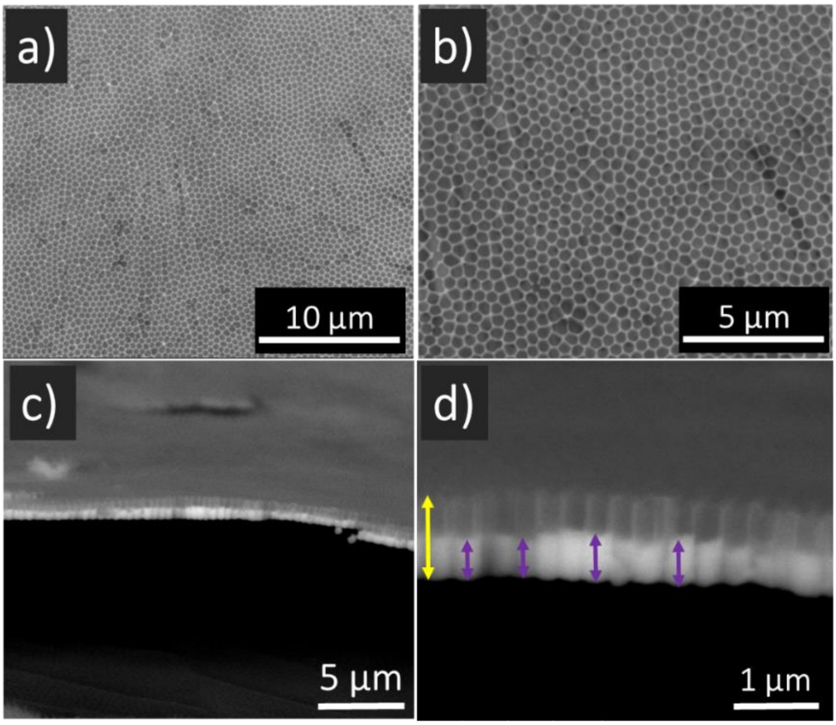

Figure 5.5. a) and **b)** top; **c)** and **d)** cross-section SEM views of the wBL-NAA substrate after the $MAPbI_3$ (2 M) infiltration via spin-coating deposition. The $MAPbI_3$ layer is marked by purple. The yellow double arrow denotes the nanopores thickness. Pictures **c)** and **d)** were taken in backscattering mode. The scales are indicated in each picture.

In **figures 5.6 a)** and **b)** a kind of needles can be seen, marked by purples arrows. These needles are the $MAPbI_3$ crystals, which grows over NAA surface instead of growing inside the nanopores as it is expected. In **figures 5.6 c)** and **d)** the double purple arrows are marking the $MAPbI_3$ thickness and the yellow one denotes the nanopores thickness. From these pictures, the nanostructured $MAPbI_3$ layer thickness was estimated at 1000 nm.

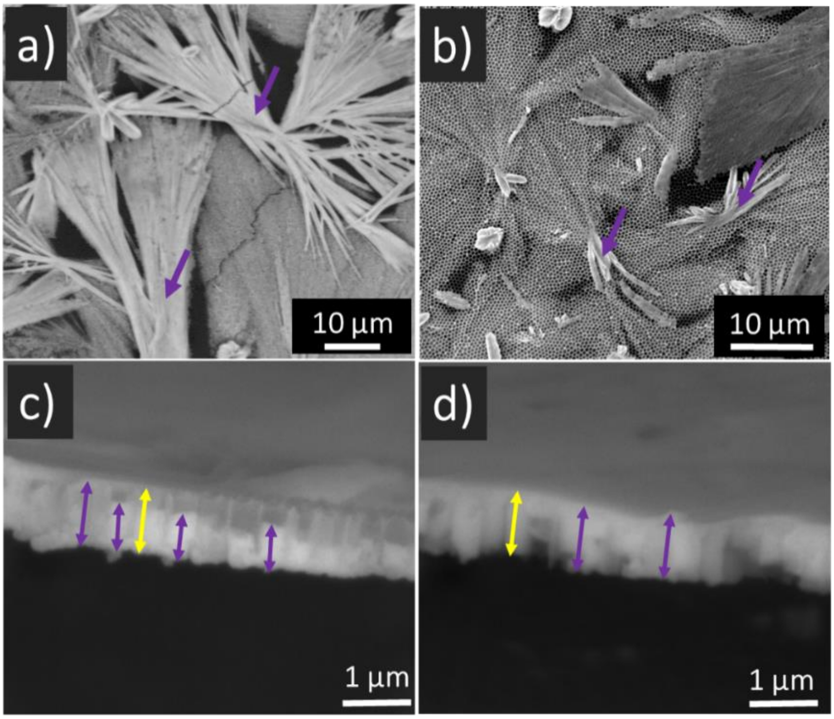

Figure 5.6. a) and **b)** top; **c)** and **d)** cross-section SEM views of the wBL-NAA substrate after the $MAPbI_3$ (2.5 M) infiltration via spin-coating deposition. The $MAPbI_3$ layer is marked by purple. The yellow double arrow denotes the nanopores thickness. Pictures **a)**, **c)** and **d)** were taken in backscattering mode. The scales are indicated in each picture.

Figure 5.7 a) shows the X-Ray diffractograms for $MAPbI_3$ perovskite precursor solution deposited over an electropolished aluminium (black line) and wBL-NAA substrates (purple line). **Figure 5.7 b)** displays the XRD of $MAPbI_3$ perovskite magnified in the region of (2θ = 10.0°–16.0°) and (2θ = 26.0°–30.0°). In **figure 5.7 a)** several diffraction peaks can be observed. In agreement with reported literature, the peaks at 14.0°, 20.0°, 23.5°, 24.5°, 28.2°, 31.7°, 35.0°, 40.5° and 43° in the XRD pattern corresponding to (110), (200), (211), (202), (220), (310), (312), (224) and (330) diffraction planes of $MAPbI_3$ perovskite, respectively.[251,252] Those diffraction peaks are assigned to the crystal planes of the tetragonal lattice of the mixed halide perovskite, indicating that the tetragonal $MAPbI_3$ perovskite structure is formed.[253] In **figure 5.7 b)** two strongest intensities centred about 14.0° and 28.0° can be seen, corresponding to the more characteristic peaks of the tetragonal $MAPbI_3$ perovskite structure. Also, there are two more diffraction peaks at 38.5° and 44.8°, corresponding to pure aluminium, due to the aluminium is the base of the electropolished and wBL-NAA substrates.

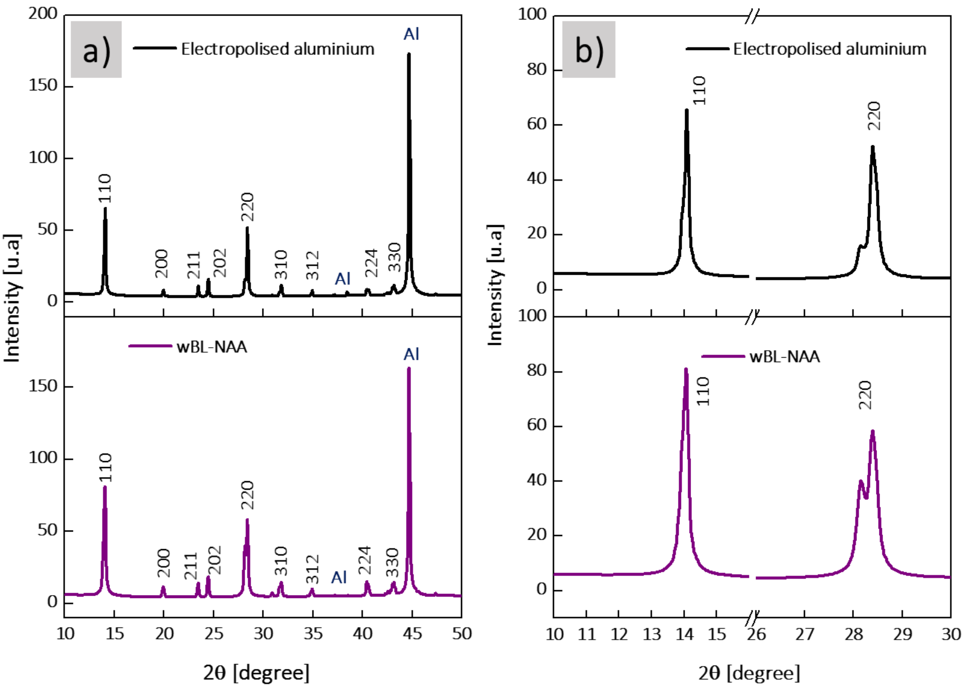

Figure 5.7. **a)** Measured X-ray diffraction patterns of MAPbI$_3$ perovskite deposited over an electropolised aluminium (black line) and wBL-NAA (purple line) substrates. **b)** magnified in the region of (2θ = 10.0°–16.0°) and (2θ = 26.0°–30.0°).

5.3.3 Spiro-OMeTAD Infiltration

To calculate the spiro-OMeTAD height and check if it has infiltrated the nanopores filling them and levelling the rough NAA surface an SEM study of the wBL-NAA-MAPbI$_3$-spiroOMeTAD substrate was carried out. **Figures 5.8 a)** and **b)** exhibit the cross-section and **figures 5.8 c)** and **d)** show the top SEM pictures of wBL-NAA-MAPbI$_3$ substrate after the 72 mg/mL spiro-OMeTAD solution deposition, at the spin-coating speeds of 1500 rpm and 1000 rpm, respectively. **Figures 5.8 e)** and **f)** correspond to the same substrates as **figures 5.8 e)** and **f)** at a higher magnification.

In **figures 5.8 a)** and **b)** three layers can be distinguished, the $MAPbI_3$ layer marked by a purple double arrow, the spiro-OMeTAD layer marked by a green double arrow and the semi-transparent electrode marked by an orange double arrow. The yellow double arrow denotes the nanopore thickness. From Ss_1 = 1500 rpm [**figure 5.8 a)**] and Ss_2 = 1000 rpm **[figure 5.8 b)]** the total thickness of the different infiltrated layers is estimated at 862 nm and 924 nm, respectively. Both thicknesses are less than the nanopores thickness (1 µm), therefore, part of the semi-transparent electrode is infiltrated into the nanopores, and part of it covers NAA surface.

In **figure 5.8** it can be seen as the nanopores were not filled with the spiro-OMeTAD for any of the tested spinning speeds. The spiro-OMeTAD layer should fill the nanopores and form a flat film which covers NAA surface. Although for Ss_2 = 1000 rpm [**figure 5.8 b)**] the spiro-OMeTAD can fill the nanopores to a greater depth than for Ss_1 = 1500 rpm [**figure 5.8 a)**], the reached depth is not enough. The spiro-OMeTAD layer thicknesses were not enough to fill the nanopores and cover NAA surface, therefore a thicker spiro-OMeTAD layer is necessary. In **figures 5.8 c)** and **d)** and their magnifications **figures 5.8 e)** and **f)**, the semi-transparent electrode surface, marked by orange arrows, can be observed. This layer shows roughness on the semi-transparent electrode film.

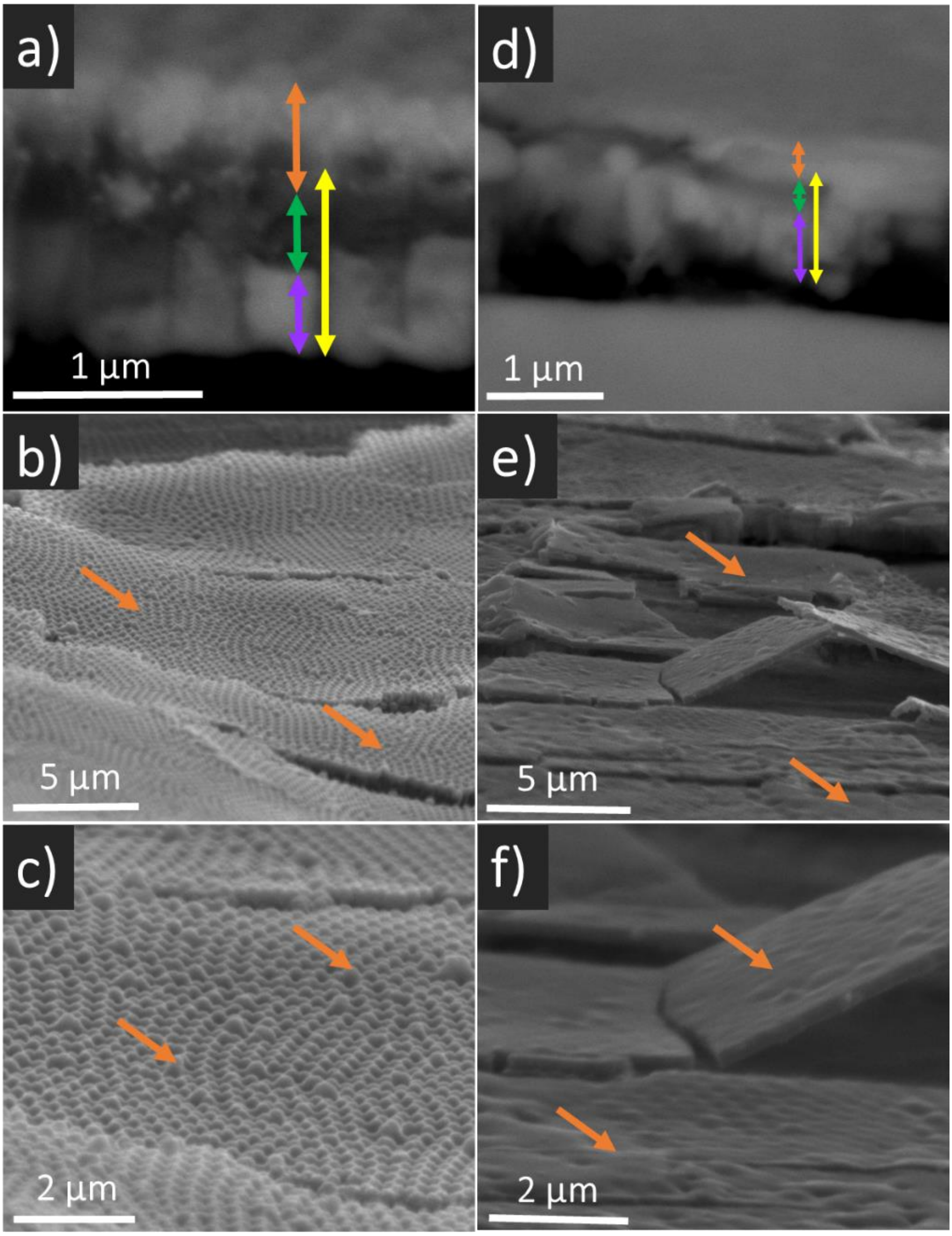

Figure 5.8. a) and **b)** cross-section; **c)** and **d)** top SEM views of wBL-NAA-$MAPbI_3$ after the spiro-OMeTAD deposition at the spin-coating speeds of 1500 rpm and 1000 rpm, respectively, and the posterior electrode thermal evaporation. The $MAPbI_3$, spiro-OMeTAD and the semi-transparent electrode layers are marked by purple, green and orange arrows, respectively. The yellow double arrow denotes the nanopores thickness. Pictures **a)** and **b)** were taken in backscattering mode. The scales are indicated in each picture.

Figures 5.9 a) and **b)** show the cross-section and **figures 5.9 c)** and **d)** show the top SEM pictures of the wBL-NAA-$MAPbI_3$ substrates after 105 mg/mL and 140 mg/mL spiro-OMeTAD solutions infiltration, respectively. **Figures 5.9 e)** and **f)** display the magnification pictures of **c)** and **d)**, respectively. In **figures 5.9 a)** and **b)** two layers can be distinguished, a $MAPbI_3$ layer marked by a double purple arrow and the spiro-OMeTAD layer marked by a double green arrow. The yellow double arrow denotes the nanopores thickness (1 µm). For C_1 = 105 mg/mL [**figure 5.9 a)**] and C_2 = 140 mg/mL [**figure 5.9 b)**] the total thickness of the different infiltrated layers is estimated at 1.03 µm and 1.45 µm, respectively. In **figures 5.9 c)** and **d)** and their magnifications, **figures 5.9 e)** and **f)**, the spiro-OMeTAD film surface can be observed. **Figures 5.9 c)** and **e)** show roughness on the spiro-OMeTAD film. On the other hand, **figures 5.9 d)** and **f)** exhibit a flat spiro-OMeTAD film.

In **figure 5.9** it can be seen as the nanopores were filled for both deposited spin speeds, however, in **figure 5.9 a)** the spiro-OMeTAD only is filling the nanopores while in **figure 5.9 b)** the spiro-OMeTAD is not only filling the nanopores but also is covering them and forming a flat film over the wBL-NAA surface. The nanopores structure of the wBL-NAA surface cannot be observed on the top-view picture. This indicates that spiro-OMeTAD has infiltrated the nanopores filling them and also it is levelling the rough NAA surface. The overall thickness of the layer resulted to be somehow higher than optimum (~900 nm *vs* 100-300 nm) and could incur resistive losses.

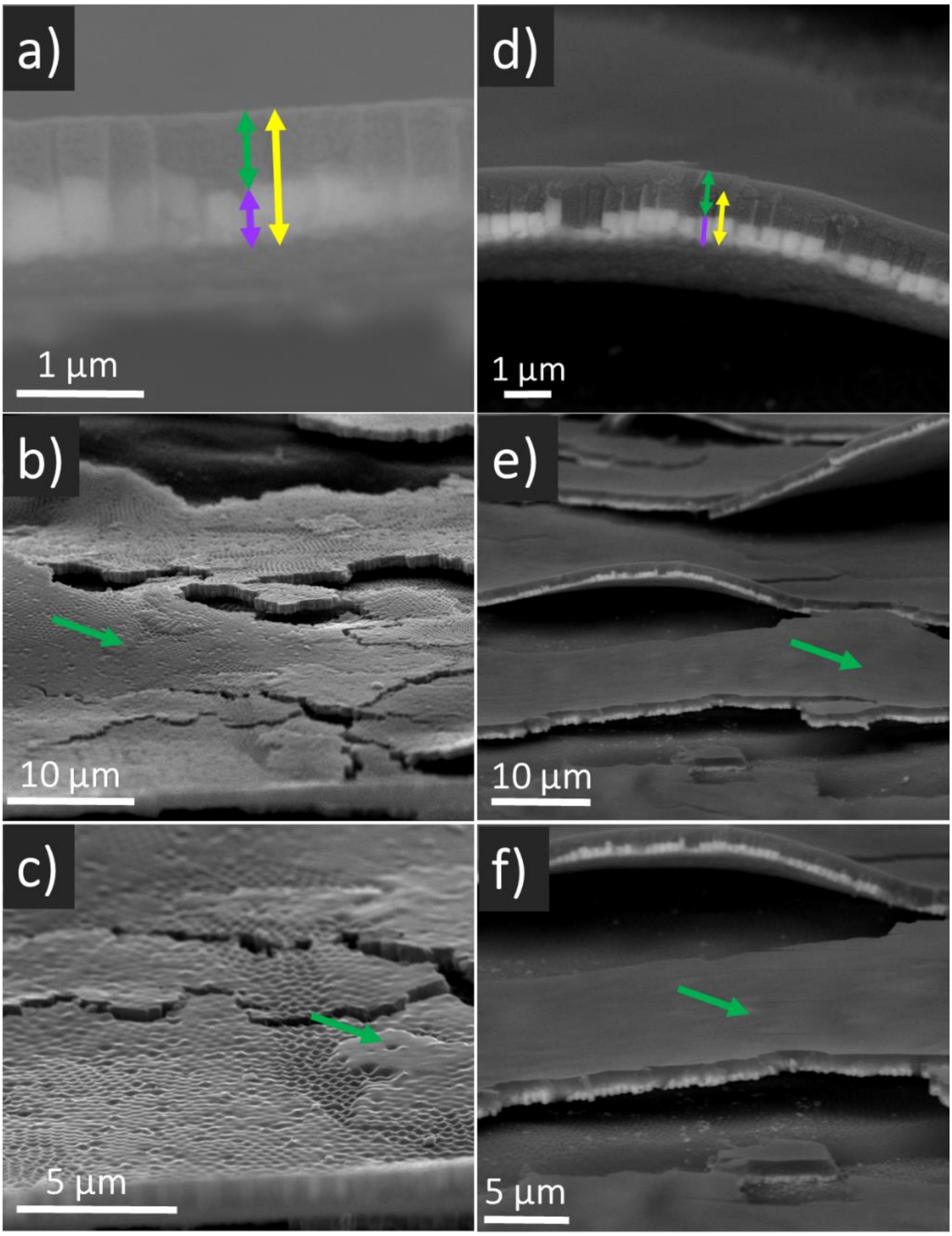

Figure 5.9. **a)** and **b)** top and **c)** and **d)** cross-section SEM views of wBL-NAA-$MAPbI_3$ after 105 mg/mL and 140 mg/mL spiro-OMeTAD solutions deposition, respectively. **e)** and **f)** magnifications views of **c)** and **d)** respectively. The $MAPbI_3$ and spiro-OMeTAD layers are marked by purple and green arrows, respectively. The yellow double arrow denotes the nanopore thickness. Pictures **a)**, **c)**, **e)** and **f)** were taken in backscattering mode. The scales are indicated in each picture.

5.3.4 Nanostructured perovskite solar cell device

To measure the height of each infiltrated material and check if their height is homogeneous through the wBL-NAA substrate a SEM study of the nPSC device was conducted. **Figure 5.10** presents the cross-section SEM picture of one of the obtained nPSC devices, in which each material is highlighted with a different colour as is indicated in the picture. From **figure 5.10** the thicknesses of the TiO_2, $MAPbI_3$, spiro-OMeTAD and semi-transparent electrode are estimated at 40 nm, 500 nm, 900 nm and 230 nm, respectively.

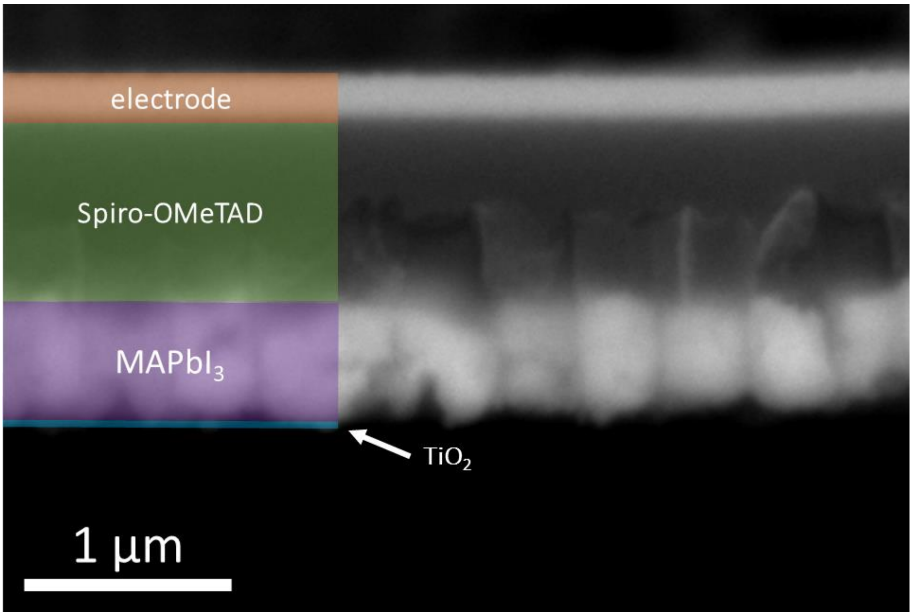

Figure 5.10. Cross-section SEM view of the nPCS device highlighting each material. The picture was taken in backscattering mode.

The Current density *vs* voltage (*JV*) characteristics of the best performing nPSCs devices measured in dark and under simulated AM1.5G illumination are shown in **figure 5.11**. The Primary performance parameters values of the devices are summaries in **table 5.5**, open-circuit voltage (V_{oc}), short-circuit current density (J_{sc}), fill factor (FF) and power conversion efficiency (PCE). Results demonstrate that a working nanostructured perovskite solar cell using barrier layer-free NAA as enclosure is obtained.

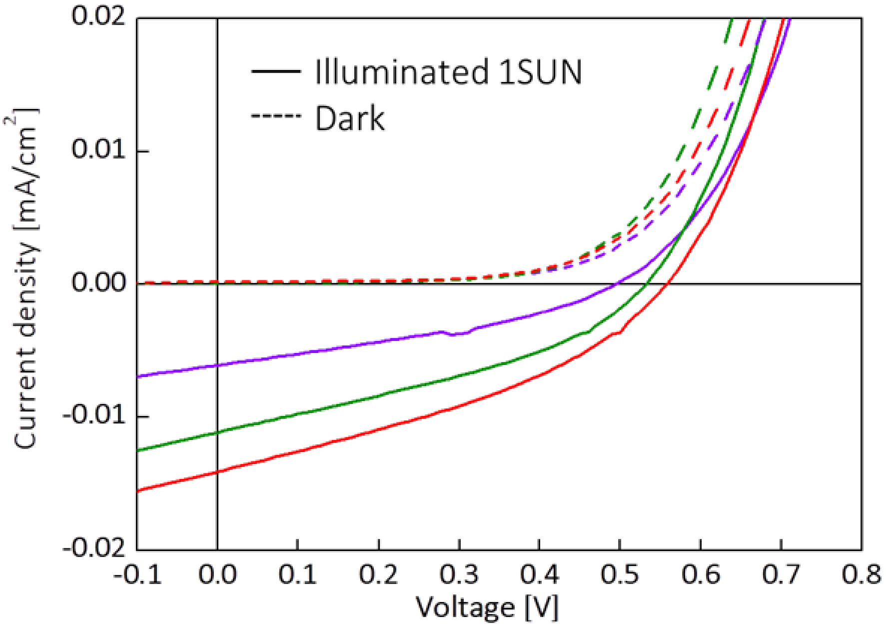

Figure 5.11. Current density *vs* voltage (*JV*) characteristics of the best performing nPSCs devices in dark (hollow markers) and under simulated A.M. 1.5G illumination (100 mWcm^{-2}).

	V_{oc} [V]	J_{sc} [mA/cm^2]	FF [%]	PCE [%]
Purple	0.49	0.006	38	0.01
Green	0.53	0.011	36	0.02
Red	0.56	0.014	36	0.03

Table 5.5. Primary performance parameters values of the best-performing nPCSs devices measured at 1 SUN A.M. 1.5 illumination (100 mWcm^{-2}). V_{oc}: open-circuit voltage, J_{sc}: short circuit current density, FF: fill factor and PCE: power conversion efficiency.

The effective active area of the devices was calculated with the area of the illuminated device (0.28 cm^2). However, alumina is an insulating material, it should be taken into account to calculate the theoretical effective active area of the devices. The porosity of alumina is about 10%[66]. So, the theoretical density current and efficiency values can be corrected in a 10 factor.

The low *J-V* characteristics are probably due to a combination of factors linked to the morphological complexity of the device. The extremely thick layer of HTM, necessary to level the barrier layer free NAA, is most probably responsible for significant losses. The high density of structural defects together with the great thickness of the overall device are likely responsible for a great amount of charge trapping as well as fast rates of recombination dynamics with respect to charge percolation/sweep out to the respective electrodes.

5.3.5 Semi-Transparent Electrode Characterization

To check if the proposed semi-transparent electrode has good proprieties as electrode its optical and electric properties were assessed. The measured average transmittance (T_{avg}) and measured average sheet resistance (Rs_{avg}) values are 21% and 2.8 Ω/sq respectively. **Figure 5.12** shows the transmittance spectra of the proposed electrode and the reference glass substrate as a function of wavelength (300-800 nm).

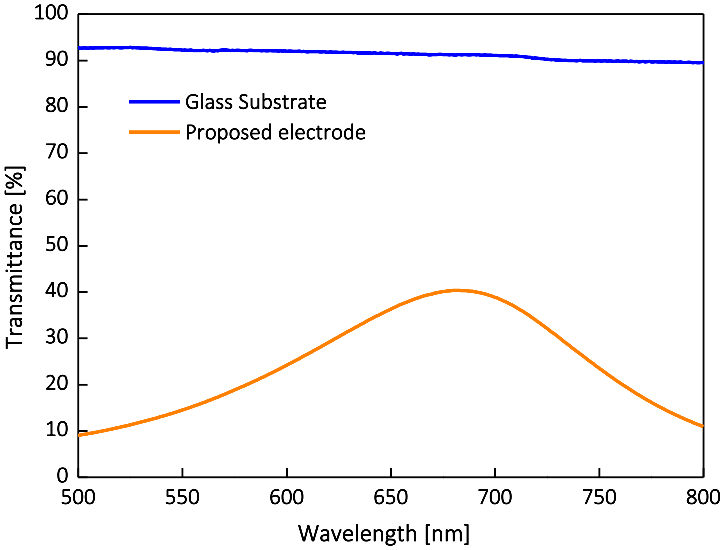

Figure 5.12. Optical transmittance spectra of the proposed semi-transparent electrode and the reference glass substrate.

The very low photovoltaic effect can be attributed to the strong absorbance of the anode. The UV-Visible characterisation of the alternating WO_3/Ag layers showed that the layer possesses a stronger absorbance than that expected from the literature. Further optimisation would be necessary in order to find a better trade-off between high conductivity and low absorbance.

5.4 Conclusions

In this chapter, the existing electrical contact between the aluminium and the first infiltrated material, since a nPSC with PV effect is achieved, is corroborated. So, the fact that aluminium can be used as electrical contact is demonstrated.

The infiltration of different materials, e.g., oxides (TiO_2), hybrid organic-inorganic ($MAPbI_3$), organics (spiro-OMeTAD), within the nanopores of wBL-

NAA (with a nanoporous film thickness of about 1 µm) *via* simple deposition methods such as spin-coating is demonstrated. Also, **figure 5.3** shows as TiO_2 diffuses until the nanopores bottom. Several tests to find the optimal nanostructured layer thickness of each layer were carried out. In the case of the spiro-OMeTAD layer, the main aim was to level the rough NAA surface. These tests consist of deposit a precursor solution or a solution of the material, with distinct concentrations, *via* spin-coating method under different deposition conditions, i.e., spin speed, spin acceleration and spin time. In this way, the height of the material infiltrates can be controlled by the spinning conditions and the material concentration, has been demonstrated. Besides, cross-section SEM pictures exhibit as the height of each material is homogeneous among all the nanopores. The best conditions to obtain the appropriate nanostructure layer thicknesses of each material are summarized in **table 5.6**

Finally, a semi-transparent electrode which does not damage the perovskite layer, based on WO_3 and Ag, is thermally deposited on top of the solar cell structure.

Material	C [M]	Vd [µL]	Ss [rpm]	Ac [rpm/s]	T [s]
TiOx		100	4000	2160	90
$MAPbI_3$	2	100	4000	3996	45
s-OMeTAD	0.114	100	1000	1080	90

Table 5.6. Best conditions of the solutions depositions to obtain the appropriate nanostructure layer thicknesses. C: concentration, Vd: deposited volume, Ss: spin speed, Ac: spin acceleration, T: spin time.

Results show that this methodology permits the preparation of fully working nanostructured perovskite solar cells using barrier layer-free NAA as enclosure. The devices displayed modest values of V_{OC}, J_{SC}, FF and power PCE with respect to state-of-the-art PSC devices, however, and most importantly, the shape of the *J*-*V* characteristics provide unequivocal confirmation that an ohmic contact is present between the aluminium substrate and the successive layers. Indeed, the rectifying behaviour demonstrates that electrons are injected into the aluminium cathode and that a built-in field is present under open circuit conditions. Therefore, it marks a starting point for making cells with nanoporous structures. Further research will be underway to improve the results. For example, it is needed to avoid the thermal treatment of TiO_x, decrease the height of the spiro-OMeTAD layer, use its dopants and increase the transmittance of the electrode semi-transparent. Also, different perovskites can be used.

Chapter 6

Improvement of Solutions Infiltration in Barrier Layer-Free NAA

In the following chapter, the optimization of the nanostructured perovskite solar cell device obtained in the preceding chapter is investigated. Several changes were introduced to achieve a solar cell with better current density-voltage characteristics. The experimental part of this chapter was carried out in the CIDEMAT group of the University of Antioquia from Medellin (Colombia)

6.1 Introduction

In the previous chapter, a fully working nanostructured perovskite solar cell (nPSC) based on nanoporous anodic alumina (NAA) was performed. For the first time, a photovoltaic effect in this kind of device was achieved. However, the results obtained were very modest. Therefore, this work aimed is to manufacture a nPSC with better results. To reach this aim several changes on the materials infiltrated were carried out.

1) As is explained in the preceding chapter, NAA substrates which barrier layer was previously removed and in which the TiO_x-solution is infiltrated (wBL-NAA-TiO_x) should be heated at 500 °C to obtain a TiO_2 anatase crystalline formation. To avoid this thermal treatment, which can damage NAA, in this chapter the TiO_x-solution was replaced by commercial nanoparticles of TiO_2 which already present an anatase crystalline form.

2) The perovskite employed ($MAPbI_3$) was substituted by a more stable perovskite: the caesium formamidinium methylammonium lead iodide bromide perovskite (CsFAMAPbIBr) with stoichiometry $(FAPbI_3)_{0.78}(MAPbBr_3)_{0.14}(CsPbI_3)_{0.08}$.

3) In the device manufactured in chapter 5, the spiro-OMeTAD layer was very thick, this can produce resistive losses, so one of the most important optimizations need is to reduce the thickness of this layer. Also, the bis(trifluoromethylsulfonyl)amine lithium salt solution and tert-butylpiridine (dopants more commonly used for optimizing the performance of the spiro-OMeTaD) were added.

4) Another important change is the semi-transparent electrode used. The transmittance of the WO_3 (50 nm)/Ag (12 nm)/WO_3 (105 nm)/Ag (12

nm)/WO_3 electrode was very low, therefore, several tests to optimizes the transmittance were carried out.

6.2 Experimental

6.2.1 Titanium Dioxide Infiltration

To reach the goal of having a nanostructured titanium dioxide (TiO_2) layer thickness below 100 nm and with a homogeneous height among all the nanopores, distinct tests were carried out. Several titanium dioxide nanoparticles (TiO_2-NPs) dispersions were prepared with different concentrations and employing diverse solvents. The solvents used for the TiO_2-NPs dispersions were a mixture of deionized water (H_2O) and ethanol (C_2H_5OH) at different volume fractions). Following, the effect of these variables (TiO_2-NPs concentration and solvent) in the TiO_2-NPs infiltration within the nanopores was studied.

Initially, six TiO_2-NPs dispersions were tested at three concentrations (C): C = 2 mg/mL, C = 5 mg/mL and C = 10 mg/mL and employing a mixture of H_2O:C_2H_5OH with a volume ratio of 1:1 and 1:3 as solvents. After these tests, the procedure was further optimized by testing four more TiO_2-NPs dispersions: C = 3 mg/mL, C = 1.5 mg/mL, C = 1 mg/mL and C = 0.5 mg/mL, employing a mixture of H_2O: C_2H_5OH with a volume ratio of 1:1. To carry out these tests 2 mg, 5 mg, 10 mg and then 3 mg, 1.5 mg, 1 mg and 0.5 mg of TiO_2-NPs were dispersed in 1 mL of the solvent and subsequently, they were vigorously stirred to achieve a good NPs dispersion.

The commercial TiO_2-NPs presented an anatase crystalline form. Therefore, a temperature treatment after each TiO_2-NPs dispersion deposition was not necessary. The TiO_2-NPs dispersions summarized in **table**

6.1 were prepared and 100 µL of each solution were drop-casted on the top of several wBL-NAA substrates elaborated under the same conditions.

Sub	TiO_2-NPs concentration [mg/mL]	Volume ratio [H_2O: C_2H_5OH]
1	2	1:1
2	2	1:3
3	5	1:1
4	5	1:3
5	10	1:1
6	10	1:3
7	3	1:1
8	1.5	1:1
9	1	1:1
10	0.5	1:1

Table 6.1. Conditions of the prepared titanium dioxide nanoparticles dispersions. Sub: substrate.

6.2.2 CsFAMAPbIBr Perovskite Infiltration

To achieve the aim of having a nanostructured caesium formamidinium methylammonium lead iodide bromide (CsFAMAPbIBr) perovskite layer thickness between 400 and 600 nm, and with a homogeneous height among all the nanopores, a 1 M CsFAMAPbIBr perovskite precursor solution was prepared, in a N_2-filled glove-box, as is explained on chapter 3 (3.2.3.3). The precursor solution was filtered before its deposition. The wBL-NAA-TiO_2 substrates, made under identical conditions, were loaded in a spin-coating which is positioned in a dry-box. 100 µL of CsFAMAPbIBr perovskite precursor solution were dropped on the top the substrates. After waiting for 60 s to let the CsFAMAPbIBr perovskite precursor solution infiltration in the nanopores, the substrates were spin-coated at 4000 rpm (3996 rpm/s) for 45 s, to obtain the desired nanostructured CsFAMAPbIBr perovskite layer thickness between 400 nm and 600 nm. Later, the substrates were placed in a hotplate and they were annealed at 100 °C for 1 h.

Substrate	CsFAMAPbIBr [M]	Ss [rpm]	Ac [rpm/s]	T [s]
11	1.0	4000	3996	45

Table 6.2. Conditions of the CsFAMAPbIBr perovskite precursor solution deposition. Ss: spin speed, Ac: acceleration speed, T: spin time.

6.2.3 Spiro-OMeTAD Infiltration

To reach the target of having 2,2',7,7'-Tetrakis[N,N-di(4-methoxyphenyl)amino]-9,9' spirobifluorene (spiro-OMeTAD) with a height between 100 nm and 300 nm a 70 mM spiro-OMeTAD solution was prepared, in a N_2-filled glovebox, as is described on chapter 3 (3.2.3.4). Subsequently, the solution was vigorously stirred and filtered (0.2 µm PTFE filter) before its deposition.

The conditions of the spiro-OMeTAD solution depositions are summarized in **table 6.3.** 100 µL of the 70 mM spiro-OMeTAD solution were dropped, in a dry-box, on the top of two wBL-NAA-TiO_2-CsFAMAPbIBr substrates prepared under similar conditions. Each substrate was spin-coated at a different spin speed: Ss_1 = 2500 rpm and Ss_2 = 1500 nm, (2000 rpm/s) for 30 s, to obtain the desired spiro-OMeTAD height between 100 nm and 300 nm.

Substrate	Spiro-OMeTAD [mM]	Ss [rpm]	Ac [rpm/s]	T [s]
12	70	2500	2000	30
13	70	1500	2000	30

Table 6.3. Conditions of the spiro-OMeTAD solution depositions. Ss: spin speed, Ac: acceleration speed, T: spin time.

Following, several NAA substrates with a nanoporous film thickness of about 650 nm, which barrier layers were previously removed were used as substrates. The TiO_2-NPs, CsFAMAPbIBr perovskite precursor solution and the spiro-OMeTAD solution were deposited as is indicated in **table 6.4**.

Material	C [M]	Vd [µL]	Ss [rpm]	Ac [rpm/s]	T [s]
TiO_2-NPs	0.5	100	-	-	-
TC	1	100	4000	3996	45
s-OMeTAD	0.70	100	2500	2000	30

Table 6.4. Conditions of the different solution depositions in a wBL-NAA with a nanoporous film thickness of 650 nm. TC: CsFAMAPbIBr, C: concentration, Ss: spin speed, Ac: acceleration speed, T: spin time.

First, 100 µL of the TiO_2-NPs dispersion number 10, (C = 0.5 mg/mL employing a mixture of H_2O:C_2H_5OH with a volume ratio of 1:1) were drop-casted on the top of the wBL-NAA substrates, to obtain the desired nanostructured TiO_2 layer thickness below 100 nm. Secondly, 100 µL of the 1 M CsFAMAPbIBr perovskite precursor solution were deposited, in a dry-box, on the top of the previously deposited layer. After waiting for 60 s to let the CsFAMAPbIBr perovskite precursor solution infiltration in the nanopores, the substrates were spin-coated at 4000 rpm (3996 rpm/s) for 45 s, to obtain the desired nanostructured CsFAMAPbIBr perovskite layer thickness between 400 nm and 600 nm. Then, the substrates were placed in a hotplate and they were annealed at 100 °C for 1 h. Finally, 100 µL of the 70 mM spiro-OMeTAD solution were dropped, in a dry-box, on the top of the previously deposited layer. The substrates were spin-coated at 2500 rpm (2000 rpm/s) for 30 s, to obtain the desired spiro-OMeTAD height between 100 nm and 300 nm. It is very important to consider that to increase the oxidative doping of the spiro-OMeTAD, substrates were kept in dark in a dry air chamber overnight before the thermal evaporation of the semi-transparent electrode.

6.2.4 Semi-Transparent Electrode

To achieve the goal of having a highly conductive semi-transparent electrode, the indium tin oxide-coated glasses (ITO) were used as substrates. The ITO films of the ITO glasses were removed and then a dielectric/metal/dielectric (DMD) multilayer was thermally evaporated over the glasses substrates. The DMD multilayer was composed of tungsten trioxide (WO_3) and silver (Ag).

Figure 6.1 shows the semi-transparent electrode structure which consists of one thin Ag film surrounded by WO_3 layers (WO_3/Ag/WO_3, WAW).

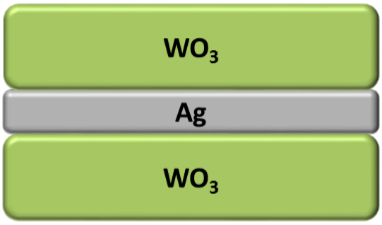

Figure 6.1. Structure of the semi-transparent WAW electrode.

First, various ITO glasses were immersed in a mix of hydrochloric acid (HCl) and zinc (Zn) to remove the ITO film by chemical etching. Subsequently, the glass substrates were carefully brushed with Hellmanex soap in deionized water solution and following they were cleaned by ultrasonication in the Hellmanex soap deionized water solution, then in isopropanol and finally in acetone for 15 min each. Afterwards, the substrates were placed in a UVO cleaning system for 10 min to remove the remaining organics and to increase their wettability.[188]

Secondly, the glasses substrates were positioned in a thermal evaporation chamber (vacuum pressure < $5x3^{-6}$ torr, in an N_2-filled glovebox) and diverse WAW multilayers were thermally deposited over the glasses substrates. To find the optimal structure of the WAW multilayer several semi-transparent electrodes with Ag thicknesses varying between 8 nm and 14 nm were studied (**table 6.5**).[254]

Number	Conditions
1	WO_3 50 nm/Ag 8 nm/WO_3 50 nm
2	WO_3 50 nm/Ag 10 nm/WO_3 50 nm
3	WO_3 50 nm/Ag 12 nm/WO_3 50 nm
4	WO_3 50 nm/Ag 14 nm/WO_3 50 nm

Table 6.5. Conditions of the WAW multilayers proposed as semi-transparent electrodes.

6.2.5 Nanostructured Perovskite Solar Cell Device Fabrication

To fabricate a nanostructured perovskite solar cell (nPSC) device, several wBL-NAA substrates, prepared under identical conditions, with a nanoporous film thickness of about 650 nm, were used as substrates. The TiO_2-NPs, CsFAMAPbIBr perovskite precursor solution and the spiro-OMeTAD solution were deposited as is explained at the end of the section 6.2.3 (**table 6.4**). Following, the wBL-NAA-TiO_2-CsFAMAPbIBr-spiro-OMeTAD substrates were placed in the thermal evaporation chamber and using a thin-film mask the semi-transparent electrode was thermally deposited sequentially: WO_3 50 nm/Ag 12 nm/WO_3 50 nm. Afterwards, the thin-film mask was changed and 150 nm of Ag were thermally deposited. The effective active area of the devices is 0.19 cm^2.

6.3 Results and Discussion

6.3.1 Titanium Dioxide Infiltration

In this section, the results from SEM studies of the distinct TiO_2-NPs dispersion infiltrations are summarized and conclusions about the optimal conditions to achieve a uniform pore bottom filling are obtained.

Initially, the dispersions number 1 (C = 2 mg/mL), 3 (C = 5 mg/mL) and 5 (C = 10 mg/mL), employing a mixture of H_2O:C_2H_5OH with a volume ratio of 1:1 were tested.

Figures 6.2 a), **c)** and **e)** display the top SEM pictures and **figures 6.2 b)**, **d)** and **f)** exhibit the EDX spectra of the wBL-NAA substrates infiltrated with TiO_2-NPs dispersions in H_2O:C_2H_5OH (1:1) with a 2 mg/mL, 5 mg/mL and 10 mg/mL concentrations, respectively. Inserted in each EDX spectra there is an elemental mapping of the wBL-NAA-TiO_2 substrates.

From **figures 6.2 a)**, **c)** and **e)** nanopores with different grey tones can be distinguished. Some nanopores are black, others look cloudy and others are grey. For C = 2 mg/mL [**figure 6.2 a)**] nanopores with distinct grey tones can be seen, most of them are black and the nanopores circled by blue look cloudy. While for C= 5 mg/mL [**figure 6.2 c)**] and C = 10 mg/mL [**figure 6.2 e)**] there are only nanopores with one grey tone, but with the difference that the nanopores are black and grey, respectively.

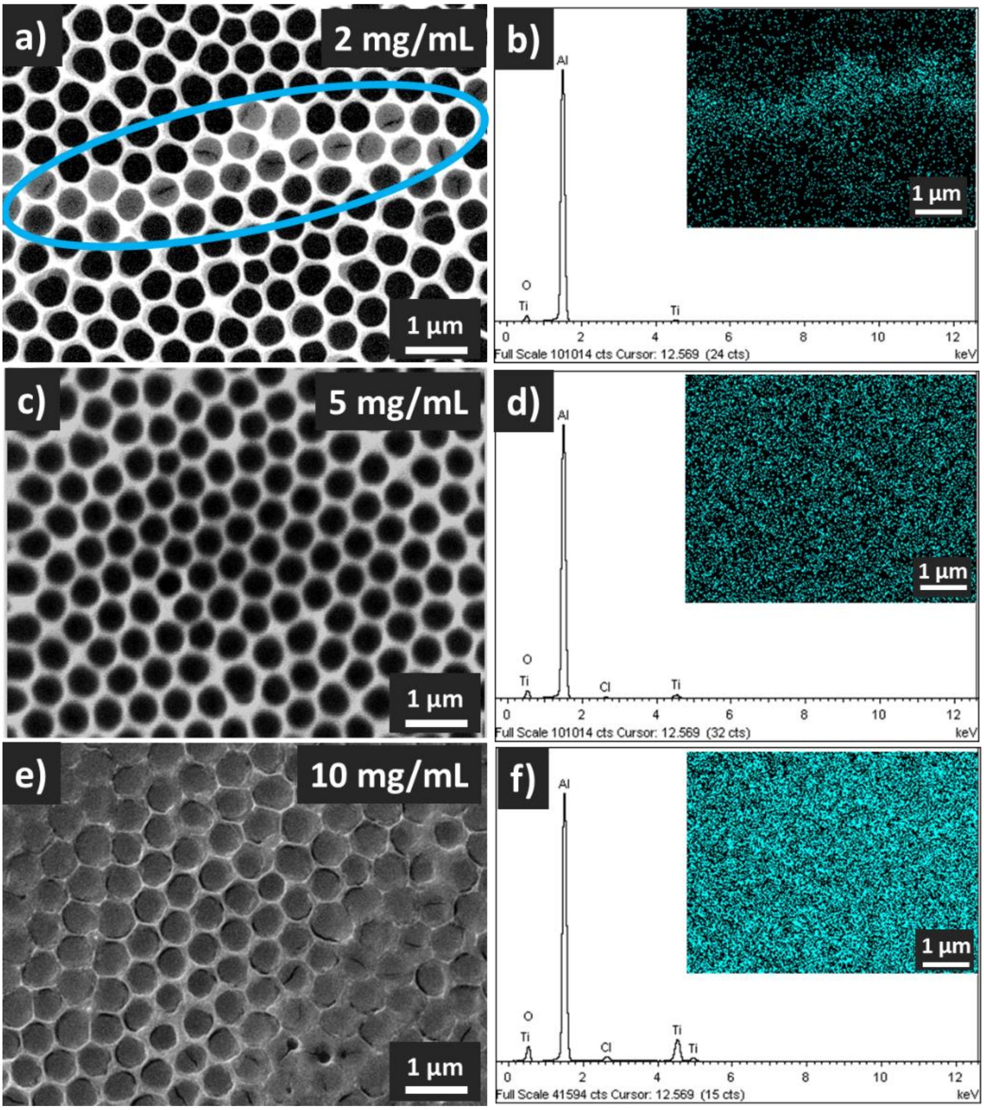

Figure 6.2. a), **c)** and **e)** top SEM views and **b)**, **d)** and **f)** EDX elemental analysis of the wBL-NAA substrates infiltrated with different TiO_2-NPs dispersions in H_2O:C_2H_5OH (1:1) with concentrations of 2 mg/mL, 5 mg/mL and 10 mg/mL, respectively, via spin-coating deposition. There is a mapping inserted in each EDX spectra. The scale bars are indicated in each picture.

In **figures 6.2 b)**, **d)** and **f)** the EDX elemental analysis demonstrates a strong peak corresponding to the aluminium (Al) since the wBL-NAA substrate base is aluminium. Two further peaks can be observed corresponding to the titanium (Ti) whose intensity depends on the amount of Ti. The mappings show the Ti distribution (therefore the TiO_2 distribution) represented by the blue dots. For C = 2 mg/mL [**figure 6.2 b)**] the highest concentration of blue dots in the middle of the picture can be seen. While for C= 5 mg/mL [**figure 6.2 d)**] and C = 10 mg/mL [**figure 6.2 f)**] the blue dots are distributed for all the area, but with the difference that the number of blue dots in **figure 6.2 f)** is bigger than in **figure 6.2 d)**.

The nanoporous layer thickness is about 1 µm. The differences in grey tone observed in the SEM pictures is given by the different filling degree of the nanopores. If the nanopores are partially filled (it is means less than 500 nm) they will be black. If the nanopores are almost filled (it means more than 500 nm and less than 1 µm) they will be cloudy. If the nanopores are filled (it is means 1 µm or more) they will be grey. Taking into account the previous comments, from **figure 6.2** it can be learned the following:

For C = 2 mg/mL [**figure 6.2 a)**] the nanopores circled by blue are almost filled and the rest of the nanopores are not. This can be confirmed with the mapping inserted in **figure 6.2 b)**. The highest concentration of blue dots is in the middle of the picture, this means that there is a high amount of Ti and therefore TiO_2 within these nanopores.

For C = 5 mg/mL [**figure 6.2 c)**] most of the nanopores are partially filled. The mapping inserted in **figure 6.2 d)** exhibits how the blue dots are distributed for all over the area, this means that the Ti and therefore TiO_2 is homogeneously dispersed within the nanopores.

For C = 10 mg/mL [**figure 6.2 e)**] the nanopores are filled with TiO_2. In the mapping inserted in the **figure 6.2 f)** there is a high concentration of blue dots in all the area, this means that there is a high amount of Ti and therefore the TiO_2 is filling the nanopores.

Figure 6.2 a) demonstrates a non-homogeneous TiO_2 distribution within the nanopores since some nanopores are partially filled and others are not. **Figures 6.2 c)** and **e)** display a distribution more homogeneous than **figure 6.2 a)** since most of the nanopores are partially filled and filled, respectively.

The results of this test show that to achieve a nanostructured TiO_2 layer thickness below 100 nm homogeneously deposited on the whole wBL-NAA area, dispersions number 1 (C = 2 mg/mL) and 5 (C = 10 mg/mL) should be discarded as they tend to have nanopores partially filled and filled, respectively.

A cross-section SEM of the wBL-NAA corresponding to the dispersion number 3 (C = 5 mg/mL) was obtained to estimate the actual amount of infiltrated TiO_2. **Figures 6.3 a)** and **b)** display the cross-section SEM pictures of NAA-wBL substrate infiltrated with a TiO_2-NPs dispersion in $H_2O:C_2H_5OH$ (1:1), with a concentration of 5 mg/mL. The blue arrows mark the TiO_2. From **figures 6.3 a)** and **b)** the nanostructured TiO_2 layer thickness was estimated at 500 nm.

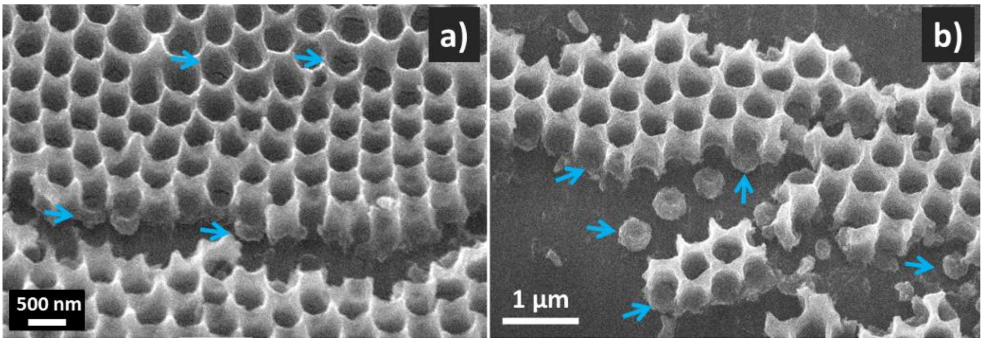

Figure 6.3. a) and **b)** cross-section SEM views of NAA-wBL substrate infiltrated with a TiO_2-NPs dispersion in $H_2O:C_2H_5OH$ (1:1) with a concentration of 5 mg/mL, via spin-coating deposition. The scale bars are indicated in each picture and the TiO_2 is marked by blue arrows.

Secondly, the dispersions number 2 (C = 2 mg/mL), 4 (C = 5 mg/mL) and 6 (10 mg/mL), employing a mixture of $H_2O:C_2H_5OH$ with a volume ratio of 1:3 were tested. **Figures 6.4 a)** and **c)** exhibit the top and **figures 6.4 b)** and **d)** demonstrate the cross-section SEM pictures of the wBL-NAA substrates infiltrated with the TiO_2-NPs dispersions in $H_2O:C_2H_5OH$ (1:3) with a 2 mg/mL and 5 mg/mL concentrations, respectively. The blue arrows are marking the TiO_2.

In **figures 6.4 a)** and **b)** two zones can be distinguished. A zone in which the nanopores are black and a zone in which there is a grey film on top of NAA structure. While from **figures 6.4 c)** and **d)** only nanopores with a grey colour can be seen. Following the same analysis as for the dispersions number 1, 3 and 5, for C = 2 mg/mL [**figure 6.4 a)** and **b)**] it can be seen as a high portion of the nanopores are filled with the TiO_2. For C = 5 mg/mL [**figure 6.4 c)** and **d)**] it can be observed as the nanopores are filled with the TiO_2.

Comparing the pictures corresponding to C **=** 2 mg/mL [**figure 6.4 a)**] and C **=** 5 mg/mL [**figure 6.4 c)**] in H_2O:C_2H_5OH (1:3) with the pictures corresponding to C **=** 2 mg/mL [**figure 6.2 a)**] and C **=** 5 mg/mL [**figure 6.2 c)**] in H_2O:C_2H_5OHOH (1:1) exhibit a similar TiO_2 distribution within the nanopores. But, a difference in the nanopores filling can be noticed, **figure 6.4 a)** displays most of the nanopores filled while the **figure 6.4 c)** displays all the nanopores filled, instead, **figure 6.2 a)** demonstrates most of the nanopores partially filled and the **figure 6.2 c)** shows all the nanopores almost filled.

This result can be caused by the fact that C_2H_5OH is more volatile than H_2O, consequently, C_2H_5OH evaporates faster than H_2O. When the solution is dropped on the substrate, if the droplet volume is smaller, evaporation will take a shorter time and the solution has not enough time to infiltrate the nanopores. Therefore, the TiO_2-NPs will be covering the nanopores. In this case, the substrates corresponding to the concentration of 10 mg/mL was not characterized by SEM because employing the 5 mg/mL concentration dispersion the nanopores are already filled. With these results, it can be concluded that the most homogeneous TiO_2 distribution was achieved with the number 3 dispersion: 5 mg/mL in H_2O:C_2H_5OH (1:1). Nevertheless, the nanostructured TiO_2 layer thickness is estimated at 500 nm, which is too thick, since the aim is to achieve a nanostructured TiO_2 layer thickness below 100 nm.

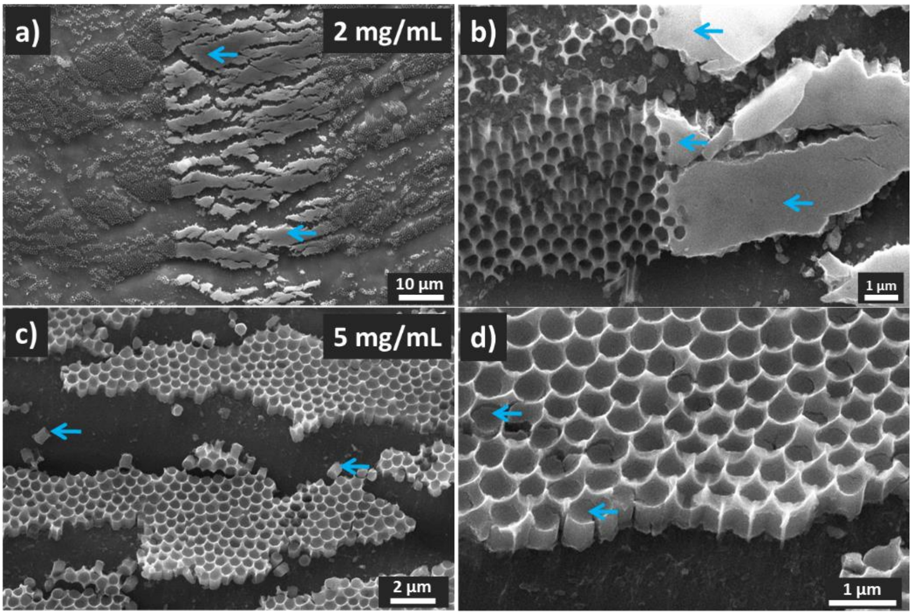

Figure 6.4. a) and **b)** top and **c)** and **d)** cross-section SEM views of the wBL-NAA infiltrated with TiO_2-NPs dispersions in H_2O:C_2H_5OH (1:3) with a concentration of 2 mg/mL and 5 mg/mL, respectively, via spin-coating deposition. The scale bars are indicated in each picture and the TiO_2 is marked by blue arrows.

Finally, dispersions number 7 (C = 3 mg/mL), number 8 (C = 1.5 mg/mL), number 9 (C = 1 mg/mL) and number 10 (C = 0.5 mg/mL), employing a mixture of H_2O:C_2H_5OH with a volume ratio of 1:1 were tested.

Figures 6.5 a), **b)**, **c)** and **d)** display the top SEM pictures of the wBL-NAA substrates infiltrated with a TiO_2-NPs dispersion in H_2O:C_2H_5OH, with a volume ratio 1:1 and with TiO_2-NPs concentrations of 3 mg/mL, 1.5 mg/mL, 1 mg/mL and 0.5 mg/mL, respectively. In **figure 6.5** nanopores with a distinct colour can be distinguished. Some nanopores are black and others are grey.

Following the same analysis as for the dispersions number 1 to 6, for C = 3 mg/mL [**figure 6.5 a)**], C = 1 mg/mL [**figure 6.5 c)**] and C = 0.5 mg/mL [**figure 6.5 d)**], it can be seen as most of the nanopores are partially filled, on the other hand, for C = 1.5 mg/mL [**figure 6.5 b)**] most of the nanopores are almost filled. **Figures 6.5 a)**, **c)** and **d)** exhibit a homogeneous TiO_2 distribution while **b)** demonstrates a no homogeneous distribution. Therefore, a cross-section SEM of the wBL-NAA substrates infiltrated with C = 3 mg/mL, C = 1 mg/mL and C = 0.5 mg/mL were obtained to estimate the actual amount of infiltrated TiO_2.

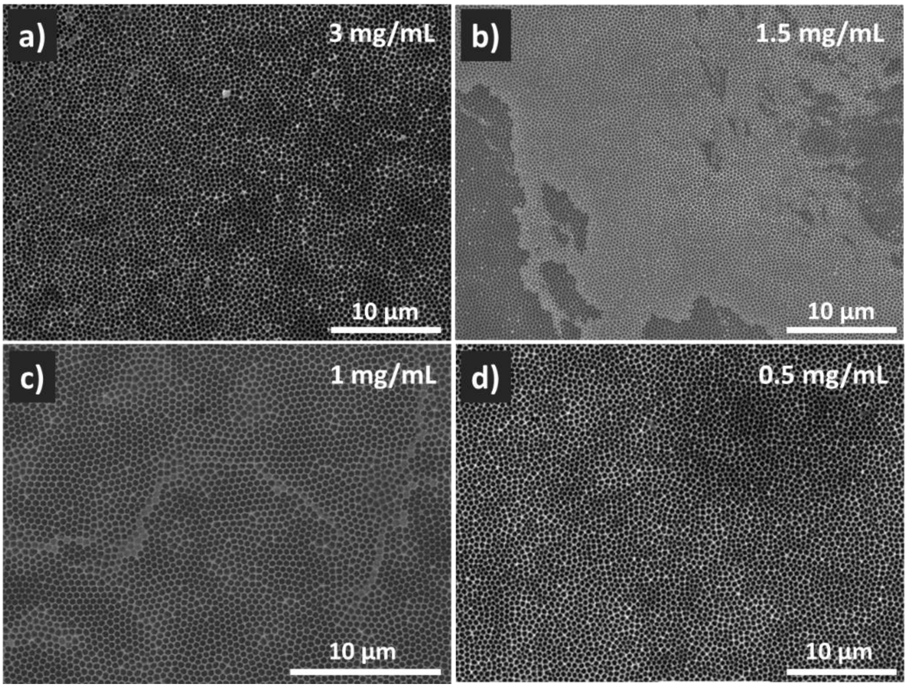

Figure 6.5. a), b), c) and **d)** top SEM views of the wBL-NAA infiltrated with different TiO_2-NPs dispersions in $H_2O:C_2H_5OH$ (1:1) with concentrations of 3 mg/mL, 1.5 mg/mL, 1 mg/mL and 0.5 mg/mL, respectively, *via* spin-coating deposition. The scale bars are indicated in each picture.

Figures 6.6 a), **b)**, and **c)** display the cross-section SEM pictures of the wBL-NAA substrates infiltrated with the TiO_2-NPs dispersion in $H_2O:C_2H_5OH$ (1:1) and with concentrations of 3 mg/mL, 1 mg/mL and 0.5 mg/mL respectively. The blue arrows are marking the TiO_2. From **figure 6.6 a)** nanostructured TiO_2 layer thickness was estimated at 300 nm, which is still too thick and from **figures 6.6 b)** and **c)** nanostructured TiO_2 layers thicknesses were estimated lower than 100 nm. Also, TiO_2-NPs are covering the aluminium surface. As a consequence of the method to open the cross-section for the SEM investigation.

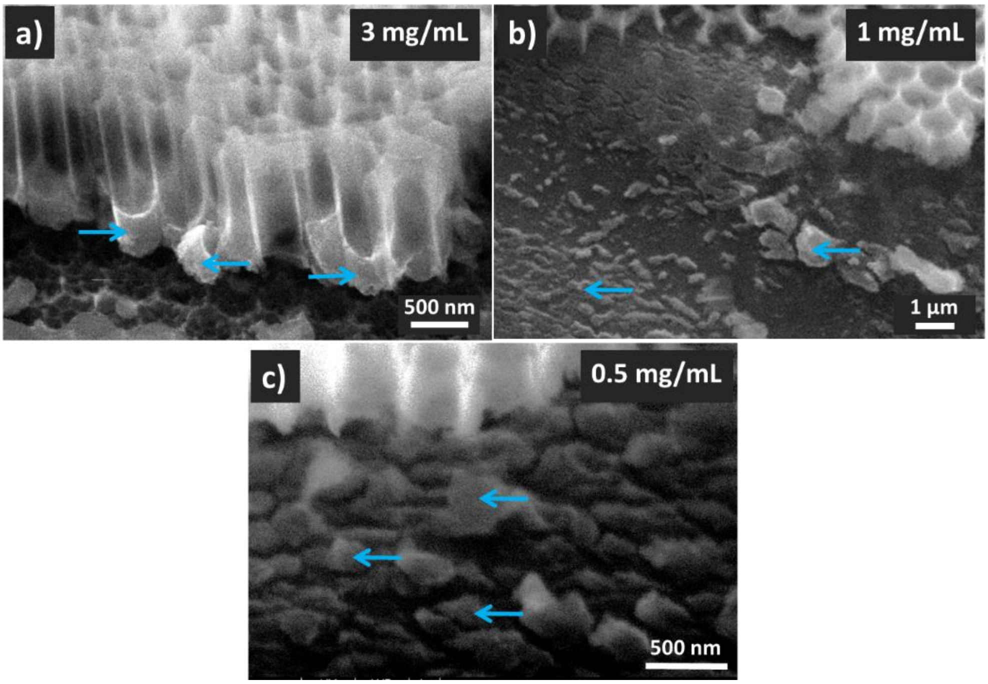

Figure 6.6. a), **b)**, and **c)** cross-section SEM views of the wBL-NAA infiltrated with different TiO_2-NPs dispersions in $H_2O:C_2H_5OH$ (1:1) with concentrations of 3 mg/mL, 1 mg/mL and 0.5 mg/mL, respectively, via spin-coating deposition. The scale bars are indicated in each picture and the TiO_2 is marked by blue arrows.

6.3.2 CsFAMAPbIBr Perovskite Infiltration

To estimate the nanostructured CsFAMAPbIBr perovskite layer thickness within the nanopores a line profile analysis of the wBL-NAA-TiO_2-CsFAMAPbIBr substrates was carried out.

Figure 6.7 a) shows an AFM picture of the wBL-NAA-TiO_2 surface topography after the 1 M CsFAMAPbIBr solution infiltration. In **figure 6.7 a)** three lines across NAA surface: a green, a blue and a pink one can be seen. Each line is formed by a set of nanopores. **Figures 6.7 b)**, **c)** and **d)** exhibit the lines profiles analysis across the lines indicated in **a)**. In **figures 6.7 b)**, **c)** and **d)** the highest (w_1, w_2 …) and lowest (p_1, p_2 …) points refer to the centres of walls and nanopores, respectively. Therefore, remaining unfilled nanopore depth can be estimated as the average of the subtraction of the highest and lowest adjacent points, for example, w_1-p_1 or w_3-p_3.

From **figures 6.7 b), c)** and **d)** in an area of 10 µm x 10 µm, the average of the unfilled nanopores depth detected by AFM tip is 535 nm, 220 nm and 397 nm, respectively. The average of these measured unfilled nanopores depth is 384 nm. Considering that the length of the nanopores is 1 µm and the height of the TiO_2 layer previously infiltrated was estimated at 70 nm, the nanostructured CsFAMAPbIBr perovskite layer thickness within the nanopores is estimated at 546 nm.

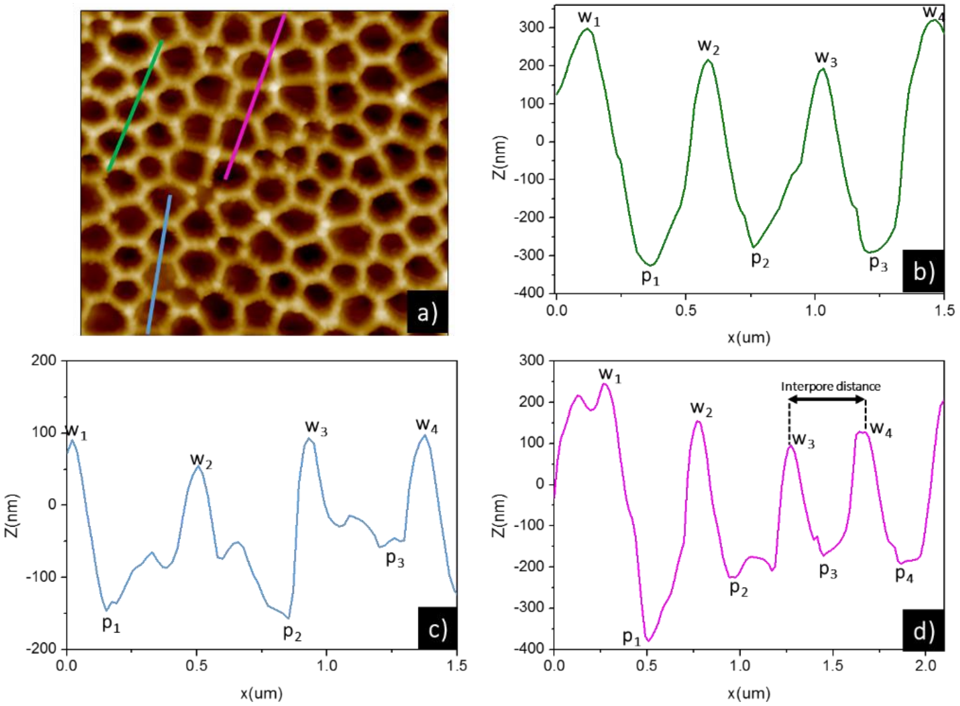

Figure 6.7. a) AFM picture (10 x 10 µm) of a NAA-wBL-TiO_2-CsFAMAPbIBr substrate **b)**, **c)** and **d)** line profiles analysis across the nanopores set of the green, blue and pink lines indicated in **a)** respectively.

6.3.3 Spiro-OMeTAD Infiltration

To estimate the nanostructured spiro-OMeTAD layer thickness within the nanopores, a line profile analysis of NAA-TiO_2-CsFAMAPbIBr-spiro-OMeTAD substrates was conducted.

Figure 6.8 a) shows an AFM picture of wBL-NAA-TiO_2-CsFAMAPbIBr surface topography after the 70 mM spiro-OMeTAD solution infiltration with Ss_1 = 2500 rpm. In **figure 6.8 a)** three lines across NAA surface: a green, a blue and a pink one can be seen. Each line is formed by a set of nanopores. **Figures 6.8 b)**, **c)** and **d)** display the lines profiles analysis across the lines indicated in **a)**.

Following the same analysis as for the wBL-NAA-TiO_2-CsFAMAPbIBr substrates, the estimated remaining unfilled nanopores depth for Ss_1 = 2500 rpm [**figures 6.8 b)**, **c)** and **d)**] in an area of 10 µm x 10 µm is 148 nm, 163 nm and 145 nm, respectively. The average of the measured depths is 152 nm. Considering that the length of the nanopores is 1 µm and the height of the layers previously infiltrated was estimated at 616 nm, the nanostructured spiro-OMeTAD layer thickness within the nanopores is estimated at 232 nm.

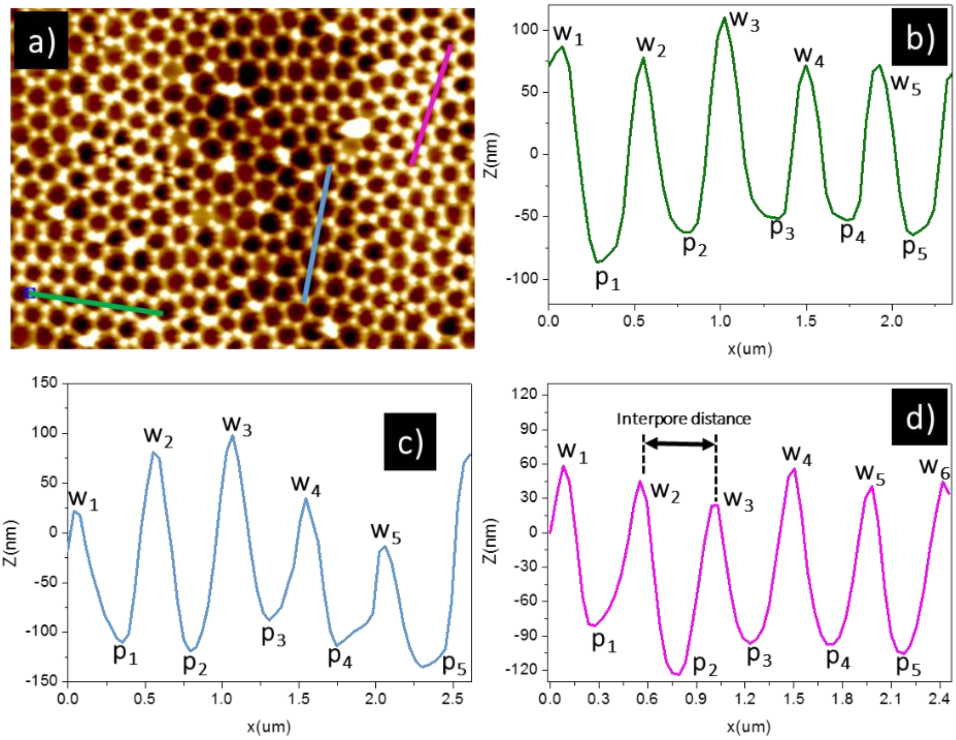

Figure 6.8. a) AFM picture (10 x 10 µm) of a NAA-wBL-TiO_2-CsFAMAPbIBr-spiro-OMeTAD (Ss_1 = 2500 rpm). **b)**, **c)** and **d)** lines profiles analysis across a set of nanopores of the green, blue and pink lines indicated in **a)**, respectively.

Figure 6.9 a) shows an AFM picture of the wBL-NAA-TiO_2-CsFAMAPbIBr surface topography after the 70 mM spiro-OMeTAD solution infiltration with Ss_2 = 1500 rpm. In **figure 6.9 a)** three lines across NAA surface: a green, a blue and a pink one can be seen. Each line is formed by a set of nanopores. **Figures 6.9 b)**, **c)** and **d)** display the lines profiles analysis across the lines indicated in **a)**.

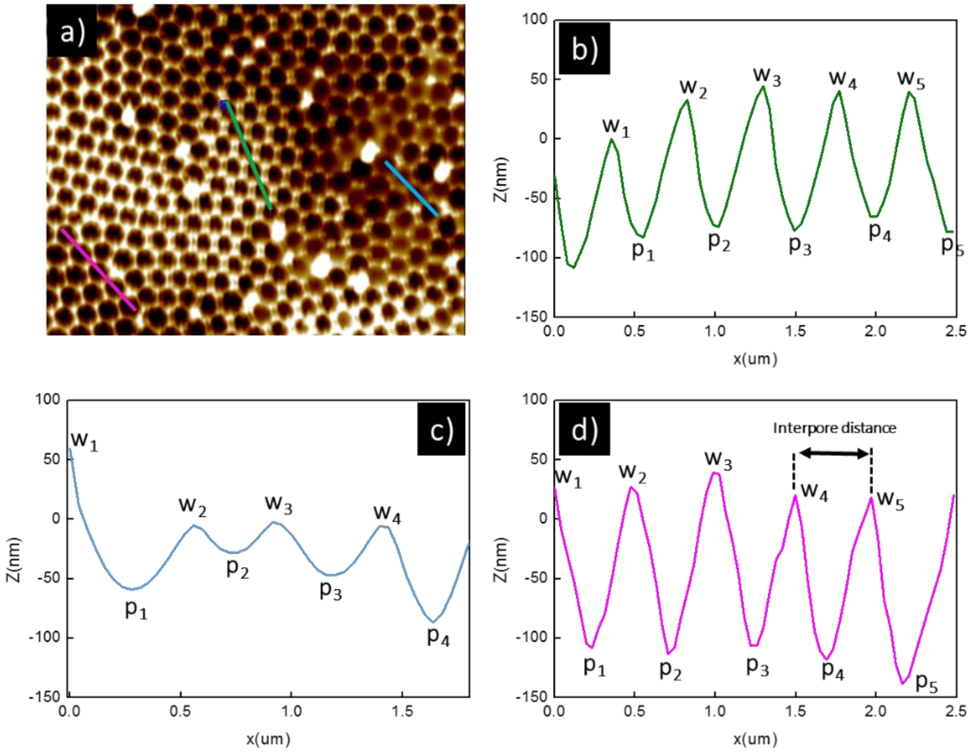

Figure 6.9. a) AFM surface topography image of NAA-wBL-TiO_2-CsFAMAPbIBr-spiro-OMeTAD (Ss_2= 1500 rpm). **b)**, **c)** and **d)** lines profiles analysis along the green, blue and pink lines, respectively.

For Ss_2 = 1500 rpm [**figures 6.9 b)**, **c)** and **d)**] in an area of 10 nm x 10 nm the estimated unfilled nanopores depth is 104 nm, 73 nm and 147 nm, respectively. The average of the measured depths is 107.6 nm. Considering that the length of the nanopores is 1 µm and the height of the layers previously infiltrated is estimated at 616 nm, the height of the spiro-OMeTAD within the nanopores is estimated at 277 nm.

In summary, the nanostructured spiro-OMeTAD layer thickness obtained in the substrates spin-coated at 2500 rpm and 1500 rpm are 232 nm and 277 nm, respectively. From **figures 6.8** and **6.9** it can be seen as the nanopores were not filled with the spiro-OMeTAD solution in any test. The nanostructured spiro-OMeTAD layer should fill the nanopores and formed a flat film which covers NAA surface. Although using Ss_2 = 1500 rpm [**figure 6.8**] it is achieved nanopores more filled than using Ss_1 = 2500 rpm [**figure 6.9**] the nanopores were not filled yet. The nanostructured spiro-OMeTAD layer thicknesses were not enough to fill the nanopores and cover NAA surface, therefore it needs a thicker thickness of the spiro-OMeTAD layer. However, the spiro-OMeTAD height should not be bigger than 300 nm, so wBL-NAA with a nanoporous film thickens of 650 nm were tested. To check that the nanostructured spiro-OMeTAD layer is not only filling the nanopores but also is covering NAA surface, an AFM study of the wBL-NAA-TiO_2-CsFAMAPbIBr-spiro-OMeTAD substrates, with a nanoporous film thickness of 650 nm, was carried out.

Figure 6.10 shows an AFM picture of the wBL-NAA-TiO_2-CsFAMAPbIBr surface after the 70 mM spiro-OMeTAD solution infiltration, which was spin-coated employing a Ss_1 = 2500 rpm (2000 rpm/s) for 30 s. The nanopore structure of NAA surface cannot be observed. This indicates that spiro-OMeTAD has infiltrated the nanopores filling them and also has formed a film over NAA surface.

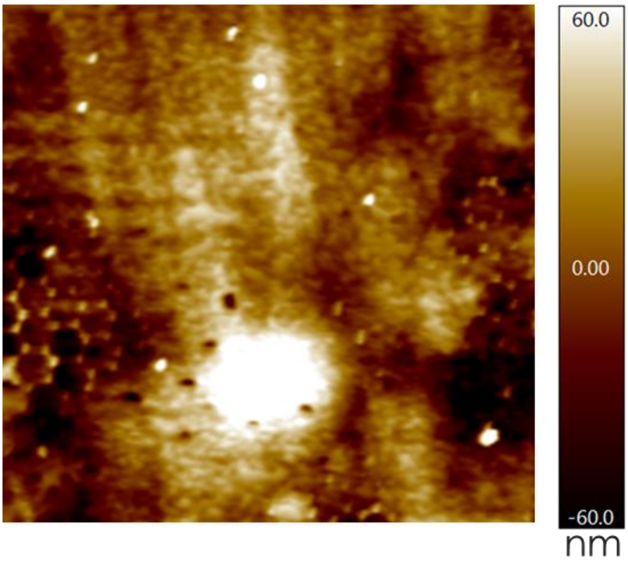

Figure 6.10. AFM picture (10 x 10 µm) of a wBL-NAA-TiO_2-CsFAMAPbIBr-spiro-OMeTAD with a nanoporous thickness layer of 650 nm. The scale is indicated in the picture.

6.3.4 Semi-Transparent Electrode Characterization

To find a highly conductive semi-transparent electrode the optical and electric properties of the proposed semi-transparent electrodes were studied. The measured average transmittance (T_{avg}), measured average sheet resistance (Rs_{avg}) and Figure-of-Merit (FoM) values of the WAW multilayers electrodes as a function of the Ag thickness (δ_{Ag}) and the ITO substrate are shown in **table 6.6**.

N	Conditions	T_{avg} [%]	Rs_{avg} [Ω/sq]	FoM [Ω^{-1}]
1	WO_3 50 nm/Ag 8 nm/WO_3 50 nm	40	42.60	7.6
2	WO_3 50 nm/Ag 10 nm/WO_3 50 nm	38	5.25	57.7
3	WO_3 50 nm/Ag 12 nm/WO_3 50 nm	44	2.67	139.1
4	WO_3 50 nm/Ag 14 nm/WO_3 50 nm	19	3.04	47.9
5	ITO	85	17	131.0

Table 6.6. T_{avg}: measured average transmittance, Rs_{avg}: measured average sheet resistance and FoM: Figure-of-Merit values of the WAW multilayer electrodes as a function Ag thickness.

Figure 6.11 exhibits the optoelectronic characterization of the WAW multilayers electrodes summarized in **table 6.6** as a function of Ag thickness (δ_{Ag}). **a)** Transmittance spectra of the electrodes as a function of wavelength (300-800 nm). For comparison, the reference glass substrate and the ITO substrate were also included. **b)** Measured average transmittance (300-800 nm) and measured average sheet-resistance. **c)** Correlation between the measured average transmittance, Ag thickness and measured average sheet-resistance. **d)** Figure-of-Merit (FoM) of the proposed semi-transparent electrodes. To evaluate and compare the performance of the different electrodes tested and also compare them with the standard electrode (ITO) it is needed to define a FoM. This FoM must take into account the transparency and conductivity, which are antagonistic properties. To find the optimal ratio between electrical and optical conductivity of WAW prepared films, closely dependent on the δ_{Ag}, the electrical to optical conductivity ratio [$\sigma_{DC}/\sigma_{OP}=185.5/Rs_{avg}*(T_{avg}^{-1/2}-1)$] used by Sepulveda *et al.*[255] was employed as FoM relating T_{avg} and Rs_{avg}.

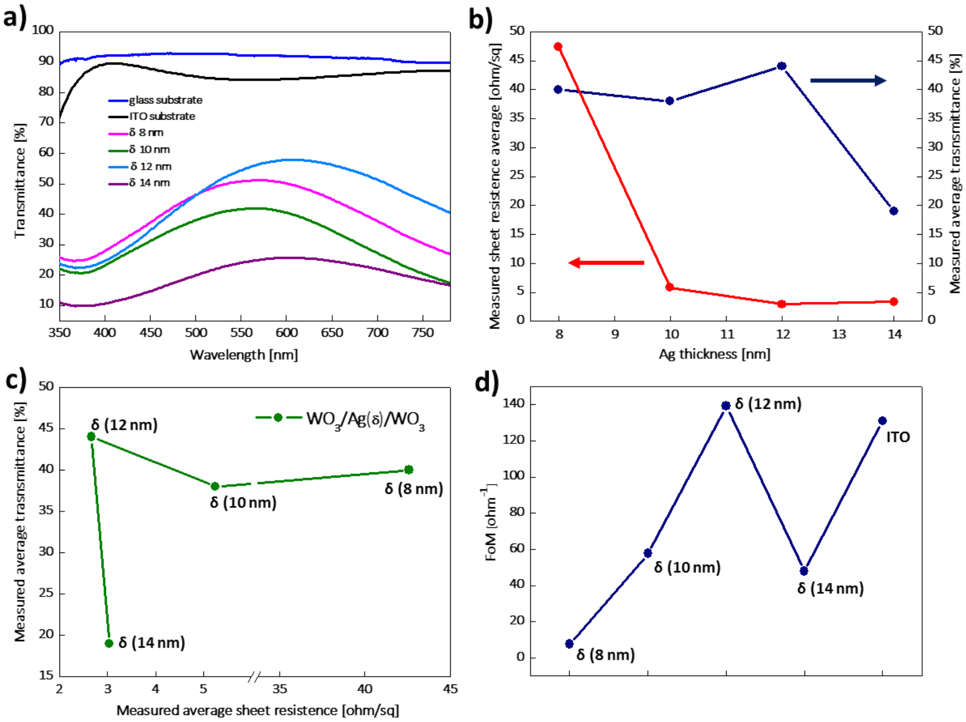

Figure 6.11. Optoelectronic characterization of WAW multilayer semi-transparent electrodes as a function of Ag thickness (δ_{Ag}) **a)** Optical transmittance spectra of the WAW substrates, the reference glass substrate and the ITO substrate. **b)** Measured average transmittance and measured sheet resistance. **c)** Correlation between the measured average transmittance, the measured sheet resistance and Ag thickness. **d)** Figure-of-Merit of the proposed semi-transparent electrodes.

Figure 6.11 b) shows the change in T_{avg} (300-800 nm) and Rs_{avg} of the WAW multilayers as a function of δ_{Ag}. It is assumed that all thin-film layers (regarding optics) are continuous film.[256] However, Ag films thermally evaporated has a preference for island-like growth, due to the surface diffusion of Ag atoms.[257,258] It is thought that Ag morphology to enhance the optical transmittance since Ag light absorption is greatly increased when the Ag layer has an island-like morphology.[259,260] It has also been studied that increasing δ_{Ag} results in a transition of the surface shape from islands to a continuous film.[219]

From δ_{Ag} = 8 nm to δ_{Ag} = 10 nm the T_{avg} value undergoes a small decrease, from δ_{Ag} = 10 nm to δ_{Ag} = 12 nm the T_{avg} value experiences a small increase and from δ_{Ag} = 12 nm to δ_{Ag} = 14 nm the T_{avg} value bears a major decrease. The low transmittance at thicknesses less than 12 nm (δ_{Ag} = 8 nm and δ_{Ag} = 10 nm) originates from the discontinuous island growth of Ag, leading to scattering losses at the interface of Ag with WO_3.[261] However, the transmittance decrease at δ_{Ag} above 12 nm is caused by the high reflectance of the Ag layer.[261]

From δ_{Ag} = 8 nm to δ_{Ag} = 10 nm the Rs_{avg} value endures a major decrease, from δ_{Ag} = 10 nm to δ_{Ag} = 12 nm the Rs_{avg} value goes through a small decrease and from δ_{Ag} = 12 nm to δ_{Ag} = 14 nm the Rs_{avg} value has a small increase. The Rs_{avg} decreased from 42.6 ohm/sq to 2.67 ohm/sq with the increase of δ_{Ag} from 8 nm to 12 nm and increase from 2.67 ohm/sq to 3.04 ohm/sq with the increase of δ_{Ag} from 12 nm to 14 nm.

These results indicate that the thickness of Ag plays a critical role in the determination of T_{avg} and Rs_{avg}. The substrate with an δ_{Ag} of 12 nm presents the best optical proprieties with a T_{avg} of 44%. While the substrates with an δ_{Ag} of 8 nm, 10 nm and 12 nm have good electrical properties.[262]

Figure 6.11 c) displays the correlation between of T_{avg}, δ_{Ag} and Rs_{avg}. This figure demonstrates that the optimal value is achieved when δ_{Ag} is 12 nm.

Figure 6.11 d) shows the FoM values. The FoM value increases with δ_{Ag} reaching a maximum value of 139.1 Ω^{-1} at δ_{Ag} = 12 nm and decreases to 47.9 Ω^{-1} at δ_{Ag} = 14 nm. Therefore, the latter suggests that the WAW with at δ_{Ag} = 12 nm should present the best performance as semi-transparent electrode.

The FoM value of the WAW multilayer electrode with a δ_{Ag} of 12 nm is superior to ITO. This is because the WAW multilayers have better electrical conductivity and surface roughness than ITO, although its transmittance is slightly lower.[263]

6.3.5 Nanostructured Perovskite Solar Cell Device

The current-density *(J-V)* characteristics of the best performing nPSC device (pink line) under AM 1.5G irradiation in comparation with the nPSCs fabricated in the previous chapter, are shown in **figure 6.12**. The primary performance parameters values of the device in comparation with the nPSCs fabricated in the previous chapter are summaries in **table 6.7**, open-circuit voltage (V_{oc}), short-circuit current density (J_{sc}), fill factor (FF) and power conversion efficiency (PCE).

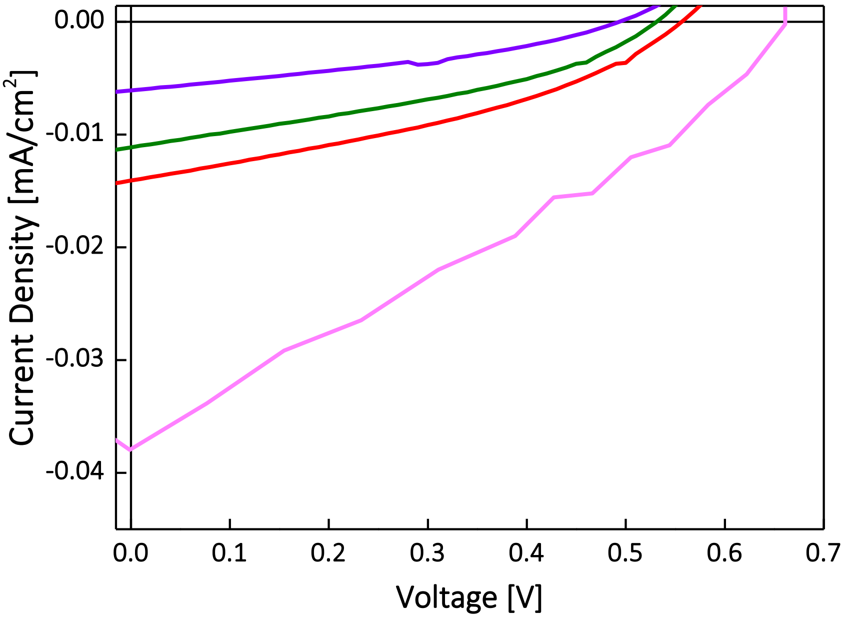

Figure 6.12. *J-V* characteristics of the best performing nPSC device (pink line) under AM 1.5G irradiation in comparation with the nPSCs fabricated in the previous chapter.

	Purple	Green	Red	Pink
V_{oc} [V]	0.49	0.53	0.56	0.58
J_{sc} [mA/cm^2]	0.006	0.011	0.014	0.04
FF [%]	38	36	36	44
PCE [%]	0.01	0.02	0.03	0.07

Table 6.7. Primary performance parameters values of the best-performing nPCS device (pink) measured at 1 SUN A.M. 1.5 illumination (100 mWcm^{-2}) in comparation with the nPSCs fabricated in the previous chapter. V_{oc}: open-circuit voltage, J_{sc}: short circuit current density, FF: fill factor and PCE: power conversion efficiency.

The changes produced in the structure of the nPSC device have resulted in a slight improvement of the primary performance parameters values. However, the results obtained are still too low in comparison with high-efficiency PSCs. It may also be due to too morphological complexity of the device and the absorbance of the anode. A preliminary study of the device with CsFAMAPbIBr perovskite was conducted. We should carry out more characterisation as a SEM study to compare both devices (chapter 5 and 6).

The effective active area of the devices was calculated with the area of the illuminated device (0.19 cm^2). However, alumina is an insulating material, it should be taken into account to calculate the theoretical effective active area of the devices. The porosity of alumina is about 10%[66]. So, the theoretical density current and efficiency values can be corrected in a 10 factor.

6.4 Conclusions

In this chapter, the possibility of infiltrating TiO_2 nanoparticles from its dispersion with an anatase crystalline form, to avoid thermal treatment carried out in section 5.2.1, is demonstrated. Also, $MAPbI_3$ perovskite is replacing by CsFAMAPbIBr perovskite with good control of its height. The fact that different materials, e.g., oxides (TiO_2-NPs), hybrid organic-inorganic (CsFAMAPbIBr), organics (spiro-OMeTAD) can be infiltrated within the nanopores of wBL-NAA *via* simple deposition methods such as spin-coating or drop-casted is corroborated. Besides, these materials can be infiltrated in wBL-NAA with a nanoporous film thickness of about 650 nm is proved. The use of a wBL-NAA with a nanoporous film thickness of about 650 nm permits to deposit a smaller height of the spiro-OMeTAD layer, which filled the nanopores and also level the rough NAA surface, thus reducing the possibility of resistivity losses. In the same way as in chapter 5, various experiments to find the optimal thickness of each nanostructured layer were conducted. The best conditions to obtain the appropriate nanostructured layer thicknesses of each material are summarized in **table 6.8**.

Material	C [M]	Vd [µL]	Ss [rpm]	Ac [rpm/s]	T [s]
TiO_2	0.5	100	-	-	-
CsFAMAPbIBr	1	100	4000	3996	45
s-OMeTAD	0.70	100	2500	2000	30

Table 6.8. Best solutions depositions conditions to obtain the appropriate nanostructured layer thicknesses. C: concentration, Vd: deposited volume, Ss: spin speed, Ac: spin acceleration, T: spin time.

Furthermore, in this chapter, the improvement of the semi-transparent electrode transmittance has also been studied. The results show that it is possible to reduce the number of layers of the transparent electrode from 5 to 3 while maintaining a good figure of merit for the transmittance and the electrical conductance. This reduction is especially significant as it permits to reduce steps in the fabrication protocols, with the subsequent increase in the robustness of the design.

After these changes, the performance parameters values undergo a slight increase. However, the current density and power conversion efficiency values are still too low.

Chapter 7

Conclusions

In the following chapter, the general conclusions of the thesis and the overall results achieved during this research are summarized. Future works related to this research are also added.

As is already explained, in this thesis, NAA-based nanotechnology is expected to be applied to the manufacture of perovskite solar cells. For this reason, first, the familiarization process with the manufacture and characterization of NAA, as well as of high-efficiency PSCs, by known standard methods were carried out.

When the manufacture and characterization of NAA with diverse nanopore sizes is controlled, the alumina barrier layer that exists between the aluminium and the bottom of the nanopores had to be removed, to take advantage of the aluminium (base of NAA) as an electrical contact. A new method for thick (more than 200 nm) barrier layer removal of NAA without removing the aluminium substrate is studied and presented. This method is based on a re-anodized step at a constant current density and chemical etchings. After several tests at different constant current densities, we demonstrate that the best condition for removing the barrier layer is to fix the constant density current at 17.0 $\mu A/cm^2$ in the constant current re-anodization step, using as electrolyte a solution of H_3PO_4 (1% wt.). The barrier layer-free NAA formation allows the establishment of electric contact between the aluminium of NAA substrates and the infiltrated materials within the nanopores. While this method has been developed for NAA obtained with H_3PO_4 electrolytes, it can be extended to NAA fabricated with different electrolytes at high voltage anodization.

Once the manufacture of PSCs is also controlled, the infiltration of several materials (those that form PSCs devices) within the nanopores of barrier layer-free NAA is studied and achieved. The infiltrated materials can be oxides, hybrid organic-inorganic and organics, e.g., TiO_2, $MAPbI_3$ and spiro-OMeTAD. We prove that they can be infiltrated *via* simple deposition methods such as spin-coating. The material solutions concentration and the different deposition conditions, e.g., spin speed, spin acceleration and spin time and let controlling the height of the material infiltrates. Also, we demonstrate that the height of each material is homogeneous among all the nanopores. After several experiments at distinct conditions, we determine that the best conditions to obtain the appropriate nanostructure layer thicknesses of each material are summarized in **table 5.4**. Although the obtained efficiency values are low, results show that this methodology permits the preparation of fully working nanostructured perovskite solar cells (nPSCs) using NAA as a enclosure. The low measured efficiency can be due to several reasons. Such as possible bad contact between layers. The fact that the spiro-OMeTAD layer is too thick since it can lead to resistivity loss. Also, the semi-transparent electrode results in a low transmittance. Therefore, optimization of the proposed nPSC should be carried out.

The infiltration of the materials that form the PSCs devices within the nanopores (even with different nanoporous film thickness) of barrier layer-free NAA *via* simple deposition methods such as spin-coating or drop-casted is corroborated. As well as, the fact that we can control its height. Then various trials at diverse conditions, we establish that the best conditions to obtain the appropriate nanostructured layer thicknesses of each material are summarized in **table 6.4**. Furthermore, we demonstrate that the number of layers of the semi-transparent electrode can be reduced from 5 to 3 while maintaining a good figure of merit for the transmittance and the electrical conductance, reducing the steps in the fabrication protocols, with the subsequent increase in the robustness of the design. After these changes, the short circuit current density, open-circuit voltage, fill factor and power conversion efficiency values undergo a slight increase. However, the current density and power conversion efficiency values are still too low.

To summarised:

We have developed a novel method to remove the thick barrier layer (>200 nm) in NAA without removing the aluminium base.

We reach to infiltrate different materials with good control of their thickness and homogeneity among nanopores.

We achieve to establish an electrical contact between the aluminium and the infiltrated material.

We achieve to use the aluminum base of NAA substrates as a back electrical contact of solar devices.

We fabricated a novel type of nanostructured perovskite solar cell based on nanoporous anodic alumina.

Despite several nanostructured perovskite solar cell devices based on NAA technology were manufacture in this thesis, their power conversion efficiencies values were very modest. Since the structure proposed in this work is novel, a great number of experiments should be done, which could not be done due to lack of time. So, this project opens a wide path for future work, such as:

Analysis of the effects of nanopore diameter and nanopore thickness on the performance of nPSCs.

Study of the stability of the devices under temperature, radiation and humidity over time.

Employ other perovskites such as lead-free perovskites to decreases the ambient impact.

On the other hand, taking advantage of the fact that there is electrical contact between the aluminium and the bottom of the nanopores, the barrier layer-free NAA could be used as the template for manufacturing batteries or super capacitors.

Appendixes

Appendix 1. Characterization Techniques

In this section, the characterization techniques used to characterize the nanoporous anodic alumina substrates, the conventional flat and nanostructured perovskites solar cells manufacture in this thesis are described.

Scanning Electron Microscopy (SEM)

NAA structural characterization was performed using an environmental scanning microscope (SEM FEI Quanta 600) operating under high vacuum conditions. SEM pictures were analysed by ImageJ software. SEM is the most common technique use for analysing the microstructure of a solid specimen since it can not only observe the surface but also the transverse, tilt and cross-sections, as well as analyse the elemental composition by the energy dispersive X-ray analysis. In a typical SEM setup, electrons are emitted from a cathode filament toward an anode. A solid specimen surface is excited with a highly-focused energetic beam of electrons. There are two types of electrons used to produce an image in a SEM, secondary and backscattered electrons. When the primary electrons reach the surface, they are inelastically scattered by atoms in the specimen. These scattering events cause the primary beam to spread and create emission of secondary electrons and X-rays. These secondary electrons are detected and processed to generate an image of the specimen structure.[264,265]

Energy-Dispersive X-Ray Spectroscopy (EDX)

The materials infiltrated within NAA were chemically identified using a. EDX is considered a tool for identifying the chemical composition of a specimen. EDX analysis can give us information about the elemental composition of a sample and the concentration of an element. SEM equipment is often coupled with energy dispersive spectroscopy X-ray diffraction, thereby enabling elemental composition analysis. When a specimen is bombarding with a highly-focused energetic beam of electrons, the electrons of the specimen deliver energy in the form of X-rays, these energies are characteristic of the element which produced it. A detector measures the characteristic X-ray energy and intensity of each element.[266]

Atomic Force Microscopy (AFM)

It is the most commonly used technique for surface topography analysis as well as for the analysis of the mechanical, functional and electrical properties of the specimen surfaces. Also, AFM can evaluate the degree of ordering of the nanopores array, as well as NAA nanopores density and the diameters and external shape of the nanopores. A typical AFM setup comprises a silicon tip on a free-moving cantilever, commonly referred to as the probe. The probe is brought close to the specimen surface, the force from the specimen onto the tip causes the bending of the cantilever. This bending is measured employing a laser beam focused on the top side of the cantilever. The reflection of this beam is directed to a position-sensitive photodetector. The bending of the cantilever causes a deflection of the laser beam that is measured by the position-sensitive photodetector. With this technique, a height map of the specimen can be obtained by scanning the tip on the surface. [265,267]

Profilometry

The thin film thicknesses of the different layers were obtained using a Bruker DektakXT profilometer. Profilometry is a technique used to study the step heights, surface morphology and roughness of a specimen. There are two types of profilometers: stylus or optical. Stylus profilometers (employed in this thesis) use a probe that contacts the surface. Height variations are measured as either the stylus or the substrate is being moved. The mechanical movements of the stylus are converted to electrical signals, which are then amplified to give DC output signals. [268]

Basic Electrical Characterization

The most common method to characterize the photovoltaic performance of PSCs, as well as their electrical properties, is the measurement of their current density-voltage characteristics (J-V curve) in dark and under illumination conditions. The J-V measurements for PSCs and nPSCs in which the absorber layer was the MAPbI3 perovskite were carried out with a solar simulator (Abet Technologies model 11000 class type A, Xenon arc) and a Keithley 2400 Source-Measure Unit. The light intensity was calibrated to AM1.5G standard conditions by an NREL certified monocrystalline silicon photodiode. The J-V measurements for PSCs in which the absorber layer was the CsFAMAPbIBr perovskite were carried out with a 4200SCS Keithley system at a voltage swept speed around 50 mV/s in combination with an Oriel sol3A sun simulator, which was calibrated to AM1.5G standard conditions using an Oriel 91150 V reference cell.

The sheet resistance (Rs) of the deposited layers was measured using the four-point probe technique employing a 4200SCS Keithley system. It is an apparatus for measuring the resistivity (sheet resistance) of semiconductor specimens, particularly semiconductor thin films. It works by driving a current through two outer probes which induce a voltage through the inner probes. The voltage through the inner probes is measured allowing so the measurement of the specimen resistivity.[269]

Optical Transmittance

The transmittance (T) was measured in the perovskites absorption region (300-800 nm) using a Cary 100 Agilent spectrophotometer.

Ultraviolet-Visible Spectrophotometry

The ultraviolet-visible spectrophotometry (UV-Vis) is a technique used to measure the structural and optical properties of a specimen. Electromagnetic radiation hits the specimen and the amount of light absorbed (or transmitted) by it is measured. The intensity of light that passes through a specimen regarding the intensity of light through a reference substrate or blank is measured.[270]

X-Ray Diffraction

The XRD measurement were obtained with using micro-X-ray diffraction (μ-XRD) measurements from a Bruker-AXS D8-Discover diffractometer equipped with a parallel incident beam (i.e., Göbel mirror), a vertical θ-θ goniometer, a XYZ motorized stage and with a general area diffraction system (GADDS).

X-Ray diffraction is a technique for characterizing crystalline materials. It provides information on structures, phases, preferred crystal orientations, etc. X-ray diffraction peaks are produced by constructive interference of a monochromatic beam of X-rays scattered at specific angles from each set of lattice planes in a substrate. The peak intensities are determined by the distribution of atoms within the lattice.[271]

Appendix 2. Thin-Film Deposition Techniques

There are several thin-film deposition techniques but only those used in this thesis are described. Drop-casting, spin-coating and thermal evaporation techniques were used for typical conventional flat and nanostructured PSCs devices manufacture.

Drop Casting

It is the most extensively used deposition technique due to the outstanding advantages such as the facile process and no requirement of specific equipment. It consists of a thin solid film formation by dropping a solution on a flat surface followed by the solvent evaporation. This technique is easy and fast.[272] In this thesis, the TiO_2 nanoparticles dispersions prepared for fabricating nPSCs devices were deposited *via* drop-casting.

Spin Coating

It is the standard technique of thin-films deposition from a solution. This technique yields films with relatively high uniformity and well-controlled thickness. The solution-processed material is dropped on a rotating substrate, where the centrifugal forces spread the solution on the whole substrate surface and the volatile solvent is simultaneously evaporated due to the speed spinning. [273] The thickness of the film highly depends on the concentration and viscosity of the solution, the volatility of solvent, and the angular speed of spinning.[274] In this thesis, the TiO_2, $MAPbI_3$ and spiro-OMeTAD layers for fabricating mesoporous PSCs and nPSCs devices were deposited *via* spin-coating with a Laurel WS-400B-6NPP/LITE and WS-650MZ-23NPP spin-coaters. The spin-coating depositions of SnO_2, CsFAMAPbIBr and spiro-OMeTAD layers for fabricating planar PSCs and nPSC devices were performed with Laurel WS-650MZ-8NPP. The perovskite film depositions were carried out using the spin-coating technique *via* the solution-processed single precursor and anti-solvent method.[275,276] First, a single perovskite precursor is deposited over a substrate and it is spin-coated. A solvent is poured onto the precursor perovskite film while the substrate is still spinning, causing the salts to precipitate out of solution into a smooth, compact film.[186,276] The most common solvents used are toluene, chlorobenzene, and diethyl ether. The use of anti-solvents enhances crystallinity and allows us to have better control of the perovskite morphology.[186]

Thermal Evaporation

It is a vacuum technology for thin-films deposition of pure solid materials such as metals, non-metals, oxides, nitrides, and organic materials. In thermal evaporation a high-current flow through a resistive evaporation source (so-called filament or boat) made of metals, commonly tungsten or molybdenum.[277] The evaporation source is located at the bottom of a vacuum chamber (1×10^{-9} bar), whereas the target (substrate) is held inverted on the top. The materials are heated to overcome their melting point and form a vapour stream which is deposited on the surface of the substrate. The vacuum chamber is located in a nitrogen-filled glove-box. In this thesis, silver (Ag), gold (Au) and tungsten trioxide (WO_3) layers were thermally evaporated under high vacuum in a thermal evaporator located in a Glove-box, model MB20/MB200 from MBRAUN.

References

[1] I. Capek, Nanotechnology and nanomaterials, Nanocomposite Struct. Dispersions. (2019) 1–93. https://doi.org/10.1016/b978-0-444-63748-2.00001-8.

[2] H. Asoh, S. Ono, Fabrication of Ordered Anodic Nanoporous Alumina Layers and their Application to Nanotechnology, Electrocrystallization Nanotechnol. (2007) 138–166. https://doi.org/10.1002/9783527610198.ch7.

[3] Z. Bojar, W.J. Stępniowski, Nanoporous Anodic Aluminum Oxide: Fabrication, Characterization, and Applications, in: M.A. Makhlouf, A.S. Hamdy (Eds.), Handb. Nanoelectrochemistry Electrochem. Synth. Methods, Prop. Charact. Tech., Springer International Publishing, Switzerland, 2016: pp. 593–646. https://doi.org/10.1007/978-3-319-15266-0.

[4] E. Xifre-Perez, J. Ferré-Borrull, J. Pallarès, L.F. Marsal, Micro- and nanoparticles of mesoporous anodic alumina: Morphological and physicochemical properties, Microporous Mesoporous Mater. 239 (2017) 363–370. https://doi.org/10.1016/j.micromeso.2016.10.034.

[5] P. Formentín, Ú. Catalán, L. Pol, S. Fernández-Castillejo, R. Solà, L.F. Marsal, Collagen and fibronectin surface modification of nanoporous anodic alumina and macroporous silicon for endothelial cell cultures, J. Biol. Eng. 12 (2018) 21. https://doi.org/10.1186/s13036-018-0111-x.

[6] C. Toccafondi, R. La Rocca, A. Scarpellini, M. Salerno, G. Das, S. Dante, Thin nanoporous alumina-based SERS platform for single cell sensing, Appl. Surf. Sci. 351 (2015) 738–745. https://doi.org/10.1016/j.apsusc.2015.05.169.

[7] K.C. Popat, K.-I. Chatvanichkul, G.L. Barnes, T.J. Latempa, C.A. Grimes, T.A. Desai, Osteogenic differentiation of marrow stromal cells cultured on nanoporous alumina surfaces, J. Biomed. Mater. Res. Part A. 80A (2007) 955–964. https://doi.org/10.1002/jbm.a.31028.

[8] L. Pol, C. Eckstein, L.K. Acosta, E. Xifr, J. Ferr, L.F. Marsal, Real-Time

Monitoring of Biotinylated Molecules Detection Dynamics in Nanoporous Anodic Alumina for Bio-Sensing, Nanomaterials. 9 (2019) 478–490. https://doi.org/10.3390/nano9030478.

[9] S.M. Aguilar-Sierra, J. Ferré-Borrull, F.E. Echeverría, L.F. Marsal, Titanium dioxide-coated nanoporous anodic alumina optical properties, Appl. Surf. Sci. 489 (2019) 239–246. https://doi.org/10.1016/j.apsusc.2019.05.290.

[10] L. Cantelli, J.S. Santos, F. Trivinho-Strixino, The effect of anodization temperature on optical properties of nanoporous anodic alumina (NAA) films, J. Electroanal. Chem. 780 (2016) 386–390. https://doi.org/10.1016/j.jelechem.2016.01.009.

[11] M. Porta-i-Batalla, C. Eckstein, E. Xifré-Pérez, P. Formentín, J. Ferré-Borrull, L.F. Marsal, Sustained, Controlled and Stimuli-Responsive Drug Release Systems Based on Nanoporous Anodic Alumina with Layer-by-Layer Polyelectrolyte, Nanoscale Res. Lett. 11 (2016). https://doi.org/10.1186/s11671-016-1585-4.

[12] M. Porta-i-Batalla, E. Xifré-Pérez, C. Eckstein, J. Ferré-Borrull, L. Marsal, 3D Nanoporous Anodic Alumina Structures for Sustained Drug Release, Nanomaterials. 7 (2017) 227. https://doi.org/10.3390/nano7080227.

[13] Q. Wei, Y. Fu, G. Zhang, D. Yang, G. Meng, S. Sun, Rational design of novel nanostructured arrays based on porous AAO templates for electrochemical energy storage and conversion, Nano Energy. 55 (2019) 234–259. https://doi.org/10.1016/j.nanoen.2018.10.070.

[14] G. Che, B.B. Lakshmi, E.R. Fisher, C.R. Martin, Carbon nanotubule membranes for electrochemical energy storage and production, Nature. 393 (1998) 346–349. https://doi.org/10.1038/30694.

[15] M. Ghrib, R. Ouertani, M. Gaidi, N. Khedher, M. Ben Salem, H. Ezzaouia, Effect of annealing on photoluminescence and optical properties of porous anodic alumina films formed in sulfuric acid for solar energy applications, Appl. Surf.

Sci. 258 (2012) 4995–5000. https://doi.org/10.1016/j.apsusc.2011.12.056.

[16] A.S. Aricò, P. Bruce, B. Scrosati, J.-M. Tarascon, W. van Schalkwijk, Nanostructured materials for advanced energy conversion and storage devices, Nat. Mater. 4 (2005) 366–377. https://doi.org/10.1038/nmat1368.

[17] World-energy-statistics, (2020). https://www.iea.org/reports/key-world-energy-statistics-2020.

[18] G. Kopp, J.L. Lean, A new, lower value of total solar irradiance: Evidence and climate significance, Geophys. Res. Lett. 38 (2011) 1–7. https://doi.org/10.1029/2010GL045777.

[19] L. Yue, B. Yan, M. Attridge, Z. Wang, Light absorption in perovskite solar cell: Fundamentals and plasmonic enhancement of infrared band absorption, Sol. Energy. 124 (2016) 143–152. https://doi.org/10.1016/j.solener.2015.11.028.

[20] O. Ergen, S.M. Gilbert, T. Pham, S.J. Turner, M.T.Z. Tan, M.A. Worsley, A. Zettl, Graded bandgap perovskite solar cells, Nat. Mater. 16 (2017) 522–525. https://doi.org/10.1038/nmat4795.

[21] B. Wang, K.Y. Wong, S. Yang, T. Chen, Crystallinity and defect state engineering in organo-lead halide perovskite for high-efficiency solar cells, J. Mater. Chem. A. 4 (2016) 3806–3812. https://doi.org/10.1039/c5ta09249c.

[22] S. Demchyshyn, J.M. Roemer, H. Groiß, H. Heilbrunner, C. Ulbricht, D. Apaydin, A. Böhm, U. Rütt, F. Bertram, G. Hesser, M.C. Scharber, N.S. Sariciftci, B. Nickel, S. Bauer, E.D. Głowacki, M. Kaltenbrunner, Confining metal-halide perovskites in nanoporous thin films, Sci. Adv. 3 (2017) 1–12. https://doi.org/10.1126/sciadv.1700738.

[23] “British Patent 223994 (1923),” “British Pat. 223994 (1923).” (n.d.). https://doi.org/10.1016/j.bios.2017.12.023.

[24] Italian Patent 741753 (1936), n.d.

[25] F. Keller, M.S. Hunter, D.L. Robinson, Structural Features of Oxide Coatings on Aluminum, J. Electrochem. Soc. 100 (1953) 411.

https://doi.org/10.1149/1.2781142.

[26] J.W. Diggle, T.C. Downie, C.W. Goulding, Anodic oxide films on aluminum, Chem. Rev. 69 (1969) 365–405. https://doi.org/10.1021/cr60259a005.

[27] G.E. Thompson, G.C. Wood, Porous anodic film formation on aluminium, Nature. 290 (1981) 230–232. https://doi.org/10.1038/290230a0.

[28] G.C. Wood, A Model for the Incorporation of Electrolyte Species into Anodic Alumina, J. Electrochem. Soc. 143 (1996) 74. https://doi.org/10.1149/1.1836389.

[29] O. Jessensky, F. Müller, U. Gösele, Self-organized formation of hexagonal pore arrays in anodic alumina, Appl. Phys. Lett. 72 (1998) 1173–1175. https://doi.org/10.1063/1.121004.

[30] G.D. Sulka, Highly Ordered Anodic Porous Alumina Formation by Self-Organized Anodizing, 2008. https://doi.org/10.1002/9783527621507.ch1.

[31] Ling Z., Li Y., Mechanisms of Nanoporous Alumina Formation and Self-organized Growth, in: D. Losic, A. Santos (Eds.), Nanoporous Alumina, Springer Series in Materials Science Springer, Cham, 2015. https://doi.org/10.1007/978-3-319-20334-8_1.

[32] H. Masuda, K. Fukuda, Ordered metal nanohole arrays made by a two-step replication of honeycomb structure of anodic alumina, Science (80-.). 268 (1995) 1466–1468. https://doi.org/10.1126/science.268.5216.1466.

[33] K. Nielsch, J. Choi, K. Schwirn, R.B. Wehrspohn, U. Gösele, Self-ordering Regimes of Porous Alumina: The 10 Porosity Rule, Nano Lett. 2 (2002) 677–680. https://doi.org/10.1021/nl025537k.

[34] W. Lee, J.-C. Kim, Highly ordered porous alumina with tailor-made pore structures fabricated by pulse anodization, Nanotechnology. 21 (2010) 485304. https://doi.org/10.1088/0957-4484/21/48/485304.

[35] P. Yan, G.T. Fei, G.L. Shang, B. Wu, L. De Zhang, Fabrication of one-dimensional alumina photonic crystals with a narrow band gap and their

application to high-sensitivity sensors, J. Mater. Chem. C. 1 (2013) 1659–1664. https://doi.org/10.1039/c2tc00396a.

[36] J. Ferré-Borrull, M.M. Rahman, J. Pallarès, L.F. Marsal, Tuning nanoporous anodic alumina distributed-Bragg reflectors with the number of anodization cycles and the anodization temperature, Nanoscale Res. Lett. 9 (2014) 1–6. https://doi.org/10.1186/1556-276X-9-416.

[37] J.P. O'Sullivan, G.C. Wood, Morphology and mechanism of formation of porous anodic films on aluminum, Proc Roy Soc Ser A Math Phys Sci. 317 (1970) 511–543. https://doi.org/10.1098/rspa.1970.0129.

[38] W. Lee, The anodization of aluminum for nanotechnology applications, JOM. 62 (2010) 57–63. https://doi.org/10.1007/s11837-010-0088-5.

[39] E. Davoodi, M. Zhianmanesh, H. Montazerian, A.S. Milani, M. Hoorfar, Nano-porous anodic alumina: fundamentals and applications in tissue engineering, J. Mater. Sci. Mater. Med. 31 (2020) 60. https://doi.org/10.1007/s10856-020-06398-2.

[40] R. Palacios, P. Formentín, A. Santos, E. Martínez-Ferrero, J. Ferré-Borrull, J. Pallarès, L.F. Marsal, Template-assisted fabrication and characterization of photoluminescent polymer nanopillars, Phys. Status Solidi Curr. Top. Solid State Phys. 8 (2011) 2612–2616. https://doi.org/10.1002/pssc.201084122.

[41] E.C.S. Transactions, T.E. Society, Synthesis and Characterization of Photoluminescence Polymer Nanopillar Arrays, ECS Meet. Abstr. 28 (2010) 105–113. https://doi.org/10.1149/ma2010-01/20/1088.

[42] J. Ferré-Borrull, E. Xifré-Pérez, J. Pallarès, L.F. Marsal, Optical Properties of Nanoporous Anodic Alumina and Derived Applications, in: D. Losic, A. Santos (Eds.), Nanoporous Alumina, Springer International Publishing, Cham, 2015: pp. 185–217. https://doi.org/10.1007/978-3-319-20334-8_6.

[43] R. Palacios, P. Formentín, J. Ferré-Borrull, J. Pallarés, L.F. Marsal, Polymer nanopillars using self-ordered nanoporous alumina templates, in: Phys.

Status Solidi Curr. Top. Solid State Phys., 2009: pp. 1584–1586. https://doi.org/10.1002/pssc.200881057.

[44] A. Santos, P. Formentin, J. Pallarés, J. Ferré-Borrull, L.F. Marsal, Quasi-ordered P3HT nanopillar-nanocap structures with controlled size, Mater. Lett. 64 (2010) 371–374. https://doi.org/10.1016/j.matlet.2009.11.020.

[45] V.S. Balderrama, J. Albero, P. Granero, J. Ferré-Borrull, J. Pallarés, E. Palomares, L.F. Marsal, Design, fabrication and charge recombination analysis of an interdigitated heterojunction nanomorphology in P3HT/PC70BM solar cells, Nanoscale. 7 (2015) 13848–13859. https://doi.org/10.1039/c5nr02429c.

[46] G. Sauer, G. Brehm, S. Schneider, K. Nielsch, R.B. Wehrspohn, J. Choi, H. Hofmeister, U. Gösele, Highly ordered monocrystalline silver nanowire arrays, J. Appl. Phys. 91 (2002) 3243–3247. https://doi.org/10.1063/1.1435830.

[47] G. Che, B.B. Lakshmi, E.R. Fisher, C.R. Martin, Carbon nanotubule membranes for electrochemical energy storage and production, Nature. 393 (1998) 346–349. https://doi.org/10.1038/30694.

[48] K.N. Hideki Masuda, Kenji Yasui, Fabrication of Ordered Arrays of MultipleNanodots Using Anodic Porous Alumina as an Evaporation Mask, Adv. Mater. 12 (2000) 1031–1033. https://doi.org/10.1002/1521-4095(200007)12:14<1031::AID-ADMA1031>3.0.CO;2-R.

[49] A.J. Goszczak, P.P. Cielecki, A Review on Anodic Aluminum Oxide Methods for Fabrication of Nanostructures for Organic Solar Cells, Curr. Nanosci. 15 (2018) 64–75. https://doi.org/10.2174/1573413714666180228152018.

[50] H. Asoh, K. Nishio, M. Nakao, T. Tamamura, H. Masuda, Conditions for fabrication of ideally ordered anodic porous alumina using pretextured Al, J. Electrochem. Soc. 148 (2001) B152. https://doi.org/10.1149/1.1355686.

[51] D. Gong, V. Yadavalli, M. Paulose, M. Pishko, C.A. Grimes, Controlled

molecular release using nanoporous alumina capsules, Biomed. Microdevices. 5 (2003) 75–80. https://doi.org/10.1023/A:1024471618380.

[52] Z. Huang, W. Zhang, J. Yu, D. Gao, Nanoporous alumina membranes for enhancing hemodialysis, 1 (2007) 79–83. https://doi.org/10.1115/1.2360949.

[53] Z. Fan, H. Razavi, J. Do, A. Moriwaki, O. Ergen, Y.-L. Chueh, P.W. Leu, J.C. Ho, T. Takahashi, L.A. Reichertz, Three-dimensional nanopillar-array photovoltaics on low-cost and flexible substrates, Nat. Mater. 8 (2009) 648–653. https://doi.org/10.1038/nmat2493.

[54] T. Hübert, L. Boon-Brett, G. Black, U. Banach, Hydrogen sensors–a review, Sensors Actuators B Chem. 157 (2011) 329–352. https://doi.org/10.1016/j.snb.2011.04.070.

[55] B. Sun, E. Marx, N.C. Greenham, Photovoltaic devices using blends of branched CdSe nanoparticles and conjugated polymers, Nano Lett. 3 (2003) 961–963. https://doi.org/10.1021/nl0342895.

[56] Z. Yu, L. Tetard, L. Zhai, J. Thomas, Supercapacitor electrode materials: Nanostructures from 0 to 3 dimensions, Energy Environ. Sci. 8 (2015) 702–730. https://doi.org/10.1039/c4ee03229b.

[57] Z. Chang, J. Xu, X. Zhang, Recent progress in electrocatalyst for Li-O 2 batteries, Adv. Energy Mater. 7 (2017) 1–21. https://doi.org/10.1002/aenm.201700875.

[58] P. Granero, V.S. Balderrama, J. Ferré-Borrull, J. Pallarès, L.F. Marsal, Two-dimensional finite-element modeling of periodical interdigitated full organic solar cells, J. Appl. Phys. 113 (2013). https://doi.org/10.1063/1.4788819.

[59] P. Granero, V.S. Balderrama, J. Ferré-Borrull, J. Pallarès, L.F. Marsal, Light absorption modeling of ordered bulk heterojunction organic solar cells, Curr. Appl. Phys. 13 (2013) 1801–1807. https://doi.org/10.1016/j.cap.2013.07.016.

[60] P. Liu, V.P. Singh, C.A. Jarro, S. Rajaputra, Cadmium sulfide nanowires for the window semiconductor layer in thin film CdS-CdTe solar cells., Nanotechnology. 22 (2011) 145304. https://doi.org/10.1088/0957-4484/22/14/145304.

[61] M.M. Lee, J. Teuscher, T. Miyasaka, T.N. Murakami, H.J. Snaith, Efficient hybrid solar cells based on meso-superstructured organometal halide perovskites., Science. 338 (2012) 643–647. https://doi.org/10.1126/science.1228604.

[62] J. Oh, H.-C. Yuan, H.M. Branz, An 18.2%-efficient black-silicon solar cell achieved through control of carrier recombination in nanostructures., Nat. Nanotechnol. 7 (2012) 743–748. https://doi.org/10.1038/nnano.2012.166.

[63] Narottam Das, Introduction of Nano-Structured Solar Cells, in: N. Das (Ed.), Nanostructured Sol. Cells, IntechOpen, Rijeka, 2017. https://doi.org/10.5772/67467.

[64] F. Li, L. Zhang, R.M. Metzger, On the Growth of Highly Ordered Pores in Anodized Aluminum Oxide, Electrochim. Acta. 10 (1998) 2470–2480. https://doi.org/10.1021/cm980163a.

[65] W. Lee, R. Ji, U. Gösele, K. Nielsch, Fast fabrication of long-range ordered porous alumina membranes by hard anodization, Nat. Mater. 5 (2006) 741–747. https://doi.org/10.1038/nmat1717.

[66] K. Nielsch, J. Choi, K. Schwirn, R.B. Wehrspohn, U. Gösele, Self-ordering Regimes of Porous Alumina: The 10% Porosity Rule, Nano Lett. 2 (2002) 1–4. https://doi.org/10.1021/nl025537k.

[67] G.E. Thompson, G.C. Wood, Anodic films on aluminium, in: J.C. SCULLY (Ed.), Corros. Aqueous Process. Passiv. Film., 1983: pp. 205–329. https://doi.org/10.1016/B978-0-12-633670-2.50010-3.

[68] H. Han, S.J. Park, J.S. Jang, H. Ryu, K.J. Kim, S. Baik, W. Lee, In situ determination of the pore opening point during wet-chemical etching of the

barrier layer of porous anodic aluminum oxide: Nonuniform Impurity Distribution in Anodic Oxide, ACS Appl. Mater. Interfaces. 5 (2013) 3441–3448. https://doi.org/10.1021/am400520d.

[69] A. Mozalev, S. Magaino, H. Imai, The formation of nanoporous membranes from anodically oxidized aluminium and their application to Li rechargeable batteries, Electrochim. Acta. 46 (2001) 2825–2834. https://doi.org/10.1016/S0013-4686(01)00497-2.

[70] W. Lee, S.-J. Park, Porous Anodic Aluminum Oxide: Anodization and Templated Synthesis of Functional Nanostructures, Chem. Rev. 114 (2014) 7487–7556. https://doi.org/10.1021/cr500002z.

[71] C. Cheng, A.H.W. Ngan, Theoretical Pore Growth Models for Nanoporous Alumina, in: D. Losic, A. Santos (Eds.), Nanoporous Alumina Fabr. Struct. Prop. Appl., Springer Series in Materials Science, 2015: pp. 31–60. https://doi.org/10.1007/978-3-319-20334-8_2.

[72] G.E. Thompson, Porous anodic alumina: Fabrication, characterization and applications, Thin Solid Films. 297 (1997) 192–201. https://doi.org/10.1016/S0040-6090(96)09440-0.

[73] F. Davies, J. A.; Domeij, B.; Pringle, J. P.; Brown, The migration of metal and oxygen during anodic film formation, Electrochem. Soc. 112 (1965) 670–680.

[74] J.A. Davies, J.P.S. Pringle, R.L. Graham, F. Brown, A Radiotracer Study of Anodic Oxidation, J. Electrochem. Soc. 109 (1962) 99. https://doi.org/10.1149/1.2423662.

[75] K. Shimizu, G. Thompson, G. Wood, Y. Xu, Direct observations of ion-implanted Xenon marker layers in anodic barrier films on aluminum, Thin Solid Films. 88 (1982) 255–262.

[76] F. Brown, W.D. Mackintosh, The Use of Rutherford Backscattering to Study the Behavior of Ion-Implanted Atoms During Anodic Oxidation of Aluminum: Ar, Kr, Xe, K, Rb, Cs, Cl, Br, and I, J. Electrochem. Soc. 120 (1973) 1096.

https://doi.org/10.1149/1.2403637.

[77] S.Ikonopisov, A.Girginov, M.Machkova, Post-breakdown anodization of aluminium, Electrochem. Soc. 22 (1977) 1283–1286. https://doi.org/10.1016/0013-4686(77)87011-4.

[78] J.M. Albella, Electron Injection and Avalanche during the Anodic Oxidation of Tantalum, J. Electrochem. Soc. 131 (1984) 1101. https://doi.org/10.1149/1.2115758.

[79] S.Z. Chu, K. Wada, S. Inoue, M. Isogai, Y. Katsuta, A. Yasumori, Large-Scale Fabrication of Ordered Nanoporous Alumina Films with Arbitrary Pore Intervals by Critical-Potential Anodization, J. Electrochem. Soc. 153 (2006) B384. https://doi.org/10.1149/1.2218822.

[80] J. Ferré-Borrull, J. Pallarès, G. Macías, L.F. Marsal, Nanostructural engineering of nanoporous anodic alumina for biosensing applications, Materials (Basel). 7 (2014) 5225–5253. https://doi.org/10.3390/ma7075225.

[81] H. Takahashi, M. Nagayama, The determination of the porosity of anodic oxide films on aluminium by the pore-filling method, Corros. Sci. 18 (1978) 911–925. https://doi.org/10.1016/1010-938x(78)90012-4.

[82] R.C. Alkire, Y. Gogotsi, P. Simon, Nanostructured materials in electrochemistry, John Wiley & Sons, 2008. https://doi.org/10.1002 / 9783527621507.

[83] H. Takahashi, M. Nagayama, The determination of the porosity of anodic oxidfe films on aluminium by the pore-filling method, Corros. Sci. 18 (1978) 911–925.

[84] L. Zaraska, G.D. Sulka, M. Jaskuła, Anodic alumina membranes with defined pore diameters and thicknesses obtained by adjusting the anodizing duration and pore opening/widening time, J. Solid State Electrochem. 15 (2011) 2427–2436. https://doi.org/10.1007/s10008-011-1471-z.

[85] A. Santos, P. Formentín, J. Pallarès, J. Ferré-Borrull, L.F. Marsal, Structural

engineering of nanoporous anodic alumina funnels with high aspect ratio, J. Electroanal. Chem. 655 (2011) 73–78. https://doi.org/10.1016/j.jelechem.2011.02.005.

[86] S. GD, P. KG, Temperature influence on well-ordered nanopore structures grown by anodization of aluminium in sulphuric acid, Electrochim. Acta. 52 (2007) 1880–1888. https://doi.org/10.1016/j.electacta.2006.07.053.

[87] H. Masuda, H. Yamada, M. Satoh, H. Asoh, M. Nakao, T. Tamamura, Highly ordered nanochannel-array architecture in anodic alumina, Appl. Phys. Lett. 71 (1997) 2770–2772. https://doi.org/10.1063/1.120128.

[88] A.P. Li, F. Müller, A. Bimer, K. Nielsch, U. Gösele, Hexagonal pore arrays with a 50-420 nm interpore distance formed by self-organization in anodic alumina, J. Appl. Phys. 84 (1998) 6023–6026. https://doi.org/10.1063/1.368911.

[89] Kikuchi, Tatsuya, Nishinaga, Osamu, Natsui, Shungo, Suzuki, R. O., Self-Ordering Behavior of Anodic Porous Alumina via Selenic Acid Anodizing, Electrochim. Acta. 137 (2014) 728–735. https://doi.org/10.1016/j.electacta.2014.06.078.

[90] T. Aerts, J.B. Jorcin, I. De Graeve, H. Terryn, Comparison between the influence of applied electrode and electrolyte temperatures on porous anodizing of aluminium, Electrochim. Acta. 55 (2010) 3957–3965. https://doi.org/10.1016/j.electacta.2010.02.044.

[91] I. Vrublevsky, V. Parkoun, V. Sokol, J. Schreckenbach, Study of chemical dissolution of the barrier oxide layer of porous alumina films formed in oxalic acid using a re-anodizing technique, Appl. Surf. Sci. 236 (2004) 270–277. https://doi.org/10.1016/j.apsusc.2004.04.030.

[92] I. Vrublevsky, V. Parkoun, V. Sokol, J. Schreckenbach, G. Marx, The study of the volume expansion of aluminum during porous oxide formation at galvanostatic regime, Appl. Surf. Sci. 222 (2004) 215–225.

https://doi.org/10.1016/j.apsusc.2003.08.014.

[93] A.L. Friedman, D. Brittain, L. Menon, Roles of pH and acid type in the anodic growth of porous alumina., J. Chem. Phys. 127 (2007) 154717. https://doi.org/10.1063/1.2790429.

[94] M.M. Rahman, E. Garcia-Caurel, A. Santos, L.F. Marsal, J. Pallarès, J. Ferré-Borrull, Effect of the anodization voltage on the pore-widening rate of nanoporous anodic alumina, Nanoscale Res. Lett. 7 (2012) 1–7. https://doi.org/10.1186/1556-276X-7-474.

[95] F. Bertó-Roselló, E. Xifré-Pérez, J. Ferré-Borrull, J. Pallarès, L.F. Marsal, Nanoporous Anodic Alumina 3D FDTD Modelling for a Broad Range of Inter-pore Distances, Nanoscale Res. Lett. 11 (2016). https://doi.org/10.1186/s11671-016-1575-6.

[96] P. Hersch, K. Zweibel, Basic photovoltaic principles and methods, United States, 1982. https://doi.org/10.2172/5191389.

[97] A. E. Becquerel, Recherches sur les effets de la radiation chimique de la lumiere solaire au moyen des courants electriques, Comptes Rendus L'Academie Des Sci. 9 (1839) 145–149.

[98] C.E. Fritts, On the fritts selenium cells and batteries, J. Franklin Inst. 119 (1885) 221–232. https://doi.org/10.1016/0016-0032(85)90426-0.

[99] A. Einstein, Concerning an heuristic point of view toward the emission and transformation of light, Am. J. Phys. 33 (1905) 367. https://doi.org/10.1119/1.1971542.

[100] Edwin F. Kingsbury, Russell S. Ohl, Photoelectric Properties of Ionically Bombarded Silicon, Bell Syst. Tech. J. 31 (1952) 802–815. https://doi.org/10.1002/j.1538-7305.1952.tb01407.x.

[101] D.M. Chapin, C.S. Fuller, G.L. Pearson, A new silicon pn junction photocell for converting solar radiation into electrical power, J. Appl. Phys. 25(5) (1954) 676–677. https://doi.org/10.1063/1.1721711.

[102] B.M. Kayes, H. Nie, R. Twist, S.G. Spruytte, F. Reinhardt, I.C. Kizilyalli, G.S. Higashi, 27.6% conversion efficiency, a new record for single-junction solar cells under 1 sun illumination, in: 2011 37th IEEE Photovolt. Spec. Conf., IEEE, 2011: pp. 4–8. https://doi.org/10.1109/PVSC.2011.6185831.

[103] M. Nakamura, K. Yamaguchi, Y. Kimoto, Y. Yasaki, T. Kato, H. Sugimoto, Cd-Free Cu(In,Ga)(Se,S)2 Thin-Film Solar Cell With Record Efficiency of 23.35%, IEEE J. Photovoltaics. 9 (2019) 1863–1867. https://doi.org/10.1109/JPHOTOV.2019.2937218.

[104] Q. Liu, Y. Jiang, K. Jin, J. Qin, J. Xu, W. Li, J. Xiong, J. Liu, Z. Xiao, K. Sun, S. Yang, X. Zhang, L. Ding, 18% Efficiency organic solar cells, Sci. Bull. 65 (2020) 272–275. https://doi.org/10.1016/j.scib.2020.01.001.

[105] M. Hao, Y. Bai, S. Zeiske, L. Ren, J. Liu, Y. Yuan, N. Zarrabi, N. Cheng, M. Ghasemi, P. Chen, M. Lyu, D. He, J.-H. Yun, Y. Du, Y. Wang, S. Ding, A. Armin, P. Meredith, G. Liu, H.-M. Cheng, L. Wang, Ligand-assisted cation-exchange engineering for high-efficiency colloidal Cs1−xFAxPbI3 quantum dot solar cells with reduced phase segregation, Nat. Energy. 5 (2020) 79–88. https://doi.org/10.1038/s41560-019-0535-7.

[106] K.-J. Yang, D.-H. Son, S.-J. Sung, J.-H. Sim, Y.-I. Kim, S.-N. Park, D.-H. Jeon, J. Kim, D.-K. Hwang, C.-W. Jeon, A band-gap-graded CZTSSe solar cell with 12.3% efficiency, J. Mater. Chem. A. 4 (2016) 10151–10158. https://doi.org/10.1039/C6TA01558A.

[107] Best Research-Cell Efficiency Chart (NREL), (2020). https://www.nrel.gov/pv/cell-efficiency.html.

[108] J.F. Geisz, R.M. France, K.L. Schulte, M.A. Steiner, A.G. Norman, H.L. Guthrey, M.R. Young, T. Song, T. Moriarty, Six-junction III–V solar cells with 47.1% conversion efficiency under 143 Suns concentration, Nat. Energy. 5 (2020) 326–335. https://doi.org/10.1038/s41560-020-0598-5.

[109] M.A. Green, A. Ho-Baillie, H.J. Snaith, The emergence of perovskite solar cells,

Nat. Photonics. 8 (2014) 506–514. https://doi.org/10.1038/nphoton.2014.134.

[110] M. Grätzel, The light and shade of perovskite solar cells, Nat. Mater. 13 (2014) 838–842. https://doi.org/10.1038/nmat4065.

[111] T.J. Jacobsson, J.-P. Correa-Baena, M. Pazoki, M. Saliba, K. Schenk, M. Grätzel, A. Hagfeldt, Exploration of the compositional space for mixed lead halogen perovskites for high efficiency solar cells, Energy Environ. Sci. 9 (2016) 1706–1724. https://doi.org/10.1039/c6ee00030d.

[112] N.G. Park, Perovskite solar cells: An emerging photovoltaic technology, Mater. Today. 18 (2015) 65–72. https://doi.org/10.1016/j.mattod.2014.07.007.

[113] A.R. Chakhmouradian, P.M. Woodward, Celebrating 175 years of perovskite research: A tribute to Roger H. Mitchell, Phys. Chem. Miner. 41 (2014) 387–391. https://doi.org/10.1007/s00269-014-0678-9.

[114] S. Sasaki, C.T. Prewitt, J.D. Bass, W. Schulze, Orthorhombic perovskite CaTiO3 and CdTiO3: structure and space group, Acta Crystallogr. 43 (1987) 1668–1674.

[115] J. Yan, B.R. Saunders, Third-generation solar cells: a review and comparison of polymer:fullerene, hybrid polymer and perovskite solar cells, RSC Adv. 4 (2014) 43286–43314. https://doi.org/10.1039/C4RA07064J.

[116] Z. Shi, A.H. Jayatissa, Perovskites-based solar cells: A review of recent progress, materials and processing methods, Materials (Basel). 11 (2018). https://doi.org/10.3390/ma11050729.

[117] Q. Chen, N. De Marco, Y. Yang, T. Bin Song, C.C. Chen, H. Zhao, Z. Hong, H. Zhou, Y. Yang, Under the spotlight: The organic-inorganic hybrid halide perovskite for optoelectronic applications, Nano Today. 10 (2015) 355–396. https://doi.org/10.1016/j.nantod.2015.04.009.

[118] K. Qin, B. Dong, S. Wang, Improving the stability of metal halide perovskite

solar cells from material to structure, J. Energy Chem. 33 (2019) 90–99. https://doi.org/https://doi.org/10.1016/j.jechem.2018.08.004.

[119] J.-P. Correa-Baena, M. Saliba, T. Buonassisi, M. Grätzel, A. Abate, W. Tress, A. Hagfeldt, Promises and challenges of perovskite solar cells, Science (80-.). 358 (2017) 739 LP – 744. https://doi.org/10.1126/science.aam6323.

[120] S. Il Seok, M. Grätzel, N.-G. Park, Methodologies toward Highly Efficient Perovskite Solar Cells, Small. 14 (2018) 1704177. https://doi.org/10.1002/smll.201704177.

[121] A. Kojima, K. Teshima, T. Miyasaka, Y. Shirai, Novel Photoelectrochemical Cell with Mesoscopic Electrodes Sensitized by Lead-Halide Compounds, in: Proc. 210th ECS Meet., 2006.

[122] M. Jeong, I.W. Choi, E.M. Go, Y. Cho, M. Kim, B. Lee, S. Jeong, Y. Jo, H.W. Choi, J. Lee, Stable perovskite solar cells with efficiency exceeding 24.8% and 0.3-V voltage loss, Science (80-.). 369 (2020) 1615–1620. https://doi.org/10.1126/science.abb7167.

[123] B. O'Regan, M. Grätzel, A low-cost, high-efficiency solar cell based on dye-sensitized colloidal TiO2 films, Nature. 353 (1991) 737–740. https://doi.org/10.1038/353737a0.

[124] A. Kojima, K. Teshima, Y. Shirai, T. Miyasaka, Organometal Halide Perovskites as Visible-Light Sensitizers for Photovoltaic Cells, J. Am. Chem. Soc. 131 (2009) 6050–6051. https://doi.org/10.1021/ja809598r.

[125] J.H. Im, C.R. Lee, J.W. Lee, S.W. Park, N.G. Park, 6.5% Efficient Perovskite Quantum-Dot-Sensitized Solar Cell, Nanoscale. 3 (2011) 4088–4093. https://doi.org/10.1039/c1nr10867k.

[126] H.S. Kim, C.R. Lee, J.H. Im, K.B. Lee, T. Moehl, A. Marchioro, S.J. Moon, R. Humphry-Baker, J.H. Yum, J.E. Moser, M. Grätzel, N.G. Park, Lead iodide perovskite sensitized all-solid-state submicron thin film mesoscopic solar cell with efficiency exceeding 9%, Sci. Rep. 2 (2012) 1–7.

https://doi.org/10.1038/srep00591.

[127] Michael M. Lee, J. Teuscher, T. Miyasaka, T.N. Murakami, Henry J. Snaith, Efficient Hybrid Solar Cells Based on Meso-Superstructured Organometal Halide Perovskites, Science (80-.). 338 (2012) 643–647. https://doi.org/10.1126/science.1228604.

[128] J.H. Noh, S.H. Im, J.H. Heo, T.N. Mandal, S. Il Seok, Chemical management for colorful, efficient, and stable inorganic–organic hybrid nanostructured solar cells, Nano Lett. 13 (2013) 1764–1769. https://doi.org/10.1021/nl400349b.

[129] M. Liu, M.B. Johnston, H.J. Snaith, Efficient planar heterojunction perovskite solar cells by vapour deposition, Nature. 501 (2013) 395–398. https://doi.org/10.1038/nature12509.

[130] N. Pellet, P. Gao, G. Gregori, T.Y. Yang, M.K. Nazeeruddin, J. Maier, M. Grätzel, Mixed-organic-cation perovskite photovoltaics for enhanced solar-light harvesting, Angew. Chemie - Int. Ed. 53 (2014) 3151–3157. https://doi.org/10.1002/anie.201309361.

[131] J.P. Correa Baena, L. Steier, W. Tress, M. Saliba, S. Neutzner, T. Matsui, F. Giordano, T.J. Jacobsson, A.R. Srimath Kandada, S.M. Zakeeruddin, A. Petrozza, A. Abate, M.K. Nazeeruddin, M. Grätzel, A. Hagfeldt, Highly efficient planar perovskite solar cells through band alignment engineering, Energy Environ. Sci. 8 (2015) 2928–2934. https://doi.org/10.1039/c5ee02608c.

[132] M. Saliba, T. Matsui, J.Y. Seo, K. Domanski, J.P. Correa-Baena, M.K. Nazeeruddin, S.M. Zakeeruddin, W. Tress, A. Abate, A. Hagfeldt, M. Grätzel, Cesium-containing triple cation perovskite solar cells: Improved stability, reproducibility and high efficiency, Energy Environ. Sci. 9 (2016) 1989–1997. https://doi.org/10.1039/c5ee03874j.

[133] Best Research-Cell Efficiency Chart (NREL), (2018). https://www.nrel.gov/pv/assets/images/efficiency-chart.png.

[134] G. Li, K.L. Ching, J.Y.L. Ho, M. Wong, H.-S. Kwok, Overcoming the Limitations

of Sputtered Nickel Oxide for High-Efficiency and Large-Area Perovskite Solar Cells, Adv. Energy Mater. 4 (2017) 1700463–1700463. https://doi.org/10.1002/advs.201700463.

[135] J.-H. Im, I.-H. Jang, N. Pellet, M. Grätzel, N.-G. Park, Growth of CH3NH3PbI3 cuboids with controlled size for high-efficiency perovskite solar cells., Nat. Nanotechnol. 9 (2014) 927–932. https://doi.org/10.1038/nnano.2014.181.

[136] N.J. Jeon, J.H. Noh, W.S. Yang, Y.C. Kim, S. Ryu, J. Seo, S. Il Seok, Compositional engineering of perovskite materials for high-performance solar cells., Nature. 517 (2015) 476–480. https://doi.org/10.1038/nature14133.

[137] N.J. Jeon, J.H. Noh, Y.C. Kim, W.S. Yang, S. Ryu, S. Il Seok, Solvent engineering for high-performance inorganic-organic hybrid perovskite solar cells, Nat. Mater. 13 (2014) 897–903. https://doi.org/10.1038/nmat4014.

[138] A. Dualeh, T. Moehl, N. Tétreault, J. Teuscher, P. Gao, M.K. Nazeeruddin, M. Grätzel, Impedance Spectroscopic Analysis of Lead Iodide Perovskite-Sensitized Solid-State Solar Cells, ACS Nano. 8 (2014) 362–373. https://doi.org/10.1021/nn404323g.

[139] N. Ahn, D.-Y. Son, I.-H. Jang, S.M. Kang, M. Choi, N.-G. Park, Highly Reproducible Perovskite Solar Cells with Average Efficiency of 18.3% and Best Efficiency of 19.7% Fabricated via Lewis Base Adduct of Lead(II) Iodide., J. Am. Chem. Soc. 137 (2015) 8696–8699. https://doi.org/10.1021/jacs.5b04930.

[140] F. Hao, C.C. Stoumpos, Z. Liu, R.P.H. Chang, M.G. Kanatzidis, Controllable Perovskite Crystallization at a Gas–Solid Interface for Hole Conductor-Free Solar Cells with Steady Power Conversion Efficiency over 10%, J. Am. Chem. Soc. 136 (2014) 16411–16419. https://doi.org/10.1021/ja509245x.

[141] D. Shen, X. Yu, X. Cai, M. Peng, Y. Ma, X. Su, L. Xiao, D. Zou, Understanding the solvent-assisted crystallization mechanism inherent in efficient organic–inorganic halide perovskite solar cells, J. Mater. Chem. A. 2 (2014) 20454–20461. https://doi.org/10.1039/C4TA05635C.

[142] K.W. Tan, D.T. Moore, M. Saliba, H. Sai, L.A. Estroff, T. Hanrath, H.J. Snaith, U. Wiesner, Thermally Induced Structural Evolution and Performance of Mesoporous Block Copolymer-Directed Alumina Perovskite Solar Cells, ACS Nano. 8 (2014) 4730–4739. https://doi.org/10.1021/nn500526t.

[143] D.T. Moore, H. Sai, K.W. Tan, D.-M. Smilgies, W. Zhang, H.J. Snaith, U. Wiesner, L.A. Estroff, Crystallization Kinetics of Organic–Inorganic Trihalide Perovskites and the Role of the Lead Anion in Crystal Growth, J. Am. Chem. Soc. 137 (2015) 2350–2358. https://doi.org/10.1021/ja512117e.

[144] A. Schreiber, I. Ketelsen, G.H. Findenegg, Melting and freezing of water in ordered mesoporous silica materials, Phys. Chem. Chem. Phys. 3 (2001) 1185–1195. https://doi.org/10.1039/B010086M.

[145] Q. Jiang, M.D. Ward, Crystallization under nanoscale confinement, Chem. Soc. Rev. 43 (2014) 2066–2079. https://doi.org/10.1039/C3CS60234F.

[146] G.T. Rengarajan, D. Enke, M. Steinhart, M. Beiner, Size-dependent growth of polymorphs in nanopores and Ostwald's step rule of stages., Phys. Chem. Chem. Phys. 13 (2011) 21367–21374. https://doi.org/10.1039/c1cp22679g.

[147] J. Rzayev, M.A. Hillmyer, Nanochannel Array Plastics with Tailored Surface Chemistry, J. Am. Chem. Soc. 127 (2005) 13373–13379. https://doi.org/10.1021/ja053731d.

[148] B.D. Hamilton, J.-M. Ha, M.A. Hillmyer, M.D. Ward, Manipulating crystal growth and polymorphism by confinement in nanoscale crystallization chambers., Acc. Chem. Res. 45 (2012) 414–423. https://doi.org/10.1021/ar200147v.

[149] A. Henschel, P. Kumar, T. Hofmann, K. Knorr, P. Huber, Preferred orientation of n -hexane crystallized in silicon nanochannels: A combined x-ray diffraction and sorption isotherm study., Phys. Rev. E. Stat. Nonlin. Soft Matter Phys. 79 (2009) 32601. https://doi.org/10.1103/PhysRevE.79.032601.

[150] D. Ramirez, K. Schutt, J.F. Montoya, S. Mesa, J. Lim, H.J. Snaith, F. Jaramillo, Meso-Superstructured Perovskite Solar Cells: Revealing the Role of the Mesoporous Layer, J. Phys. Chem. C. 122 (2018) 21239–21247. https://doi.org/10.1021/acs.jpcc.8b07124.

[151] D. Ramirez, E. Velilla, J.F. Montoya, F. Jaramillo, Mitigating scalability issues of perovskite photovoltaic technology through a p-i-n meso-superstructured solar cell architecture, Sol. Energy Mater. Sol. Cells. 195 (2019) 191–197. https://doi.org/10.1016/j.solmat.2019.03.014.

[152] H.J. Snaith, A. Abate, J.M. Ball, G.E. Eperon, T. Leijtens, N.K. Noel, S.D. Stranks, J.T.-W. Wang, K. Wojciechowski, W. Zhang, Anomalous hysteresis in perovskite solar cells, J. Phys. Chem. Lett. 5 (2014) 1511–1515. https://doi.org/org/10.1021/jz500113x.

[153] J. Wei, Y. Zhao, H. Li, G. Li, J. Pan, D. Xu, Q. Zhao, D. Yu, Hysteresis analysis based on the ferroelectric effect in hybrid perovskite solar cells, J. Phys. Chem. Lett. 5 (2014) 3937–3945. https://doi.org/10.1021/jz502111u.

[154] H.W. Chen, N. Sakai, M. Ikegami, T. Miyasaka, Emergence of hysteresis and transient ferroelectric response in organo-lead halide perovskite solar cells, J. Phys. Chem. Lett. 6 (2015) 164–169. https://doi.org/10.1021/jz502429u.

[155] C. Eames, J.M. Frost, P.R.F. Barnes, B.C. O'Regan, A. Walsh, M.S. Islam, Ionic transport in hybrid lead iodide perovskite solar cells, Nat. Commun. 6 (2015) 7497. https://doi.org/10.1038/ncomms8497.

[156] S. Meloni, T. Moehl, W. Tress, M. Franckevičius, M. Saliba, Y.H. Lee, P. Gao, M.K. Nazeeruddin, S.M. Zakeeruddin, U. Rothlisberger, M. Graetzel, Ionic polarization-induced current-voltage hysteresis in CH3NH3PbX3 perovskite solar cells., Nat. Commun. 7 (2016) 10334. https://doi.org/10.1038/ncomms10334.

[157] P. Calado, A.M. Telford, D. Bryant, X. Li, J. Nelson, B.C. O'Regan, P.R.F. Barnes, Evidence for ion migration in hybrid perovskite solar cells with minimal

hysteresis, Nat. Commun. 7 (2016) 13831. https://doi.org/10.1038/ncomms13831.

[158] C. Li, S. Tscheuschner, F. Paulus, P.E. Hopkinson, J. Kießling, A. Köhler, Y. Vaynzof, S. Huettner, Iodine Migration and its Effect on Hysteresis in Perovskite Solar Cells, Adv. Mater. 28 (2016) 2446–2454. https://doi.org/10.1002/adma.201503832.

[159] H.J. Snaith, Perovskites: The emergence of a new era for low-cost, high-efficiency solar cells, J. Phys. Chem. Lett. 4 (2013). https://doi.org/10.1021/jz4020162.

[160] K. Zhu, T. Miyasaka, J.Y. Kim, I. Mora-Seró, Trend of Perovskite Solar Cells: Dig Deeper to Build Higher, J. Phys. Chem. Lett. 6 (2015) 2315–2317. https://doi.org/10.1021/acs.jpclett.5b01033.

[161] J.A. Luceño-Sánchez, A.M. Díez-Pascual, R.P. Capilla, Materials for photovoltaics: State of art and recent developments, Int. J. Mol. Sci. 20 (2019). https://doi.org/10.3390/ijms20040976.

[162] T.C. Sum, N. Mathews, Advancements in perovskite solar cells: Photophysics behind the photovoltaics, Energy Environ. Sci. 7 (2014) 2518–2534. https://doi.org/10.1039/c4ee00673a.

[163] A. Miyata, A. Mitioglu, P. Plochocka, O. Portugall, J.T.-W. Wang, S.D. Stranks, H.J. Snaith, R.J. Nicholas, Direct measurement of the exciton binding energy and effective masses for charge carriers in organic–inorganic tri-halide perovskites, Nat. Phys. 11 (2015) 582–587. https://doi.org/10.1038/nphys3357.

[164] M. F.M. Firdaus, C.H.Teh, R.Daik, E. l. Lim, C.C. Yap, I.M. Adib, A. L. Norasikin, M.Y.A.R. Bin, J. Jang, A.M.T. Mohd, The architecture of the electron transport layer for a perovskite solar cell, J. Mater. Chem. C. 6 (2018) 682–712. https://doi.org/10.1039/c7tc04649a.

[165] S. Emami, L. Andrade, A. Mendes, Recent progress in long-term stability of

perovskite solar cells, U.Porto J. Eng. 1 (2015) 52–62. https://doi.org/10.24840/2183-6493_001.002_0007.

[166] G.J. Meyer, The 2010 millennium technology grand prize: dye-sensitized solar cells, (2010) 4337–4343. https://doi.org/10.1021/nn101591h.

[167] N. Islam, M. Yang, K. Zhu, Z. Fan, Mesoporous scaffolds based on TiO2 nanorods and nanoparticles for efficient hybrid perovskite solar cells, J. Mater. Chem. A. 3 (2015) 24315–24321. https://doi.org/10.1039/c5ta06727h.

[168] S.K. Balasingam, M.G. Kang, Y. Jun, Metal substrate based electrodes for flexible dye-sensitized solar cells: fabrication methods, progress and challenges, Chem. Commun. 49 (2013) 11457–11475. https://doi.org/10.1039/C3CC46224B.

[169] F. Brunetti, A. Operamolla, S. Castro-Hermosa, G. Lucarelli, V. Manca, G.M. Farinola, T.M. Brown, Printed Solar Cells and Energy Storage Devices on Paper Substrates, Adv. Funct. Mater. 29 (2019). https://doi.org/10.1002/adfm.201806798.

[170] Z. Li, H. Li, L. Chen, J. Huang, W. Wang, H. Wang, J. Li, B. Fan, Q. Xu, W. Song, Semitransparent perovskite solar cells with ultrathin silver electrodes for tandem solar cells, Sol. Energy. 206 (2020) 294–300. https://doi.org/10.1016/j.solener.2020.06.013.

[171] M. Morales-Masis, S. De Wolf, R. Woods-Robinson, J.W. Ager, C. Ballif, Transparent Electrodes for Efficient Optoelectronics, Adv. Electron. Mater. 3 (2017). https://doi.org/10.1002/aelm.201600529.

[172] K.A. Bush, A.F. Palmstrom, Z.J. Yu, M. Boccard, R. Cheacharoen, J.P. Mailoa, D.P. McMeekin, R.L.Z. Hoye, C.D. Bailie, T. Leijtens, I.M. Peters, M.C. Minichetti, N. Rolston, R. Prasanna, S. Sofia, D. Harwood, W. Ma, F. Moghadam, H.J. Snaith, T. Buonassisi, Z.C. Holman, S.F. Bent, M.D. McGehee, 23.6%-Efficient Monolithic Perovskite/Silicon Tandem Solar Cells With

Improved Stability, Nat. Energy. 2 (2017). https://doi.org/10.1038/nenergy.2017.9.

[173] S. Zhu, X. Yao, Q. Ren, C.C. Zheng, S. Li, Y. Tong, B. Shi, S. Guo, L. Fan, H. Ren, C. Wei, B. Li, Y. Ding, Q. Huang, Y.L. Li, Y. Zhao, X. Zhang, Transparent electrode for monolithic perovskite/silicon-heterojunction two-terminal tandem solar cells, Nano Energy. 45 (2018) 280–286. https://doi.org/10.1016/j.nanoen.2017.12.043.

[174] J. Meyer, S. Hamwi, M. Kröger, W. Kowalsky, T. Riedl, A. Kahn, Transition metal oxides for organic electronics: Energetics, device physics and applications, Adv. Mater. 24 (2012) 5408–5427. https://doi.org/10.1002/adma.201201630.

[175] J.H. Han, D.H. Kim, E.G. Jeong, T.W. Lee, M.K. Lee, J.W. Park, H. Lee, K.C. Choi, Highly Conductive Transparent and Flexible Electrodes Including Double-Stacked Thin Metal Films for Transparent Flexible Electronics, ACS Appl. Mater. Interfaces. 9 (2017) 16343–16350. https://doi.org/10.1021/acsami.7b04725.

[176] M. Lee, Y. Jo, S. Kim, Y. Jun, Perovskite solar cells on metal substrate with high efficiency, J. Mater. Chem. A. (2015).

[177] L. Cattin, J.C. Bernède, M. Morsli, Toward indium-free optoelectronic devices: Dielectric/metal/dielectric alternative transparent conductive electrode in organic photovoltaic cells, Phys. Status Solidi Appl. Mater. Sci. 210 (2013) 1047–1061. https://doi.org/10.1002/pssa.201228089.

[178] X. Xie, C. Wu, S. Sun, X. Xu, W. Xu, G. Qin, L. Xiao, Semitransparent Perovskite Solar Cells with Dielectric/Metal/Dielectric Top Electrodes, Energy Technol. 8 (2020) 1–7. https://doi.org/10.1002/ente.201900868.

[179] J.H. Heo, D.H. Shin, M.L. Lee, M.G. Kang, S.H. Im, Efficient Organic-Inorganic Hybrid Flexible Perovskite Solar Cells Prepared by Lamination of Polytriarylamine/CH3NH3PbI3/Anodized Ti Metal Substrate and

Graphene/PDMS Transparent Electrode Substrate, ACS Appl. Mater. Interfaces. 10 (2018) 31413–31421. https://doi.org/10.1021/acsami.8b11411.

[180] N. Marinova, S. Valero, J.L. Delgado, Organic and perovskite solar cells: Working principles, materials and interfaces, J. Colloid Interface Sci. 488 (2017) 373–389. https://doi.org/10.1016/j.jcis.2016.11.021.

[181] T.-B. Song, Q. Chen, H. Zhou, C. Jiang, H.-H. Wang, Y. (Michael) Yang, Y. Liu, J. You, Y. Yang, Perovskite solar cells: film formation and properties, J. Mater. Chem. A. 3 (2015) 9032–9050. https://doi.org/10.1039/C4TA05246C.

[182] J. Burschka, N. Pellet, S.-J. Moon, R. Humphry-Baker, P. Gao, M.K. Nazeeruddin, M. Grätzel, Sequential deposition as a route to high-performance perovskite-sensitized solar cells., Nature. 499 (2013) 316–319. https://doi.org/10.1038/nature12340.

[183] S. Pang, H. Hu, J. Zhang, S. Lv, Y. Yu, F. Wei, T. Qin, H. Xu, Z. Liu, G. Cui, NH2CH=NH2PbI3: An alternative organolead iodide perovskite sensitizer for mesoscopic solar cells, Chem. Mater. 26 (2014) 1485–1491. https://doi.org/10.1021/cm404006p.

[184] Z. Xiao, C. Bi, Y. Shao, Q. Dong, Q. Wang, Y. Yuan, C. Wang, Y. Gao, J. Huang, Efficient, high yield perovskite photovoltaic devices grown by interdiffusion of solution-processed precursor stacking layers, Energy Environ. Sci. 7 (2014) 2619–2623. https://doi.org/10.1039/C4EE01138D.

[185] J.H. Im, H.S. Kim, N.G. Park, Morphology-photovoltaic property correlation in perovskite solar cells: One-step versus two-step deposition of CH3NH3PbI 3, APL Mater. 2 (2014). https://doi.org/10.1063/1.4891275.

[186] M. Konstantakou, D. Perganti, P. Falaras, T. Stergiopoulos, Anti-solvent crystallization strategies for highly efficient perovskite solar cells, Crystals. 7 (2017) 1–21. https://doi.org/10.3390/cryst7100291.

[187] K. V. Kasiviswanathan, Hot Cells , Glove Boxes and Shield Facilities, Sci.

Technol. (2001) 3830–3834.

[188] F.E. Farina, W.S. Binti Azmi, K. Harafuji, Ultraviolet-ozone anode surface treatment and its effect on organic solar cells, Thin Solid Films. 623 (2017) 72–83. https://doi.org/10.1016/j.tsf.2016.12.031.

[189] H. Hocheng, H.Y. Tsai, U.U. Jadhav, K.Y. Wang, T.C. Lin, Laser Surface Patterning, Elsevier, 2014. https://doi.org/10.1016/B978-0-08-096532-1.00917-1.

[190] N.K. Noel, S.N. Habisreutinger, B. Wenger, M.T. Klug, M.T. Hörantner, M.B. Johnston, R.J. Nicholas, D.T. Moore, H.J. Snaith, A low viscosity, low boiling point, clean solvent system for the rapid crystallisation of highly specular perovskite films, Energy Environ. Sci. 10 (2017) 145–152. https://doi.org/10.1039/C6EE02373H.

[191] A. Santos, T. Kumeria, Nanoporous Anodic Alumina for Optical Biosensing, in: D. Losic, A. Santos (Eds.), Nanoporous Alumina Fabr. Struct. Prop. Appl., Springer Series in Materials Science, 2015: pp. 219–247. https://doi.org/10.1007/978-3-319-20334-8.

[192] T. Aerts, I. De Graeve, H. Terryn, Study of initiation and development of local burning phenomena during anodizing of aluminium under controlled convection, Electrochim. Acta. 54 (2008) 270–279. https://doi.org/10.1016/j.electacta.2008.08.004.

[193] Y. Li, M. Zheng, L. Ma, W. Shen, Fabrication of highly ordered nanoporous alumina films by stable high-field anodization, Nanotechnology. 17 (2006) 5101–5105. https://doi.org/10.1088/0957-4484/17/20/010.

[194] W. Guo, D.T. Johnson, Pattern selection with anisotropy during aluminum electropolishing, J. Cryst. Growth. 268 (2004) 258–271. https://doi.org/10.1016/j.jcrysgro.2004.04.039.

[195] V. V. Yuzhakov, P. V. Takhistov, A.E. Miller, H.C. Chang, Pattern selection during electropolishing due to double-layer effects, Chaos. 9 (1999) 62–77.

https://doi.org/10.1063/1.166380.

[196] D. Ma, S. Li, C. Liang, Electropolishing of high-purity aluminium in perchloric acid and ethanol solutions, Corros. Sci. 51 (2009) 713–718. https://doi.org/10.1016/j.corsci.2009.01.030.

[197] L. Zaraska, M. Jaskuła, G.D. Sulka, Porous anodic alumina layers with modulated pore diameters formed by sequential anodizing in different electrolytes, Mater. Lett. 171 (2016) 315–318. https://doi.org/10.1016/j.matlet.2016.02.113.

[198] S.S. Mali, C.K. Hong, P-i-n/n-i-p type planar hybrid structure of highly efficient perovskite solar cells towards improved air stability: Synthetic strategies and the role of p-type hole transport layer (HTL) and n-type electron transport layer (ETL) metal oxides, Nanoscale. 8 (2016) 10528–10540. https://doi.org/10.1039/c6nr02276f.

[199] P. Roy, N. Kumar Sinha, S. Tiwari, A. Khare, A review on perovskite solar cells: Evolution of architecture, fabrication techniques, commercialization issues and status, Sol. Energy. 198 (2020) 665–688. https://doi.org/10.1016/j.solener.2020.01.080.

[200] J. Bai, B. Zhou, Titanium dioxide nanomaterials for sensor applications, Chem. Rev. 114 (2014) 10131–10176. https://doi.org/10.1021/cr400625j.

[201] P. Tonui, S.O. Oseni, G. Sharma, Q. Yan, G. Tessema Mola, Perovskites photovoltaic solar cells: An overview of current status, Renew. Sustain. Energy Rev. 91 (2018) 1025–1044. https://doi.org/10.1016/j.rser.2018.04.069.

[202] H. Liu, Z. Huang, S. Wei, L. Zheng, L. Xiao, Q. Gong, Nano-structured electron transporting materials for perovskite solar cells, Nanoscale. 8 (2016) 6209–6221. https://doi.org/10.1039/c5nr05207f.

[203] D.A.H. Hanaor, C.C. Sorrell, Review of the anatase to rutile phase transformation, J. Mater. Sci. 46 (2011) 855–874.

https://doi.org/10.1007/s10853-010-5113-0.

[204] L. Xiong, Y. Guo, J. Wen, H. Liu, G. Yang, P. Qin, G. Fang, Review on the Application of SnO2 in Perovskite Solar Cells, Adv. Funct. Mater. 28 (2018) 1–18. https://doi.org/10.1002/adfm.201802757.

[205] Y. Chen, Q. Meng, L. Zhang, C. Han, H. Gao, Y. Zhang, H. Yan, SnO2-based electron transporting layer materials for perovskite solar cells: A review of recent progress, J. Energy Chem. 35 (2019) 144–167. https://doi.org/10.1016/j.jechem.2018.11.011.

[206] R. Sethi, S. Ahmad, A. Aziz, A.M. Siddiqui, Structural, optical and electrical properties of tin oxide thin films for application as a wide band gap semiconductor, AIP Conf. Proc. 1675 (2015). https://doi.org/10.1063/1.4929255.

[207] J.W. Lee, L. Meng, Y. Yang, Semiconducting Metal Oxides for High Performance Perovskite Solar Cells, Elsevier Inc., 2018. https://doi.org/10.1016/B978-0-12-811165-9.00007-7.

[208] U. Khan, Y. Zhinong, A.A. Khan, A. Zulfiqar, Q.U. khan, Organic–inorganic hybrid perovskites based on methylamine lead halide solar cell, Sol. Energy. 189 (2019) 421–425. https://doi.org/10.1016/j.solener.2019.06.061.

[209] C. Dong, Z.K. Wang, L.S. Liao, Progress of Triple Cation Organometal Halide Perovskite Solar Cells, Energy Technol. 8 (2020) 1–14. https://doi.org/10.1002/ente.201900804.

[210] X. Wu, Y. Jiang, C. Chen, J. Guo, X. Kong, Y. Feng, S. Wu, X. Gao, X. Lu, Q. Wang, G. Zhou, Y. Chen, J.M. Liu, K. Kempa, J. Gao, Stable Triple Cation Perovskite Precursor for Highly Efficient Perovskite Solar Cells Enabled by Interaction with 18C6 Stabilizer, Adv. Funct. Mater. 30 (2020) 1–8. https://doi.org/10.1002/adfm.201908613.

[211] P. Ganesan, K. Fu, P. Gao, I. Raabe, K. Schenk, R. Scopelliti, J. Luo, L.H. Wong, M. Grätzel, M.K. Nazeeruddin, A simple spiro-type hole transporting material

for efficient perovskite solar cells, Energy Environ. Sci. 8 (2015) 1986–1991. https://doi.org/10.1039/c4ee03773a.

[212] J.H. Noh, N.J. Jeon, Y.C. Choi, M.K. Nazeeruddin, M. Grätzel, S. Il Seok, Nanostructured TiO2/CH3NH3PbI3 heterojunction solar cells employing spiro-OMeTAD/Co-complex as hole-transporting material, J. Mater. Chem. A. 1 (2013) 11842–11847. https://doi.org/10.1039/c3ta12681a.

[213] H. Zhang, Y. Shi, F. Yan, L. Wang, K. Wang, Y. Xing, Q. Dong, T. Ma, A dual functional additive for the HTM layer in perovskite solar cells, Chem. Commun. 50 (2014) 5020–5022. https://doi.org/10.1039/c3cc49458f.

[214] W.H. Nguyen, C.D. Bailie, E.L. Unger, M.D. McGehee, Enhancing the hole-conductivity of spiro-OMeTAD without oxygen or lithium salts by using spiro(TFSI)2 in perovskite and dye-sensitized solar cells, J. Am. Chem. Soc. 136 (2014) 10996–11001. https://doi.org/10.1021/ja504539w.

[215] J.G. Sánchez, V.S. Balderrama, M. Estrada, E. Osorio, J. Ferré-Borrull, L.F. Marsal, J. Pallarès, Stability study of high efficiency polymer solar cells using TiOx as electron transport layer, Sol. Energy. 150 (2017) 147–155. https://doi.org/10.1016/j.solener.2017.04.013.

[216] Z. Shariatinia, Recent progress in development of diverse kinds of hole transport materials for the perovskite solar cells: A review, Renew. Sustain. Energy Rev. 119 (2020) 109608. https://doi.org/10.1016/j.rser.2019.109608.

[217] T.T. Ava, A. Al Mamun, S. Marsillac, G. Namkoong, A review: Thermal stability of methylammonium lead halide based perovskite solar cells, Appl. Sci. 9 (2019). https://doi.org/10.3390/app9010188.

[218] P. Zhang, J. Wu, T. Zhang, Y. Wang, D. Liu, H. Chen, L. Ji, C. Liu, W. Ahmad, Z.D. Chen, S. Li, Perovskite Solar Cells with ZnO Electron-Transporting Materials, Adv. Mater. 30 (2018) 1–20. https://doi.org/10.1002/adma.201703737.

[219] K. Hong, K. Kim, S. Kim, I. Lee, H. Cho, S. Yoo, H.W. Choi, N.Y. Lee, Y.H. Tak,

J.L. Lee, Optical properties of WO3/Ag/WO3 multilayer as transparent cathode in top-emitting organic light emitting diodes, J. Phys. Chem. C. 115 (2011) 3453–3459. https://doi.org/10.1021/jp109943b.

[220] J. Tirado, C. Roldán-Carmona, F.A. Muñoz-Guerrero, G. Bonilla-Arboleda, M. Ralaiarisoa, G. Grancini, V.I.E. Queloz, N. Koch, M.K. Nazeeruddin, F. Jaramillo, Copper sulfide nanoparticles as hole-transporting-material in a fully-inorganic blocking layers n-i-p perovskite solar cells: Application and working insights, Appl. Surf. Sci. 478 (2019) 607–614. https://doi.org/10.1016/j.apsusc.2019.01.289.

[221] B.C. O'Regan, P.R.F. Barnes, X. Li, C. Law, E. Palomares, J.M. Marin-Beloqui, Optoelectronic studies of methylammonium lead iodide perovskite solar cells with mesoporous TiO2: Separation of electronic and chemical charge storage, understanding two recombination lifetimes, and the evolution of band offsets during J - V hysteresis, J. Am. Chem. Soc. 137 (2015) 5087–5099. https://doi.org/10.1021/jacs.5b00761.

[222] N.F. Montcada, J.M. Marín-Beloqui, W. Cambarau, J. Jiménez-López, L. Cabau, K.T. Cho, M.K. Nazeeruddin, E. Palomares, Analysis of Photoinduced Carrier Recombination Kinetics in Flat and Mesoporous Lead Perovskite Solar Cells, ACS Energy Lett. 2 (2017) 182–187. https://doi.org/10.1021/acsenergylett.6b00600.

[223] X.P. Cui, K.J. Jiang, J.H. Huang, X.Q. Zhou, M.J. Su, S.G. Li, Q.Q. Zhang, L.M. Yang, Y.L. Song, Electrodeposition of PbO and its in situ conversion to CH3NH3PbI3 for mesoscopic perovskite solar cells, Chem. Commun. 51 (2015) 1457–1460. https://doi.org/10.1039/c4cc08269a.

[224] M. Jung, S.G. Ji, G. Kim, S. Il Seok, Perovskite precursor solution chemistry: From fundamentals to photovoltaic applications, Chem. Soc. Rev. 48 (2019) 2011–2038. https://doi.org/10.1039/c8cs00656c.

[225] E. Aktas, J. Jiménez-López, C. Rodríguez-Seco, R. Pudi, M.A. Ortuño, N. López,

E. Palomares, Supramolecular Coordination of Pb2+ Defects in Hybrid Lead Halide Perovskite Films Using Truxene Derivatives as Lewis Base Interlayers, ChemPhysChem. 20 (2019) 2702–2711. https://doi.org/10.1002/cphc.201900068.

[226] S. Wang, A. Cabreros, Y. Yang, A.S. Hall, S. Valenzuela, Y. Luo, J.-P. Correa-Baena, M. Kim, Ø. Fjeldberg, D.P. Fenning, Y.S. Meng, Impacts of the Hole Transport Layer Deposition Process on Buried Interfaces in Perovskite Solar Cells, Cell Reports Phys. Sci. 1 (2020) 100103. https://doi.org/10.1016/j.xcrp.2020.100103.

[227] T.H. Schloemer, J.A. Christians, J.M. Luther, A. Sellinger, Doping strategies for small molecule organic hole-transport materials: impacts on perovskite solar cell performance and stability, Chem. Sci. 10 (2019) 1904–1935. https://doi.org/10.1039/C8SC05284K.

[228] Q. Jiang, L. Zhang, H. Wang, X. Yang, J. Meng, H. Liu, Z. Yin, J. Wu, X. Zhang, J. You, Enhanced electron extraction using SnO2 for high-efficiency planar-structure HC(NH2)2 PbI3-based perovskite solar cells, Nat. Energy. 2 (2017). https://doi.org/10.1038/nenergy.2016.177.

[229] J. Tirado, M. Vásquez-Montoya, C. Roldán-Carmona, M. Ralaiarisoa, N. Koch, M.K. Nazeeruddin, F. Jaramillo, Air-Stable n-i-p Planar Perovskite Solar Cells Using Nickel Oxide Nanocrystals as Sole Hole-Transporting Material, ACS Appl. Energy Mater. 2 (2019) 4890–4899. https://doi.org/10.1021/acsaem.9b00603.

[230] E.H. Anaraki, A. Kermanpur, L. Steier, K. Domanski, T. Matsui, W. Tress, M. Saliba, A. Abate, M. Grätzel, A. Hagfeldt, J.P. Correa-Baena, Highly efficient and stable planar perovskite solar cells by solution-processed tin oxide, Energy Environ. Sci. 9 (2016) 3128–3134. https://doi.org/10.1039/c6ee02390h.

[231] B. Chen, M. Yang, S. Priya, K. Zhu, Origin of J–V Hysteresis in Perovskite Solar

Cells, J. Phys. Chem. Lett. 7 (2016) 905–917. https://doi.org/10.1021/acs.jpclett.6b00215.

[232] S.A.L. Weber, I.M. Hermes, S.-H. Turren-Cruz, C. Gort, V.W. Bergmann, L. Gilson, A. Hagfeldt, M. Graetzel, W. Tress, R. Berger, How the formation of interfacial charge causes hysteresis in perovskite solar cells, Energy Environ. Sci. 11 (2018) 2404–2413. https://doi.org/10.1039/C8EE01447G.

[233] R. Gottesman, E. Haltzi, L. Gouda, S. Tirosh, Y. Bouhadana, A. Zaban, E. Mosconi, F. De Angelis, Extremely Slow Photoconductivity Response of CH3NH3PbI3 Perovskites Suggesting Structural Changes under Working Conditions, J. Phys. Chem. Lett. 5 (2014) 2662–2669. https://doi.org/10.1021/jz501373f.

[234] A. Pockett, G.E. Eperon, T. Peltola, H.J. Snaith, A. Walker, L.M. Peter, P.J. Cameron, Characterization of Planar Lead Halide Perovskite Solar Cells by Impedance Spectroscopy, Open-Circuit Photovoltage Decay, and Intensity-Modulated Photovoltage/Photocurrent Spectroscopy, J. Phys. Chem. C. 119 (2015) 3456–3465. https://doi.org/10.1021/jp510837q.

[235] M. Saliba, J.P. Correa-Baena, C.M. Wolff, M. Stolterfoht, N. Phung, S. Albrecht, D. Neher, A. Abate, How to Make over 20% Efficient Perovskite Solar Cells in Regular (n-i-p) and Inverted (p-i-n) Architectures, Chem. Mater. 30 (2018) 4193–4201. https://doi.org/10.1021/acs.chemmater.8b00136.

[236] F. Diao, X. Xiao, B. Luo, H. Sun, F. Ding, L. Ci, P. Si, Two-step fabrication of nanoporous copper films with tunable morphology for SERS application, Appl. Surf. Sci. 427 (2018) 1271–1279. https://doi.org/10.1016/j.apsusc.2017.08.117.

[237] G.E. Thompson, Porous anodic alumina: Fabrication, characterization and applications, Thin Solid Films. 297 (1997) 192–201. https://doi.org/10.1016/S0040-6090(96)09440-0.

[238] Y. Piao, H. Lim, J.Y. Chang, W.-Y. Lee, H. Kim, Nanostructured materials

prepared by use of ordered porous alumina membranes, Electrochim. Acta. 50 (2005) 2997–3013. https://doi.org/10.1016/j.electacta.2004.12.043.

[239] K. Liu, S. Fournier-Bidoz, G.A. Ozin, I. Manners, Highly Ordered Magnetic Ceramic Nanorod Arrays from a Polyferrocenylsilane by Nanoimprint Lithography with Anodic Aluminum Oxide Templates, Chem. Mater. 21 (2009) 1781–1783. https://doi.org/10.1021/cm900164b.

[240] Fabrication and Magnetic Properties of Co Nanostructures in AAO Membranes, Bull. Korean Chem. Soc. 29 (2008) 758–760. https://doi.org/10.5012/bkcs.2008.29.4.758.

[241] M. Vázquez, K.R. Pirota, D. Navas, A. Asenjo, M. Hernández-Vélez, P. Prieto, J.M. Sanz, Ordered magnetic nanohole and antidot arrays prepared through replication from anodic alumina templates, J. Magn. Magn. Mater. 320 (2008) 1978–1983. https://doi.org/10.1016/j.jmmm.2008.02.053.

[242] T. Yanagishita, K. Nishio, H. Masuda, Fabrication of Metal Nanohole Arrays with High Aspect Ratios Using Two-Step Replication of Anodic Porous Alumina, Adv. Mater. 17 (2005) 2241–2243. https://doi.org/10.1002/adma.200500249.

[243] Z. Fan, H. Razavi, J. Do, A. Moriwaki, O. Ergen, Y.-L. Chueh, P.W. Leu, J.C. Ho, T. Takahashi, L.A. Reichertz, S. Neale, K. Yu, M. Wu, J.W. Ager, A. Javey, Three-dimensional nanopillar-array photovoltaics on low-cost and flexible substrates, Nat. Mater. 8 (2009) 648–653. https://doi.org/10.1038/nmat2493.

[244] C.F. Huang, Y. Lin, Y.K. Shen, Y.M. Fan, Optimal processing for hydrophobic nanopillar polymer surfaces using nanoporous alumina template, Appl. Surf. Sci. 305 (2014) 419–426. https://doi.org/10.1016/j.apsusc.2014.03.105.

[245] P. Chowdhury, S.B. Sellarajan, M. Krishnan, K. Raghuvaran, H.C. Barshilia, K.S. Rajam, *In Situ* Electrochemical Thinning of Barrier Oxide Layer of Porous Anodic Alumina Template, Adv. Sci. Lett. 5 (2012) 253–257.

https://doi.org/10.1166/asl.2012.2018.

[246] A. Santos, L. Vojkuvka, J. Pallarés, J. Ferré-Borrull, L.F. Marsal, In situ electrochemical dissolution of the oxide barrier layer of porous anodic alumina fabricated by hard anodization, J. Electroanal. Chem. 632 (2009) 139–142. https://doi.org/10.1016/j.jelechem.2009.04.008.

[247] K. Nielsch, F. Müller, A.-P. Li, U. Gösele, Uniform Nickel Deposition into Ordered Alumina Pores by Pulsed Electrodeposition, Adv. Mater. 12 (2000) 582–586. https://doi.org/10.1002/(SICI)1521-4095(200004)12:8<582::AID-ADMA582>3.0.CO;2-3.

[248] N.A.N. Ouedraogo, Y. Chen, Y.Y. Xiao, Q. Meng, C.B. Han, H. Yan, Y. Zhang, Stability of all-inorganic perovskite solar cells, Nano Energy. 67 (2020) 104249. https://doi.org/10.1016/j.nanoen.2019.104249.

[249] M.P. Montero-Rama, A. Viterisi, C. Eckstein, J. Ferré-Borrull, L.F. Marsal, In-situ removal of thick barrier layer in nanoporous anodic alumina by constant current Re-anodization, Surf. Coatings Technol. 380 (2019) 125039. https://doi.org/10.1016/j.surfcoat.2019.125039.

[250] J.Y. Kim, S.H. Kim, H.H. Lee, K. Lee, W. Ma, X. Gong, A.J. Heeger, New architecture for high-efficiency polymer photovoltaic cells using solution-based titanium oxide as an optical spacer, Adv. Mater. 18 (2006) 572–576. https://doi.org/10.1002/adma.200501825.

[251] S. Lilliu, T.G. Dane, M. Alsari, J. Griffin, A.T. Barrows, M.S. Dahlem, R.H. Friend, D.G. Lidzey, J.E. Macdonald, Mapping Morphological and Structural Properties of Lead Halide Perovskites by Scanning Nanofocus XRD, Adv. Funct. Mater. 26 (2016) 8221–8230. https://doi.org/10.1002/adfm.201603446.

[252] M.Z. Rahman, T. Edvinsson, X-ray diffraction and Raman spectroscopy for lead halide perovskites, Elsevier Inc., 2020. https://doi.org/10.1016/b978-0-12-814727-6.00002-5.

[253] T. Baikie, Y. Fang, J.M. Kadro, M. Schreyer, F. Wei, S.G. Mhaisalkar, M. Graetzel, T.J. White, Synthesis and crystal chemistry of the hybrid perovskite (CH 3NH3)PbI3 for solid-state sensitised solar cell applications, J. Mater. Chem. A. 1 (2013) 5628–5641. https://doi.org/10.1039/c3ta10518k.

[254] K. Jeon, H. Youn, S. Kim, S. Shin, M. Yang, Fabrication and characterization of WO3/Ag/WO3 multilayer transparent anode with solution-processed WO3 for polymer light-emitting diodes, Nanoscale Res. Lett. 7 (2012) 1–7. https://doi.org/10.1186/1556-276X-7-253.

[255] S.B. Sepulveda-Mora, S.G. Cloutier, Figures of merit for high-performance transparent electrodes using dip-coated silver nanowire networks, J. Nanomater. 2012 (2012). https://doi.org/10.1155/2012/286104.

[256] E.D. Palik, Handbook of optical constants of solids, Academic press, New York, 1998.

[257] R.S. Sennett, G.D. Scott, The structure of evaporated metal films and their optical properties, Josa. 40 (1950) 203–211. https://doi.org/10.1364/JOSA.40.000203.

[258] X. Yang, P. Gao, Z. Yang, J. Zhu, F. Huang, J. Ye, Optimizing ultrathin Ag films for high performance oxide-metal-oxide flexible transparent electrodes through surface energy modulation and template-stripping procedures, Sci. Rep. 7 (2017) 44576. https://doi.org/10.1038/srep44576.

[259] K.H. Cho, S. Il Ahn, S.M. Lee, C.S. Choi, K.C. Choi, Surface plasmonic controllable enhanced emission from the intrachain and interchain excitons of a conjugated polymer, Appl. Phys. Lett. 97 (2010) 241. https://doi.org/10.1063/1.3508949.

[260] Y.C. Han, M.S. Lim, J.H. Park, K.C. Choi, Optical effect of surface morphology of ag on multilayer electrode applications for OLEDs, IEEE Electron Device Lett. 35 (2014) 238–240. https://doi.org/10.1109/LED.2013.2293574.

[261] A. Indluru, T.L. Alford, Effect of Ag thickness on electrical transport and

optical properties of indium tin oxide-Ag-indium tin oxide multilayers, J. Appl. Phys. 105 (2009). https://doi.org/10.1063/1.3153977.

[262] S.-P. Cho, S. Na, S.-S. Kim, Efficient ITO-free semitransparent perovskite solar cells with metal transparent electrodes, Sol. Energy Mater. Sol. Cells. 196 (2019) 1–8. https://doi.org/10.1016/J.SOLMAT.2019.03.002.

[263] H.J. Bolink, E. Coronado, D. Repetto, M. Sessolo, E.M. Barea, J. Bisquert, G. Garcia-Belmonte, J. Prochazka, L. Kavan, Inverted solution processable OLEDs using a metal oxide as an electron injection contact, Adv. Funct. Mater. 18 (2008) 145–150. https://doi.org/10.1002/adfm.200700686.

[264] Z.L. Wang, J.L. Lee, Electron Microscopy Techniques for Imaging and Analysis of Nanoparticles, in: R. Kohli, K.L. Mittal (Eds.), Dev. Surf. Contam. Clean. Second Ed., 2nd ed., Elsevier Inc., 2008: pp. 395–443. https://doi.org/10.1016/B978-0-323-29960-2.00009-5.

[265] Y.Y. Zhu, G.Q. Ding, J.N. Ding, N.Y. Yuan, AFM, SEM and TEM studies on porous anodic alumina, Nanoscale Res. Lett. 5 (2010) 725–734. https://doi.org/10.1007/s11671-010-9538-9.

[266] R.K. Mishra, A.K. Zachariah, S. Thomas, Energy-Dispersive X-ray Spectroscopy Techniques for Nanomaterial, in: Microsc. Methods Nanomater. Charact., Elsevier Inc., 2017: pp. 383–405. https://doi.org/10.1016/b978-0-323-46141-2.00012-2.

[267] B. Voigtländer, Static Atomic Force Microscopy, in: At. Force Microsc., NanoScience and Technology Springer, Cham, 2019: pp. 69–86. https://doi.org/10.1007/978-3-030-13654-3_12.

[268] T.-M.L. iping Zhao, Gwo-Ching Wang, Real-Space Surface Profiling Techniques, Exp. Methods Phys. Sci. 37 (2001) 63–82. https://doi.org/10.1016/s1079-4042(13)70005-5.

[269] H. Chandra, S.W. Allen, S.W. Oberloier, N. Bihari, J. Gwamuri, J.M. Pearce, Open-source automated mapping four-point probe, Materials (Basel). 10

(2017) 1–17. https://doi.org/10.3390/ma10020110.

[270] B.P. Kafle, Theory and instrumentation of absorption spectroscopy, Chem. Anal. Mater. Charact. by Spectrophotometry. (2020) 17–38. https://doi.org/10.1016/b978-0-12-814866-2.00002-6.

[271] A.A. Bunaciu, E. gabriela Udriştioiu, H.Y. Aboul-Enein, X-Ray Diffraction: Instrumentation and Applications, Crit. Rev. Anal. Chem. 45 (2015) 289–299. https://doi.org/10.1080/10408347.2014.949616.

[272] J. Park, S. Lee, H.H. Lee, High-mobility polymer thin-film transistors fabricated by solvent-assisted drop-casting, Org. Electron. 7 (2006) 256–260. https://doi.org/10.1016/j.orgel.2006.03.008.

[273] R.G. Larson, T.J. Rehg, Spin Coating, in: S.F. Kistler, P.M. Schweizer (Eds.), Liq. Film Coat., Springer, Dordrecht, 1997: pp. 709–734. https://doi.org/10.1007/978-3-662-44324-8_1727.

[274] L.E. Scriven, Physics and Applications of DIP Coating and Spin Coating, MRS Proc. 121 (1988) 717–729. https://doi.org/10.1557/proc-121-717.

[275] N.-G. Park, Methodologies for high efficiency perovskite solar cells, Nano Converg. 3 (2016) 3–15. https://doi.org/10.1186/s40580-016-0074-x.

[276] S. Il Seok, M. Grätzel, N.G. Park, Methodologies toward Highly Efficient Perovskite Solar Cells, Small. 14 (2018) 1704177. https://doi.org/10.1002/smll.201704177.

[277] D.M. Mattox, Thermal Evaporation and Deposition in Vacuum, in: Found. Vac. Coat. Technol., 2018: pp. 151–184. https://doi.org/10.1016/b978-0-12-813084-1.00005-4.

Tarragona 2020